UNIVERSITÀ DEGLI STUDI DI BOLOGNA

FACOLTÀ DI SCIENZE MATEMATICHE FISICHE E NATURALI

Anno Accademico 2001/02

Dottorato di Ricerca in Fisica
XIV ciclo

Study of atmospheric neutrino oscillations by energy estimates of upgoing muons in MACRO

Tesi presentata da:
Dott. MIRIAM GIORGINI

Relatore:
Prof. GIORGIO GIACOMELLI

Coordinatore del dottorato:
Prof. GIOVANNI VENTURI

Correlatori:
Dr. EUGENIO SCAPPARONE
Dr. MAXIMILIANO SIOLI

Contents

Chapter 1

Introduction

In recent years, neutrino physics, and in particular neutrino oscillations, have become an important topic in the field of high energy physics. The existence of neutrino oscillations would require an extension of the subnuclear phenomena description beyond the Standard Model of the electroweak and strong interactions. Interest in this field has been revived by several experimental results, which strongly support the neutrino oscillation hypothesis (Chap. 2).

Many experiments studying solar neutrinos with different detection techniques measured solar electron neutrino fluxes significantly lower than the predictions. Moreover, results from the SuperKamiokande and SNO experiments gave a model independent strong indication of the presence of ν_μ and ν_τ in the flux of solar neutrinos on Earth.

Also several experiments studying atmospheric neutrinos, produced in the decay of secondary particles created in the interactions of primary cosmic rays with the nuclei of the Earth atmosphere, found strong indications for muon neutrino oscillations. Among these experiments, the MACRO underground detector (described in Chap. 4), located in the Gran Sasso Laboratory, found a global deficit and an anomalous zenith angle distribution of ν_μ-induced upthroughgoing muons. This result is supported by the lower energy data. The oscillation probability depends on the ratio L/E_ν, where L is the distance traveled by the neutrino between the production and the interaction points and E_ν is the neutrino energy. Since Monte Carlo simulations have shown a correlation between the neutrino energy and the muon energy at the detector level (Chap. 3), it is important to estimate the muon energy.

MACRO is not equipped with a magnet, so the only way to estimate the energy of muons is through their Multiple Coulomb Scattering (MCS) in the rock absorbers. The spatial resolution of the standard tracking system is ~ 1 cm. It allows muon energy estimates through MCS up to $E_\mu \sim 10$ GeV, which is not enough to fully exploit the informations from upthroughgoing muons. To improve the space resolution, the MACRO limited streamer tubes were used in drift mode, retrieving the time informations from the TDCs of the QTP electronics system designed for magnetic monopole searches.

The QTP electronics was not designed for drift time measurements; thus, to avoid systematic effects and to fully understand the capability of the QTP system in such context, the electronics was checked in two tests at the CERN PS/SPS beams. The tests confirmed the feasibility of a MCS analysis and indicated an improvement of the space resolution of a factor $\simeq 3.5$, from $\simeq 1$ cm to $\simeq 3$ mm. Then, we followed a Neural Network (NN) approach, which allowed to estimate the muon energy event by event up to $\simeq 40$ GeV (Chap. 5).

The same procedure was applied to the MACRO upthroughgoing muons. They were divided in four subsamples of different median energy; for each sample, the zenith angle distributions are in good agreement with the MC predictions for $\nu_\mu \longleftrightarrow \nu_\tau$ oscillations with the parameters obtained from the standard analysis of upthroughgoing muon data ($\Delta m^2 = 2.5 \cdot 10^{-3}$ eV^2 and maximal mixing). The NN output was calibrated in such a way to obtain, for each event, the L/E_ν value. The final L/E_ν distribution shows good agreement with the MC oscillation predictions (Chap. 6).

In this thesis, I shall first discuss the phenomenology of neutrino oscillations and the atmospheric neutrino flux calculations. I shall then describe the MACRO experiment and the MCS analysis; finally, I shall discuss the results.

Chapter 2

Neutrino oscillations

2.1 Introduction

In recent years, most of the research activity in neutrino physics focused on the phenomenon of neutrino oscillations, originally proposed by Bruno Pontecorvo [1]. The first idea of neutrino masses and mixing was based on an analogy with $K^0-\overline{K}^0$ mixing and on the absence of a general principle (like gauge invariance in the case of the photon) that obliges neutrinos to be massless particles. In the seventies, neutrino mixing was considered as a natural consequence of the analogy between quarks and leptons. After the appearance of GUT and other models beyond the Standard Model and after the hypothesis of the see-saw mechanism of neutrino mass generation, neutrino masses and mixing are considered as a signature of a new physics at an energy scale much larger than the electroweak scale.

Interest in this field has been revived by several experimental results, which in some cases strongly support the hypothesis of neutrino oscillations [2, 3]. In this section, after an introduction to the formalism of neutrino mixing and oscillations, the attention will be focused on the latest experimental results.

2.2 Neutrino mixing

Investigation of neutrino oscillations is based on two fundamental experimental facts: (*i*) the interaction of neutrinos with matter is described by the standard charged current (CC) and neutral current (NC) Lagrangians

$$\mathcal{L}_I^{\mathrm{CC}} = -\frac{g}{2\sqrt{2}}\, j_\alpha^{\mathrm{CC}}\, W^\alpha + \mathrm{h.c.} \quad ; \quad \mathcal{L}_I^{\mathrm{NC}} = -\frac{g}{2\cos\theta_W}\, j_\alpha^{\mathrm{NC}}\, Z^\alpha \tag{2.1}$$

where g is the electroweak interaction constant, θ_W is the Weinberg angle, W^α and Z^α are the fields of $W^\pm$ and Z^0 vector bosons and j_α^{CC} and j_α^{NC} are the leptonic charged and neutral currents.

The CC and NC interactions, Eq. (2.1), conserve flavour lepton numbers and determine *the notion* of flavour neutrinos and antineutrinos. For example, a neutrino produced in the decay $\pi^+ \to \mu^+ + \nu_\mu$ is a left-handed muon neutrino ν_μ, an antineutrino produced in the decay $n \to p + e^- + \overline{\nu}_e$ is a right-handed electron antineutrino $\overline{\nu}_e$.

(*ii*) Three flavour neutrinos exist in nature. The number of neutrino flavours was determined from measurements of the decay width of the Z^0 boson at LEP, obtaining (2.9841 ± 0.0083) [4].

According to the *neutrino mixing hypothesis* [1, 5] neutrino masses are different from zero and fields of massive neutrinos ν_i enter into the CC and the NC Lagrangians, Eq. (2.1), in the mixed form (L and R in the index mean left-handed and right-handed, respectively)

$$\nu_{lL} = \sum_i U_{li}\ \nu_{iL} \tag{2.2}$$

where ν_l is a flavour field, ν_i is the field of a neutrino with mass m_i and U is the unitary mixing matrix, also known as the Maki-Nakagawa-Sakata (MNS) matrix [5], the leptonic analogue of the CKM matrix [6] for the quark sector. Eq. (2.2) leads to a violation of flavour lepton numbers, but usually not of the total lepton number.

If neutrino masses are different from zero, there is a neutrino mass term in the total Lagrangian. The structure of the mass term depends on the mechanism of neutrino mass generation. Only left-handed neutrino fields ν_{lL} enter into the Lagrangian of the weak interaction, Eq. (2.1). In the case of massive neutrinos, both ν_{lL} and singlet ν_{lR} fields can enter in the neutrino mass term. If ν_{lL} and ν_{lR} enter in such a form that the total lepton number L is conserved, the fields of massive neutrinos are four-component Dirac fields and neutrino ν_i and antineutrino $\overline{\nu}_i$ have opposite lepton numbers. The corresponding mass term is called the Dirac mass term. The number of the massive neutrinos in the case of the standard Dirac mass term is equal to the number of flavour neutrinos. The Dirac mass term could be generated by the Standard Higgs mechanism with a Higgs doublet.

If the lepton number is not conserved, only left-handed components ν_{lL} can enter into the neutrino mass term. The corresponding mass term is called the Majorana mass term. It is a product of left-handed components ν_{lL} and right-handed components $(\nu_{lL})^c$, determined by the relation $(\nu_{lL})^c = C\overline{\nu}_{lL}^T$ where C is the matrix of the charge conjugation that satisfies the conditions

$$C\gamma_\alpha^T C^{-1} = -\gamma_\alpha \quad ; \quad C^T = -C \tag{2.3}$$

In the case of the Majorana mass term, the fields ν_i in Eq. (2.2) are two-component Majorana fields that satisfy the condition

$$\nu_i = \nu_i^c \tag{2.4}$$

The condition (2.4) means that neutrinos and antineutrinos, quanta of the Majorana field ν_i, are identical particles. The number of the massive neutrinos in the case of the Majorana mass term is equal to three. The Majorana mass term requires a mechanism beyond the Standard Model for neutrino mass generation with Higgs triplets.

In the most general case both ν_{lL} and ν_{lR} fields enter into the mass term and there are no conserved lepton numbers (the Dirac and Majorana mass term). As the lepton numbers are not conserved, there is no possibility to distinguish neutrinos and antineutrinos and fields of neutrinos with definite masses ν_i in the case of the Dirac and Majorana mass term are two-component Majorana fields. If three left-handed fields ν_{lL} and three right-handed fields ν_{lR} enter into the mass term, the number of massive Majorana neutrinos is equal to 6. For the mixing, we have

$$\nu_{lL} = \sum_{i=1}^{6} U_{li}\nu_{iL} \qquad (l = e, \mu, \tau) \tag{2.5}$$

and

$$(\nu_{lR})^c = \sum_{i=1}^{6} U_{\bar{l}i}\nu_{iL} \tag{2.6}$$

where U is the 6×6 unitary matrix and the fields ν_i satisfy the condition (2.4).

In the framework of the Dirac and Majorana mass terms, there is a mechanism of neutrino mass generation, the so called *see-saw mechanism* [7]. This mechanism is based on the assumption that the lepton number is violated by the right-handed Majorana mass term at the scale M ($\sim$ 300 GeV), which is much larger than the electroweak scale ($M_{EW} \simeq 80 \div 90$ GeV). In the see-saw case, in the mass spectrum of Majorana particles there are three light masses m_k (masses of neutrinos) and three heavy masses $M_k \simeq M$ $(k = 1, 2, 3)$. Neutrino masses are connected with the masses of the heavy Majorana particles by the see-saw relation

$$m_k \simeq \frac{(m_k^{\mathrm{f}})^2}{M_k} << m_k^{\mathrm{f}} \tag{2.7}$$

where m_k^{f} is the mass of lepton or quark in k-family. The see-saw mechanism connects the smallness of neutrino masses with respect to the masses of all other fundamental fermions with a new physics at a large energy scale.

The fields ν_{lR} do not enter into the Lagrangian of the standard electroweak interaction and are called sterile. The nature and the number of sterile fields depend on models. There could be singlet right-handed neutrino fields and also SUSY fields, and so on. Thus, in the most general case for the mixing we have

$$\nu_{lL} = \sum_{i=1}^{3+n_s} U_{li}\nu_{iL} \quad ; \quad \nu_{sL} = \sum_{i=1}^{3+n_s} U_{si}\nu_{iL} \tag{2.8}$$

where n_s is the number of sterile fields and U is a $(3+n_s) \times (3+n_s)$ unitary matrix.

2.3 Neutrino oscillations

Neutrino oscillations are the most important consequence of neutrino mixing. Neutrino oscillations were first considered by B. Pontecorvo [1], at the time when the two-component theory for *massless* neutrinos was proposed [8] and it was established that neutrinos are left-handed particles [9]. Only electron neutrino was known at that time. Pontecorvo considered the transition of a ν_e into a sterile left-handed state $\overline{\nu}_{eL}$.

If there is neutrino mixing and if neutrino mass-squared differences are much smaller than the square of the neutrino energy, the normalized state of a flavour neutrino with momentum $\vec{p}$ is given by

$$|\nu_\alpha\rangle = \sum_i U^*_{\alpha i} \; |\nu_i\rangle \tag{2.9}$$

where $|\nu_i\rangle$ is the mass state of a neutrino of mass m_i, momentum $\vec{p}$, energy (the light velocity in vacuum c is put equal to 1)

$$E_i = \sqrt{p^2 + m_i^2} \simeq p + \frac{m_i^2}{2p} \tag{2.10}$$

and negative helicity (up to the terms m_i^2/p^2)

Thus, if there is neutrino mixing, the neutrino flavour states are *superpositions* of states of neutrinos with definite masses. The phenomenon of neutrino oscillations is based on the relation (2.9). This relation is similar to the well known relations that connect the states of K^0 and $\overline{K}^0$ mesons with the states of K_S and K_L mesons, particles with definite masses and lifetimes.

2.3.1 Neutrino oscillations in vacuum

Let us consider now the evolution in vacuum of a mixed state given by Eq. (2.9). If at the initial time $t = 0$ the flavour neutrino state is $|\nu_\alpha\rangle$, at the time

t for the flavour neutrino state we have

$$|\nu_\alpha\rangle_t = \sum U_{\alpha i}^* \ e^{-iE_i t} \ |\nu_i\rangle = \sum_{\alpha'} A_{\nu_\alpha \to \nu_{\alpha'}}(t) \ |\nu_{\alpha'}\rangle \tag{2.11}$$

where

$$A_{\nu_\alpha \to \nu_{\alpha'}}(t) = \sum_i U_{\alpha' i} \ e^{-iE_i t} \ U_{\alpha i}^* \tag{2.12}$$

is the amplitude of the transition $\nu_\alpha \to \nu_{\alpha'}$ during the time t. In Eq. (2.12), the term $U_{\alpha i}^*$ is the amplitude of the transition from the state $|\alpha\rangle$ to the state $|i\rangle$; the term $e^{-iE_i t}$ describes the time evolution to the state with energy E_i; the term $U_{\alpha' i}$ is the amplitude of the transition from the state $|i\rangle$ to the state $|\alpha'\rangle$.

From Eq. (2.12), a transition between different neutrinos is an effect of neutrino mass differences and neutrino mixing. In fact, if all neutrino masses in Eq. (2.12) are the same and/or $U = 1$, $A_{\nu_\alpha \to \nu_{\alpha'}}(t) = e^{-iE_\nu t} \delta_{\alpha' \alpha}$ and there are no transitions between different types of neutrinos.

If we enumerate neutrino masses in such a way that $m_1 < m_2 < ...$, the probability of the transition $\nu_\alpha \to \nu_{\alpha'}$ in vacuum is given by

$$P(\nu_\alpha \to \nu_{\alpha'}) = \left| \sum_i U_{\alpha' i} \ U_{\alpha i}^* e^{-i \ \Delta m_{i1}^2 \frac{L}{2E_\nu}} \right|^2 \tag{2.13}$$

where $\Delta m_{i1}^2 = m_i^2 - m_1^2$, L is the distance between the neutrino source and the neutrino detector and E_ν is the neutrino energy.

The simplest case of neutrino oscillations is between two types of neutrinos. In this case the index i in Eq. (2.13) takes values 1 and 2. Taking into account the unitarity relation

$$U_{\alpha' 1} U_{\alpha 1}^* = \delta_{\alpha\alpha'} - U_{\alpha' 2} U_{\alpha 2}^* \tag{2.14}$$

for the transition probability we have

$$P(\nu_\alpha \to \nu_{\alpha'}) = |\delta_{\alpha' \alpha} + U_{\alpha'_2} U_{\alpha 2}^* \ (e^{-i\Delta m_{21}^2 \frac{L}{2E_\nu}} - 1)|^2 \tag{2.15}$$

where $\Delta m_{21}^2 \equiv \Delta m^2$. The neutrino mixing matrix for the 2×2 case has the following general form

$$\begin{pmatrix} \cos\theta & \sin\theta \\ -\sin\theta & \cos\theta \end{pmatrix} \tag{2.16}$$

where θ is the mixing angle. For $\alpha' \neq \alpha$, from Eq. (2.15) we have

$$P(\nu_\alpha \to \nu'_\alpha) = \frac{1}{2} A_{\alpha';\alpha} \left(1 - \cos \frac{\Delta m^2 \ L}{2E_\nu}\right) \tag{2.17}$$

where $A_{\alpha';\alpha} = 4|U_{\alpha'2}|^2 |U_{\alpha 2}|^2 = \sin^2 2\theta$. For the survival probability from Eq. (2.15) we have

$$P(\nu_\alpha \to \nu_\alpha) = 1 - P(\nu_\alpha \to \nu'_\alpha) = 1 - \frac{1}{2} B_{\alpha;\alpha} \left(1 - \cos \frac{\Delta m^2 L}{2E_\nu}\right) \tag{2.18}$$

where $B_{\alpha;\alpha} = 4|U_{\alpha 2}|^2 \ (1 - |U_{\alpha 2}|^2) = \sin^2 2\theta$.

Thus, in the case of transitions between two types of neutrinos all transition probabilities are characterized by the two oscillation parameters $\sin^2 2\theta$ and Δm^2. Notice that due to the unitarity of the mixing matrix in the two-neutrino case $A_{\alpha';\alpha} = B_{\alpha;\alpha}$. The oscillation probability, Eq. (2.17), can be approximated by the product of two factors:

$$P(\nu_\alpha \to \nu'_\alpha) \simeq \sin^2 2\theta \sin^2 \left(\frac{1.27 \ \Delta m^2 \ L}{E_\nu}\right) \tag{2.19}$$

The first one, $\sin^2 2\theta$, is an intrinsic parameter which describes the strength of the coupling between the two neutrino flavour and gives the maximum amplitude of the neutrino oscillations. The second factor is another oscillatory term, the period of which is determined by $\Delta m^2 \ L/E_\nu$. The values of the parameter L/E_ν depend on the experiment conditions.

Fig. 2.1 shows the survival and the $\nu_e \longleftrightarrow \nu_\mu$ oscillation probabilities for solar neutrinos in vacuum as a function of the neutrino energy.

From (2.17) and (2.18) it is obvious that neutrino oscillations can be observed if the condition

$$\frac{\Delta m^2 (\mathrm{eV})^2 \ L(\mathrm{m})}{E_\nu(\mathrm{MeV})} \gtrsim 1 \tag{2.20}$$

is satisfied. This can be achieved, for example, with low energy neutrino beams and large distances between the neutrino source and the detector. If the oscillation phase becomes too large, that is when E_ν/L is too small compared to

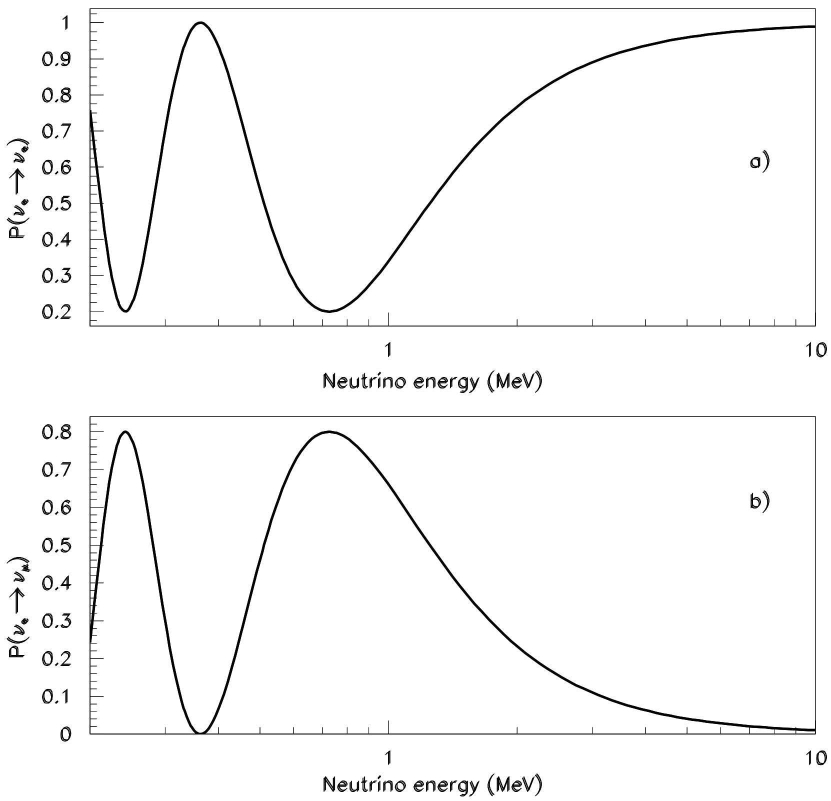

Figure 2.1: Survival (a) and $\nu_e \longleftrightarrow \nu_\mu$ oscillation (b) probabilities for solar ν_e in vacuum as a function of the neutrino energy.

Δm^2, the oscillations occur very rapidly and, due to the finite energy resolution of the experiments, the term $\sin^2(1.27\ \Delta m^2\ L/E_\nu)$ averages to 1/2.

The values of the parameter L/E_ν for experiments with accelerator neutrinos, reactor antineutrinos, atmospheric neutrinos and solar neutrinos are, respectively, in the ranges $10^{-1} \div 10^3$, $10^2 \div 10^3$, $10 \div 10^4$ and $10^{10} \div 10^{11}$. Thus, neutrino oscillation experiments are sensitive to the parameter Δm^2 in a wide range from $\Delta m^2 \simeq 10^{-11}$ eV^2 to $\Delta m^2 \simeq 10$ eV^2.

2.3.2 Neutrino oscillations in matter

Traveling through matter, neutrinos of all flavours can have neutral-current interactions with the protons, neutrons and electrons of the medium. However only electron neutrinos can interact with the electrons, through a coherent forward scattering via a W boson exchange. The consequence of this asymmetry between neutrino flavours is known as the *Mikheyev-Smirnov-Wolfenstein (MSW) effect* [10, 11].

At low neutrino energies, for electron, muon and tau neutrinos traversing an electrically neutral and unpolarized medium, the matter-induced potentials are given by:

$$\begin{aligned} V_e = &\quad \sqrt{2}G_F(N_e - N_n/2) \\ V_\mu = V_\tau = &\quad -\sqrt{2}G_F N_n/2 \end{aligned} \tag{2.21}$$

where G_F is the Fermi constant, N_e and N_n are the electron and the neutron densities in the medium, respectively. For antineutrinos the potentials have opposite signs. The weak potential in matter produces a phase shift that can modify the neutrino oscillation probability if the oscillating neutrinos have different interactions with matter. Therefore the matter effect could allow to discriminate between different oscillation channels.

According to Eq. (2.21), matter effects in the Earth could be important for $\nu_\mu \longleftrightarrow \nu_e$ and for $\nu_\mu \longleftrightarrow \nu_{sterile}$ oscillations, while for $\nu_\mu \longleftrightarrow \nu_\tau$ oscillations there is no matter effect.

In the simplest case of constant matter density and two-flavour oscillation, for example μ and e, the mass ($|\nu_1^M\rangle$ and $|\nu_2^M\rangle$) and flavour ($|\nu_e\rangle$ and $|\nu_\mu\rangle$) states are connected by a two-dimensional rotation. The relation between the two bases is given by:

$$\begin{aligned} |\nu_1^M\rangle = &\quad \cos\theta_M\ |\nu_e\rangle + \sin\theta_M\ |\nu_\mu\rangle \\ |\nu_2^M\rangle = &\quad -\sin\theta_M\ |\nu_e\rangle + \cos\theta_M\ |\nu_\mu\rangle \end{aligned} \tag{2.22}$$

where θ_M is the mixing angle in matter, given by [12]:

$$\sin^2 2\theta_M = \frac{\left(\frac{\Delta m^2}{2E}\right)^2\ \sin^2 2\theta}{\left(\frac{\Delta m^2}{2E}\cos 2\theta - \sqrt{2}G_F N_e\right)^2 + \left(\frac{\Delta m^2}{2E}\right)^2 \sin^2 2\theta} \tag{2.23}$$

The oscillation probability is of the same form as in Eq. (2.19), where the vacuum parameters are now replaced by those in matter. From Eq. (2.23) it follows that, regardless of the smallness of the mixing angle in vacuum, the mixing angle in matter can be large. In particular, maximal mixing can be achieved if the so-called *MSW resonance condition* is satisfied:

$$\sqrt{2}G_F N_e = \frac{\Delta m^2}{2E}\cos 2\theta \tag{2.24}$$

Since $N_e > 0$, Eq. (2.24) is fulfilled only if $\Delta m^2 \cos\theta > 0$. Once a convention on the phase has been chosen, Eq. (2.24) implies that resonant oscillation enhancement is possible only for one particular sign of Δm^2. This means that, for a given sign of Δm^2, matter effects cannot enhance neutrino and antineutrino oscillations at the same time: if neutrino oscillations are enhanced, antineutrino oscillations will be suppressed, and viceversa.

An interesting case to consider is the so-called *adiabatic approximation* for matter density monotonically decreasing along the neutrino path. Let us consider the case of two-flavour neutrino mixing (for example between ν_e and ν_μ), useful to describe neutrino oscillations in the Sun.

Electron neutrinos produced in the core of the Sun, where the density is above that corresponding to the MSW resonance, initially see a mixing angle $\theta_{core} \approx \pi/2$. From Eq. (2.22), at production point, a neutrino born as a ν_e would essentially coincide with one of the matter eigenstates ν_2^M. The adiabaticity condition, that requires a slowly changing matter distribution, guarantees that the neutrino system can gradually adjust to the changing density of the environment and that it doesn't make transitions to the other matter eigenstate. As ν_2^M propagates through the mantle, it encounters regions of smaller densities: the effective mixing angle decreases and the strength of the mixing increases, until the resonance condition is fulfilled and maximal mixing is reached. As the neutrino travels further, the mixing angle becomes smaller and smaller, approaching the value of the mixing angle in vacuum, θ. If θ is small, the ν_e component of ν_2^M is small at the final point and ν_2^M is mainly composed of ν_μ. The survival and the oscillation probabilities for electron neutrinos are given by:

$$P(\nu_e \longrightarrow \nu_e) = \sin^2\theta \quad ; \quad P(\nu_e \longrightarrow \nu_\mu) = \cos^2\theta \tag{2.25}$$

Thus, in the range of validity of the adiabatic approximation and for small values of the mixing angle in vacuum, if the depth of the traversed matter is large enough, the probability of finding the neutrino in the flavour state ν_e when it gets outside the Sun is tiny and a complete conversion of ν_e to ν_μ is possible.

2.4 The solar neutrino problem

The so-called Standard Solar Model (SSM) [13] is used to predict the solar neutrino flux under the assumption that no exotic phenomena, such as neutrino oscillations, can affect the nature of the produced neutrinos before they reach the Earth.

Source	Reaction	$\langle E_\nu \rangle$ (MeV)	E_ν^{max} (MeV)	Flux (10^{10} cm^{-2}s^{-1}) [13]
pp	$p+p \rightarrow d + e^+ + \nu_e$	0.2668	0.423	$5.95(1.00^{+0.01}_{-0.01})$
pep	$p+e^- + p \rightarrow d + \nu_e$	1.445	1.445	$1.40 \cdot 10^{-2}(1.00^{+0.015}_{-0.015})$
hep	$^3\mathrm{He} + p \rightarrow {}^4\mathrm{He} + e^+ + \nu_e$	9.628	18.778	$9.3 \cdot 10^{-7}$
^{7}Be	$e^- + {}^7\mathrm{Be} \rightarrow {}^7\mathrm{Li} + \nu_e$	0.3855	0.3855	$4.77 \cdot 10^{-1}(1.00^{+0.10}_{-0.10})$
		0.8631	0.8631	$4.77 \cdot 10^{-1}(1.00^{+0.10}_{-0.10})$
^{8}B	$^8\mathrm{B} \rightarrow {}^8\mathrm{Be}^* + e^+ + \nu_e$	6.735	~ 15	$5.05 \cdot 10^{-4}(1.00^{+0.20}_{-0.16})$
^{13}N	$^{13}\mathrm{N} \rightarrow {}^{13}\mathrm{C} + e^+ + \nu_e$	0.7063	1.1982	$5.48 \cdot 10^{-2}(1.00^{+0.21}_{-0.17})$
^{15}O	$^{15}\mathrm{O} \rightarrow {}^{15}\mathrm{N} + e^+ + \nu_e$	0.9964	1.7317	$4.80 \cdot 10^{-2}(1.00^{+0.25}_{-0.19})$
^{17}F	$^{17}\mathrm{F} \rightarrow {}^{17}\mathrm{O} + e^+ + \nu_e$	0.9977	1.7364	$5.63 \cdot 10^{-4}(1.00^{+0.25}_{-0.25})$

Table 2.1: Average and maximum neutrino energies and SSM flux predictions for the different reactions contributing to the solar neutrino flux [13, 14].

In this model, the sun belongs to the category of the main sequence stars, which produce energy in their interiors via thermonuclear reactions. The two reaction chains responsible for the energy production, known as the *pp*-cycle and the CNO-cycle, are illustrated in Fig. 2.2.

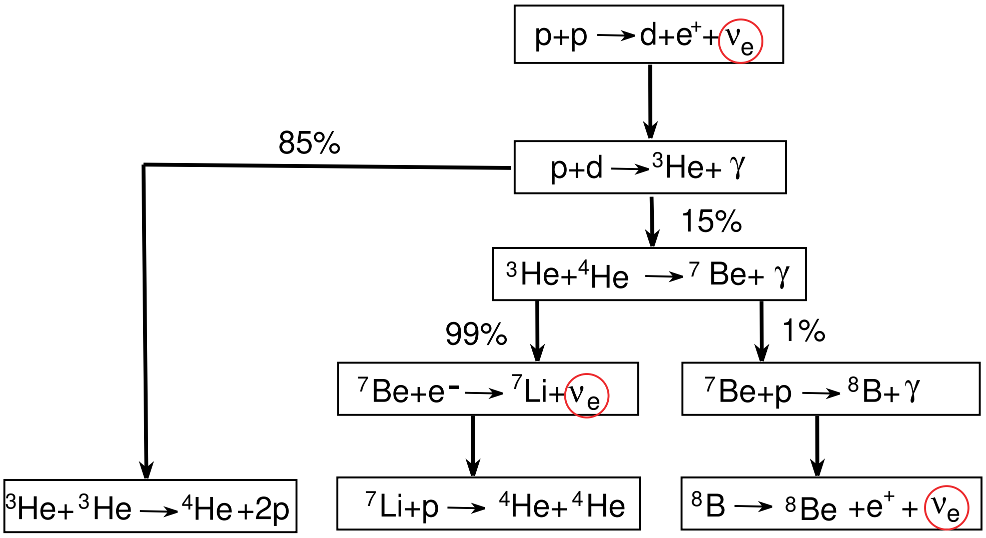

Figure 2.2: Reaction chains responsible of the production of solar ν_e.

For each reaction contributing to the solar neutrino flux, the average and maximum neutrino energies and the SSM flux prediction are listed in Table 2.1. For both cycles the overall result is the fusion of hydrogen nuclei into helium, with the emission of electron neutrinos:

$$4p + 2e^- \to^4 \text{He} + 2\nu_e + Q \tag{2.26}$$

where $Q = 4m_p + 2m_e - m_{^4He} \simeq 26.73$ MeV.

The SSM assumes that the Sun is in a stationary state and then infers a strong correlation between the solar neutrino flux and the solar luminosity ($L_\odot = 2.4{\cdot}10^{39}$ MeV s^{-1}, known with an accuracy of $\sim 0.4\%$). From Eq. (2.26), in the nuclear reactions occurring in the Sun, the production of two neutrinos is accompanied by an energy release of 26.73 MeV. Neglecting the amount of energy carried away by the neutrinos ($\sim 2\%$), the initial total electron neutrino flux can be connected with $L_\odot$ by the model independent relation [15]:

$$\int \frac{1}{2}(Q - 2E)\ \Phi_{\nu_e}^{tot}(E)dE = \frac{L_\odot}{4\pi R^2} \tag{2.27}$$

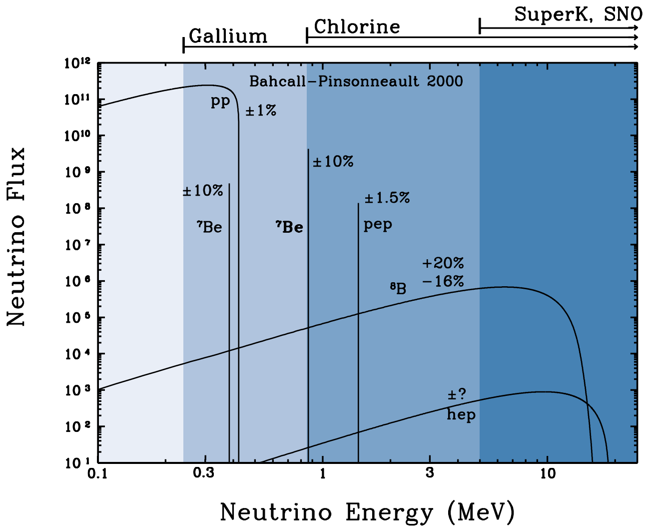

Figure 2.3: SSM predictions for the energy spectra of solar neutrinos produced in the *pp*-cycle reactions [13]. The continuum spectra are expressed in events $\mathrm{cm}^{-2}\mathrm{s}^{-1}\mathrm{MeV}^{-1}$ at one astronomical unit, while the monochromatic lines (*pep* and ^{7}Be) are given in events $\mathrm{cm}^{-2}\mathrm{s}^{-1}$. The energy thresholds of the different experiments are shown at the top of the plot.

where R is the distance between the sun and the earth and

$$\Phi_{\nu_e}^{tot}(E) = \sum_i \Phi_{\nu_e}^i(E) \tag{2.28}$$

with $\Phi_{\nu_e}^i$ is the flux of ν_e from the reaction i. The energy spectra of neutrinos from the *pp*-cycle are shown in Fig. 2.3 [13]. The uncertainties on the different flux components are also shown and the energy thresholds of the different experiments are indicated at the top of the plot.

2.4.1 Experimental results

The experiments which study solar neutrinos can be subdivided into two categories: radiochemical experiments (Homestake [16], SAGE [17], GALLEX [18] and GNO [19]) and water Cherenkov experiments (Kamiokande [20], SuperKamiokande [21] and SNO [22]). The main differences between these two categories are: (*i*) radiochemical experiments allow only an integrated measurement of the flux, water Cherenkov detectors perform real-time measurements and can study differential distributions (like the energy spectrum, the angular distribution, the correlation with the Sun position in the sky); (*ii*) the radiochemical experiments can measure the *pp* neutrinos whose flux is predicted with a precision of 1%, while water Cherenkov detectors, due to the higher detection threshold ($5 \div 7$ MeV), can see mainly neutrinos from the ^{8}B decay (see Fig. 2.3 and Table 2.2).

Radiochemical experiments

The Homestake [16] chlorine experiment, located in a gold mine in South Dakota (USA), uses a tank of $6 \cdot 10^5$ litre volume filled with tetrachlorethylene (C_2Cl_4). The detection principle is based on the reaction:

$$\nu_e +^{37} \mathrm{Cl} \to e^- +^{37} \mathrm{Ar} \tag{2.29}$$

which has a threshold of 814 keV, above the end-point of the *pp*-cycle energy spectrum. The measured rate, which mainly arises from of ^{8}B and ^{7}Be neutrinos, plus a small contribution from *pep* neutrinos, is (2.56 ± 0.23) SNU [16] (1 SNU$= 10^{-36}$ events atoms^{-1} s^{-1}), significantly below the predicted value of $7.6^{+1.3}_{-1.1}$ SNU [13].

The gallium experiments, SAGE [17], GALLEX [18] and GNO [19] detect neutrinos from the Sun by means of the process

$$\nu_e +^{71} \mathrm{Ga} \to e^- +^{71} \mathrm{Ge} \tag{2.30}$$

for which the energy threshold, 233.2 keV, is well below the maximum energy of the *pp* neutrinos. This means that gallium experiments can prove the thermonuclear nature of the energy production mechanism in the Sun by measuring low-energy solar neutrinos.

The GALLEX experiment was located at the Gran Sasso Underground Laboratory. It consisted of 30.3 tons of ^{71}Ga, in the form of a concentrated solution of gallium chloride ($GaCl_3$-HCl) in water. The ^{71}Ge atoms formed the volatile compound $GeCl_4$ which, at the end of each run ($3-4$ weeks) was swept out of the solution by means of a nitrogen stream. The $GeCl_4$ was absorbed in water in a gas scrubber, where the nitrogen was filtered out, and then converted to GeH_4. This compound was finally introduced, together with xenon, into a proportional counter where the number of ^{71}Ga atoms was determined by counting their radioactive decays. The final results from GALLEX gave a solar neutrino flux of $77.5^{+7.6}_{-7.8}$ SNU [18], again below the theoretical predictions of 128^{+9}_{-7} SNU [13].

The SAGE [17] experiment is located in the underground Baksan Neutrino Observatory (Russia). The detector uses gallium in its metallic form. The germanium produced in reaction (2.30) is removed from the metallic gallium by a liquid-liquid extraction into a HCl-H_2O_2 phase. After this initial step, the experimental technique is very similar to that followed by GALLEX. The results, based on a 10 years exposure time, yield a solar neutrino flux of $74^{+7.8}_{-7.4}$ SNU [17], in good agreement with the GALLEX results.

The GNO (Gallium Neutrino Observatory) experiment [19] is the successor project of the GALLEX experiment. The main aims of GNO are to provide a long time record of low-energy solar neutrinos, to determine the bulk production rate with an accuracy of 5 SNU and to monitor the time dependence of the *pp*-neutrino flux during a whole solar cycle with a precision of $\sim 15\%$. The measured solar neutrino flux, based on 19 months of observation, is $65.8^{+10.7}_{-10.2}$ SNU [19], which confirms the GALLEX result. A combined analysis of GNO and GALLEX gives $74.1^{+6.7}_{-6.8}$ SNU [19].

Water Cherenkov detectors

Both Kamiokande [20] and SuperKamiokande (SK) [21] are water Cherenkov detectors, located 1000 m underground in the Kamioka mine in Japan. Kamiokande was a cylindrical tank, of total volume 4.5 kton, filled with pure water. An inner volume of 2.14 kton was defined by 980 inward-looking photo-multiplier tubes (PMTs), used to detect the Cherenkov light produced by the relativistic particles traversing the water.

Kamiokande was stopped in summer 1997; its physics program has been continued by the successor experiment SuperKamiokande. It consists of a huge cylindrical tank (50 kton) filled with pure water. Also in this case an inner volume (32.5 kton) is defined by an inner surface equipped with about 11000 PMTs. The increased coverage of PMTs makes SuperKamiokande not only bigger than Kamiokande, but also better in terms of energy, position and angular resolution.

The energy threshold for Kamiokande and SuperKamiokande is determined by the threshold for detecting the recoil electron in the elastic scattering, which is about $5 \div 7.5$ MeV. Thus the solar neutrino flux measured in those experiments is essentially the ^{8}B flux (plus a small component from the *hep* reaction in SK) from the decay

$$^8\mathrm{B} \to ^8\mathrm{Be}^* + e^+ + \nu_e \tag{2.31}$$

In both experiments, the solar neutrinos are detected through the observation of the Cherenkov light rings produced by the electrons emitted in the elastic process:

$$\nu_x + e^- \to \nu_x + e^- \qquad\qquad (x = e, \mu, \tau) \tag{2.32}$$

All flavour neutrinos ν_e, ν_μ and ν_τ are detected in the SK experiment. However, the sensitivity to ν_μ and ν_τ is lower than the sensitivity to ν_e: the cross section of NC $\nu_\mu(\nu_\tau) + e$ scattering ($\simeq 0.157 \cdot 10^{-43} (E_\nu/10\mathrm{MeV})$ cm^2) is about six times smaller than the cross section of CC+NC $\nu_e + e$ scattering ($\simeq 0.92 \cdot 10^{-43} (E_\nu/10\mathrm{MeV})$ cm^2) [12, 23].

During 1258 days of running, 18464^{+677}_{-590} events with energy of the recoil electrons larger than 5 MeV were observed; for the neutrino flux, SK obtained [21]

$$(\Phi^{ES}_{\nu_x})_{SK} = (2.32 \pm 0.03 \pm 0.08) \cdot 10^6 \ \mathrm{cm}^{-2}\mathrm{s}^{-1} \tag{2.33}$$

The SK data alone do not allow to obtain an information separately on the fluxes of ν_e and $\nu_{\mu,\tau}$ on the earth. It became possible only after the data of the SNO (Sudbury Neutrino Observatory) experiment [22]. It is a water Cherenkov detector which uses 1000 tons of D_2O, allowing to measure simultaneously the ν_e flux from ^{8}B decay in the Sun and the flux of all active neutrino flavours through the following reactions:

$$\begin{array}{ll} \nu_e + d \longrightarrow p + p + e^- & \text{(CC)} \\ \nu_x + d \longrightarrow p + n + \nu_x & \text{(NC)} \\ \nu_x + e^- \longrightarrow \nu_x + e^- & \text{(ES)} \end{array} \tag{2.34}$$

The Feynman diagrams of the reactions above are illustrated in Fig. 2.4.

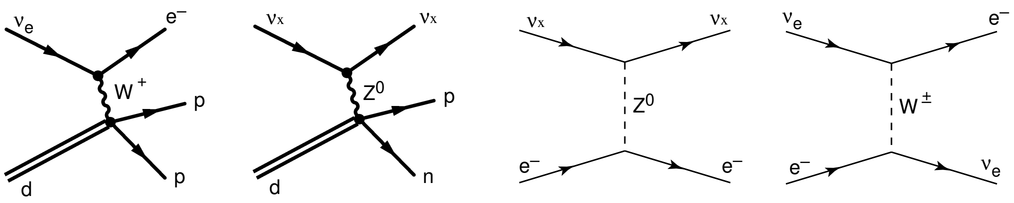

(a) (b) (c) (d)

Figure 2.4: Feynman diagrams of the reactions of Eq. (2.34): (a) refers to $\nu_e + d \longrightarrow p + p + e^-$, (b) refers to $\nu_x + d \longrightarrow p + n + \nu_x$, (c) and (d) refer to NC and CC $\nu_x + e^- \longrightarrow \nu_x + e^-$, respectively.

The charged-current (CC) reaction on the deuteron is sensitive exclusively to ν_e, while the neutral-current (NC) reaction has equal sensitivity to all active neutrino flavours (ν_x, $x = e, \mu, \tau$). Elastic scattering (ES) on electron is also sensitive to all active flavours, but with reduced sensitivity to ν_μ and ν_τ.

Comparison of the solar neutrino flux inferred from the reaction rates of these three reaction channels under the no-oscillation assumption can provide evidence for flavour-changing neutrino oscillations. If ν_e's from the Sun transform into another active flavour, then the solar neutrino flux deduced from the CC reaction rate ($\Phi^{CC}_{\nu_e}$) must be smaller than those deduced from the ES reaction rate or the NC reaction rate.

For the effective flux of ES events, SNO obtained the value

$$(\Phi_{\nu_x}^{ES})_{SNO} = (2.39 \pm 0.34 \pm 0.16) \cdot 10^6 \text{ cm}^{-2}\text{s}^{-1} \tag{2.35}$$

which is in agreement with the SK value (2.33) [21]. For the CC events, the SNO experiment found

$$\Phi_{\nu_e}^{CC} = (1.75 \pm 0.07 \pm 0.12 \pm 0.05) \cdot 10^6 \text{ cm}^{-2}\text{s}^{-1} \tag{2.36}$$

For the fluxes of ν_e on the earth we have

$$\Phi_{\nu_e}^{CC} = \langle P(\nu_e \to \nu_e) \rangle_{CC} \Phi_{\nu_e}^0 \quad ; \quad \Phi_{\nu_e}^{ES} = \langle P(\nu_e \to \nu_e) \rangle_{ES} \Phi_{\nu_e}^0 \tag{2.37}$$

where $\Phi_{\nu_e}^0$ is the total initial flux of the ^{8}B neutrinos. No indications of significant energy dependence of the ν_e survival probability in the SK and SNO energy ranges were obtained. Thus, we have $\Phi_{\nu_e}^{CC} \simeq \Phi_{\nu_e}^{ES}$. From Eq. (2.33) and Eq. (2.36), for the flux of ν_μ and ν_τ on the earth we obtain

$$\Phi_{\nu_{\mu,\tau}}^{ES} = (3.69 \pm 1.13) \cdot 10^6 \text{ cm}^{-2}\text{s}^{-1} \tag{2.38}$$

Thus, the results of the SNO and the SK experiments give the first model independent evidence (at $\simeq 3\sigma$ level) of the presence of ν_μ and ν_τ in the flux of solar neutrinos on earth. The flux of ν_μ and ν_τ is approximately two times larger than the ν_e flux.

From (2.36) and (2.38) for the total flux of all flavour neutrinos on the earth we have

$$\Phi_{\nu_{e,\mu,\tau}} = (5.44 \pm 0.99) \cdot 10^6 \text{ cm}^{-2}\text{s}^{-1} \tag{2.39}$$

This value is in a agreement with the total flux of ^{8}B neutrinos $\Phi_{\nu_e}^{SSM} = 5.05 \cdot 10^6 \text{ cm}^{-2}\text{s}^{-1}$ predicted by the SSM [13].

The recent values measured by the mentioned experiments are shown in Table 2.2. The data of all solar neutrino experiments can be described if we assume that two-neutrino oscillations, characterized by the two parameters Δm_{sol}^2 and $\tan^2\theta_{sol}$, take place. From the analysis of all existing data, made

Experiment	Measured Flux	SSM Flux [13]
Homestake	$2.56 \pm 0.16(\text{stat}) \pm 0.16(\text{sys})$	$7.6^{+1.3}_{-1.1}$
SAGE	$67.2^{+7.2}_{-7.0}(\text{stat})^{+3.5}_{-3.0}(\text{sys})$	128^{+9}_{-7}
Gallex	$77.5 \pm 6.2(\text{stat})^{+4.3}_{-4.7}(\text{sys})$	128^{+9}_{-7}
GNO	$65.8^{+10.2}_{-9.6}(\text{stat})^{+3.4}_{-3.6}(\text{sys})$	128^{+9}_{-7}
Kamiokande	$2.80 \pm 0.19(\text{stat}) \pm 0.33(\text{sys})$	$5 \cdot \left(1^{+0.20}_{-0.16}\right)$
SuperKamiokande	$2.32 \pm 0.03(\text{stat})^{+0.08}_{-0.07}(\text{sys})$	$5.05 \cdot \left(1^{+0.20}_{-0.16}\right)$

Table 2.2: Summary of solar electron neutrino observations at different solar neutrino detectors. The measured and predicted values are given in SNU for the radiochemical experiments and in 10^6 cm^{-2}s^{-1} for the water Cherenkov detectors.

under the assumption that the initial fluxes are given by the SSM, the several allowed regions (solutions) in the plane of these parameters were obtained. For oscillations in vacuum, the best values for the parameters are

$$\Delta m^2_{vac} \simeq 10^{-10} \text{ eV}^2 \quad ; \quad \sin^2 2\theta_{vac} \simeq 1 \tag{2.40}$$

After the new SK-SNO data, the preferable allowed regions became the large mixing angle MSW allowed regions (LMA, LOW) [24, 25]. For the best-fit values of the oscillation parameters in the LMA region [24] it was found

$$\Delta m^2_{MSW} = 4.5 \cdot 10^{-5} \text{ eV}^2 \quad ; \quad \tan^2 \theta_{MSW} = 4.1 \cdot 10^{-1} \tag{2.41}$$

2.5 The atmospheric neutrino anomaly

Atmospheric neutrinos are produced in the decay of secondary particles, mainly pions and kaons, created in the interactions of primary cosmic rays with the nuclei (N) of the Earth's atmosphere. If the energy of the secondary particles is sufficiently low ($\lesssim 2$ GeV) that all of them decay, we have:

$$\begin{aligned} p + N &\longrightarrow \pi^\pm + X \\ \pi^\pm &\longrightarrow \mu^\pm + \nu_\mu(\overline{\nu}_\mu) \\ \mu^\pm &\longrightarrow e^\pm + \nu_e(\overline{\nu}_e) + \overline{\nu}_\mu(\nu_\mu) \end{aligned} \tag{2.42}$$

Assuming that no effect can change the flavour composition of the shower before it is measured on Earth, Eq. (2.42) implies that:

$$R = \frac{N_{\nu_\mu} + N_{\overline{\nu}_\mu}}{N_{\nu_e} + N_{\overline{\nu}_e}} \simeq 2 \tag{2.43}$$

where N_{ν_μ} (N_{ν_e}) and $N_{\overline{\nu}_\mu}$ ($N_{\overline{\nu}_e}$) are the number of muon (electron) neutrinos and antineutrinos, respectively. The exact value of R can be affected by several effects, such as the primary energy spectrum and composition, the geomagnetic cut-off, the solar activity and the details of the model for the development of the hadronic shower. However, although the absolute neutrino fluxes are rather badly known (predictions from different calculations disagree by $\sim 20\%$), the ratio (2.43) is known at $\sim 5\%$. Neutrino oscillations could manifest as a discrepancy between the measured and the expected value of the ratio R.

For the experiments which can measure ν_μ and ν_e, the result is generally presented in terms of the double ratio:

$$R' = \frac{R_{DATA}}{R_{MC}} = \frac{[(N_{\nu_\mu} + N_{\overline{\nu}_\mu})/(N_{\nu_e} + N_{\overline{\nu}_e})]_{DATA}}{[(N_{\nu_\mu} + N_{\overline{\nu}_\mu})/(N_{\nu_e} + N_{\overline{\nu}_e})]_{MC}} \tag{2.44}$$

which is independent from the experimental parameters, such as energy thresholds and detector acceptances for signals and background. In Eq. (2.44), R_{DATA} is the measured ratio of muon-like over electron-like events and R_{MC} is the same ratio obtained from a Monte Carlo simulation. $R' < 1$ is interpreted as a deficit of measured muon-like events.

Another sensitive way to detect neutrino oscillations is the study of the zenith angle distribution of the incoming atmospheric neutrino. Downward-going neutrinos, produced in the atmosphere above the detector, will travel a path of the order of $10 \div 20$ km, while upward-going neutrinos, produced at the opposite side of the globe, will travel up to ~ 13000 km before detection. By studying the neutrino flux as a function of the zenith angle, one has baselines spanning three orders of magnitude and could observe the modulation induced on the flux by neutrino oscillations.

Assuming that no oscillation occurs between the production point and the detector and that no other effects alter the cosmic ray angular distribution, the

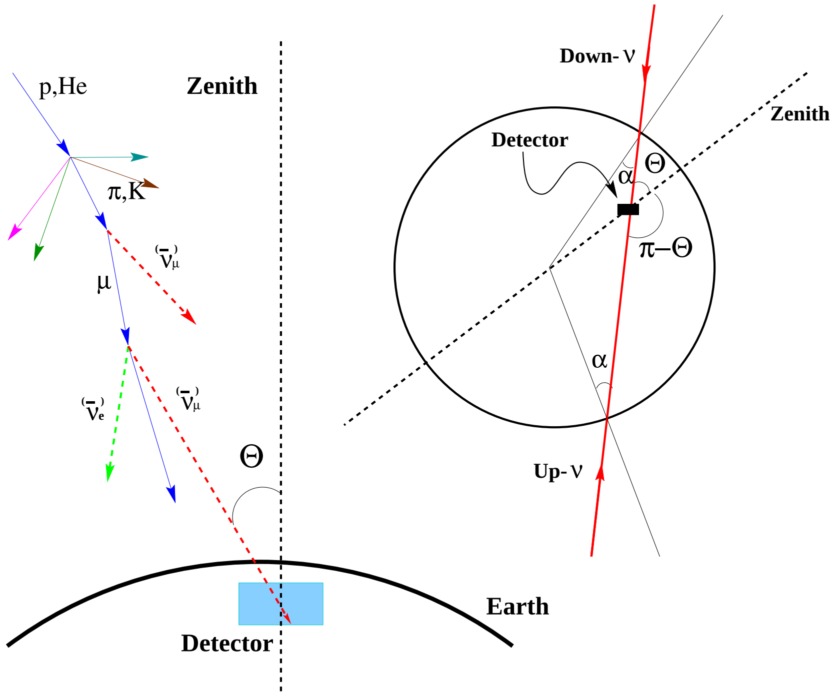

Figure 2.5: Sketch of the atmospheric neutrino detection principles.

neutrino flux per unit area is almost the same at any location on the Earth. If we consider the contribution to the flux from a point at zenith angle Θ (downward-going neutrinos) and from a point at zenith angle $\pi - \Theta$ (upward-going neutrinos), see Fig.2.5, the two quantities must have the same value. Therefore, in the no-oscillation hypothesis, the zenith angle distribution must be up-down symmetric, assuming no other phenomena affecting the neutrino angular distribution relative to the local vertical direction. Conversely, any deviation from up-down symmetry could be interpreted as an indication for neutrino oscillations.

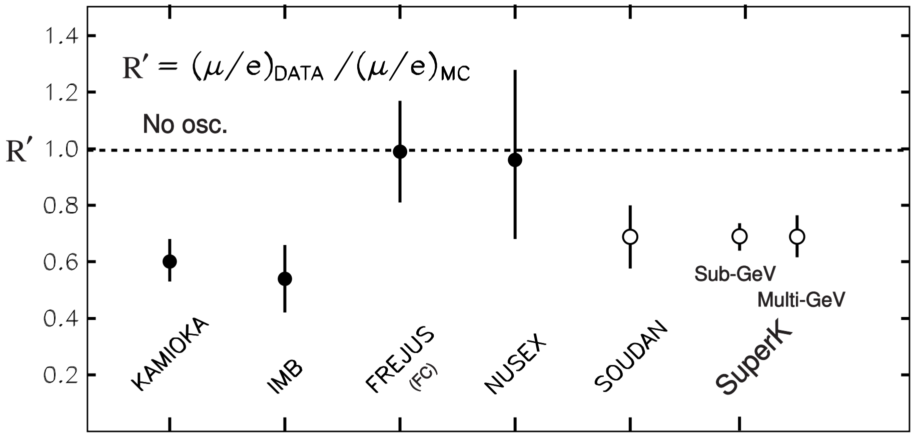

Figure 2.6: Compilation of the R' ratio (see text) measured by several atmospheric neutrino experiments [12].

2.5.1 Experimental results

Since the 1980's several underground detectors have studied atmospheric neutrinos. They are located below 1-2 km of rock and may detect neutrinos coming from all directions. Via charged current (CC) interactions, the ν_μ gives rise to a μ^- and thus to a track, the ν_e to an e^- and thus to an electromagnetic shower. The detectors can be roughly classified as tracking calorimeters (NUSEX [26], Fréjus [27], Soudan 2 [28]) and water Cherenkov detectors (IMB [29], Kamiokande [30], SuperKamiokande [31]); besides them, we have the Baksan [32] scintillation telescope and the MACRO detector [33].

A compilation of results on R' from different experiments is shown in Fig. 2.6 [12].

Early experiments

The first experiment to report, in 1986, a discrepancy between the observed and the predicted number of atmospheric muon neutrinos was IMB, a ring imaging water Cherenkov detector located in the Morton mine in Ohio (USA). Measuring ν_μ and ν_e from CC interactions, IMB found that the ratio of muons to electrons was smaller than expected. The measured double ratio was $R'_{IMB} = 0.60 \pm 0.06_{stat} \pm 0.07_{sys}$ [29].

Two years later, Kamiokande confirmed that the measured deficit of muon-like events was of the order of 40%. In that experiment, neutrino interactions were classified using the shape of Cherenkov rings on the phototubes on the wall of the cylindrical water container and through the recognition of muon decays. The measured double ratio was $R'_{Kam} = 0.60 \pm 0.06_{stat+sys}$ [30].

The same effect was not observed by two other experiments, NUSEX and Fréjus, both using fine-grained iron calorimeters. They reported for contained and semicontained events a measured number of events in agreement with Monte Carlo predictions. The measured double ratios were $R'_{NUSEX} = 1.0 \pm 0.3$ [26] and $R'_{Frejus} = 1.00 \pm 0.15_{stat} \pm 0.08_{sys}$ [27]. We have to notice the large statistical errors which affect the measurements, in particular of NUSEX.

The Baksan scintillation telescope detected upthroughgoing muons arising from ν_μ interactions in the rock below the detector. The average ν_μ energy for these events, $50 \div 100$ GeV, is larger than for the contained events measured by the other detectors. They did not find deviations from the predictions in the total number of events [32].

Later, the Soudan 2 tracking and shower calorimeter detector confirmed the anomaly in the ν_μ/ν_e double ratio for contained events (Fig. 2.6), SuperKamiokande confirmed the anomalous double ratio (Fig. 2.6), and provided a wealth of informations for sub-GeV and multi-GeV ν_μ, ν_e and for higher energy upthroughgoing and stopping muons. MACRO reported a global deficit in the total number of upthroughgoing muons ($\langle E_\nu \rangle \simeq 50$ GeV) and an anomalous zenith angle distribution, which disagrees with the MC predictions for a non oscillated ν_μ flux.

Results from the SuperKamiokande experiment

Atmospheric neutrinos are detected in SK by measuring the Cherenkov light generated by the charged particles produced in the neutrino CC interactions

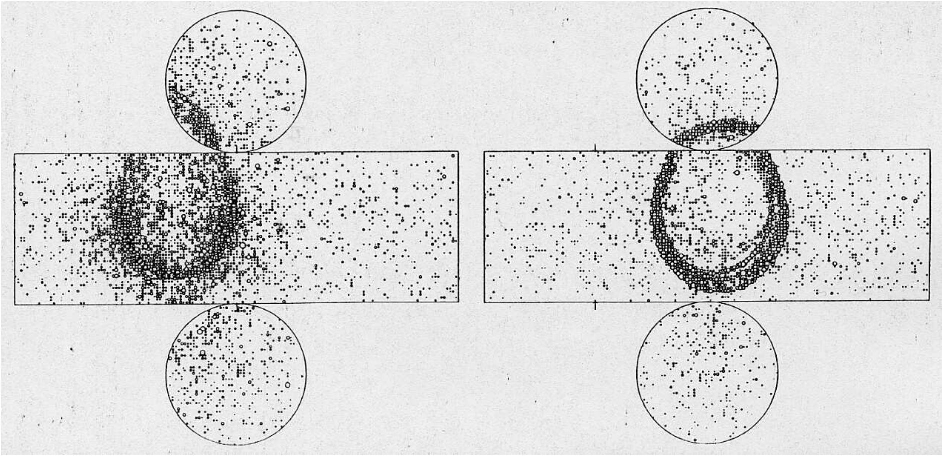

(a) (b)

Figure 2.7: Sharpness of Cherenkov rings produced in the SK detector by (a) an electron and (b) a muon.

with water nuclei. Thanks to the high PMT coverage, the experiment is characterized by a good light yield (~ 8 photo-electrons per MeV) and can detect events of energies as low as ~ 5 MeV.

The large detector mass and the possibility of clearly defining a large inner volume allow to collect a high statistics sample of *fully contained* events (FC) up to relatively high energies (up to ~ 5 GeV). The FC events have both the neutrino vertex and the resulting particle tracks entirely within the fiducial volume; they yield rings of Cherenkov light on the PMTs. The contamination from downward-going cosmic muons is drastically reduced by the containment requirement on the primary vertex coordinates. Fully contained events can be further subdivided into two subsets, the so-called *sub-GeV* and *multi-GeV* events, with energies below and above 1.33 GeV, respectively. The energies of FC events can be estimated by the thickness of the Cherenkov light rings, which allows to reconstruct the particle range. Another sub-sample, defined as the *partially contained* events (PC), is represented by those CC interactions where the vertex is still within the fiducial volume, but at least a primary charged particle, typically the muon, exits the detector without releasing in it

	Data	MC no osc.	$\langle E_\nu \rangle$ (GeV)
Sub-GeV e-like	2864	2668	0.6
Sub-GeV μ-like	2788	4073	0.6
Multi-GeV e-like	626	613	3
Multi-GeV μ-like	558	838	3

Table 2.3: Summary of the SK data. For e-like and μ-like Sub-GeV and Multi-GeV events, the number of measured events, the MC predictions for no oscillations and the approximate average energy are listed.

all its energy. In this case the light pattern is a filled circle. For these events the energy resolution is worse than for FC events. Finally, *upward-going muons* (UPMU), produced by neutrinos coming from below and interacting in the rock below the detector, are further subdivided into *stopping muons* ($\langle E_\nu \rangle \sim 7$ GeV) and *upthroughgoing muons* ($\langle E_\nu \rangle \sim 70 \div 80$ GeV), according to whether or not they stop in the detector. The different samples defined above explore different ranges of neutrino energies [34].

Particle identification in SuperKamiokande is performed using likelihood functions to parameterize the sharpness of the Cherenkov rings, which are more diffused for electrons than for muons, see Fig. 2.7. The algorithms are able to discriminate the two flavours with high precision (of the order of 98% for single track events).

The zenith angle distributions for e-like and μ-like sub-GeV and multi-GeV events are shown in Fig. 2.8. The electron-like events are in agreement with the MC predictions in absence of oscillations, while the muon data are lower than the no oscillation expectations. The number of measured and expected events are summarized in Table 2.3. The μ-like data exhibit an up/down asymmetry in zenith angle, while no significant asymmetry is observed in the e-like data [31]. For no oscillations, the up/down ratio is expected to be near unity for $E_\nu > 1$ GeV (above this value the effects due to the Earth magnetic field on cosmic rays are small).

The most recent value for the double ratio $R' = \frac{(\mu-like/e-like)_{DATA}}{(\mu-like/e-like)_{MC}}$ reported

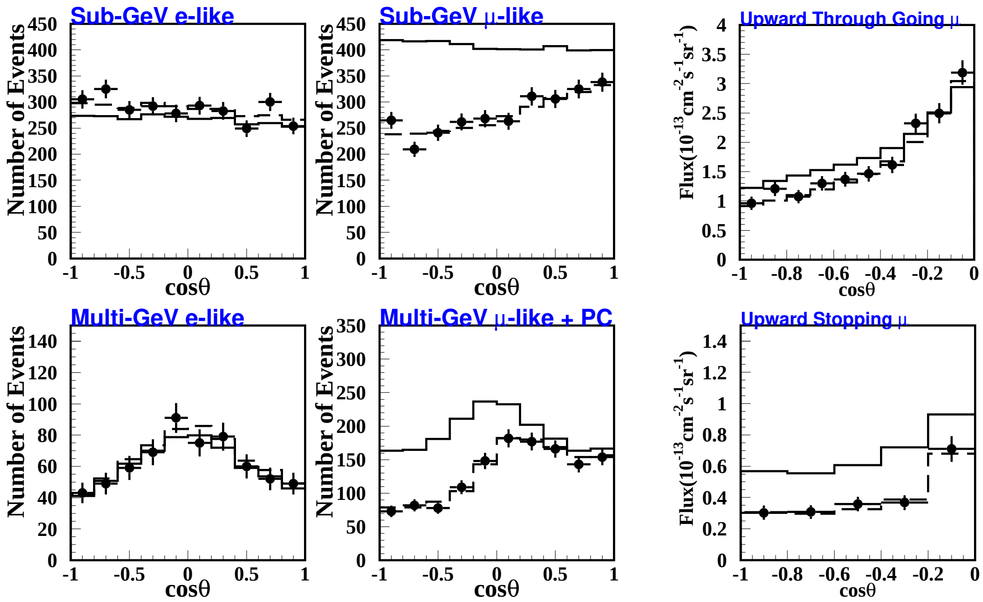

Figure 2.8: Zenith distributions for SK data (black points) for e-like and μ-like sub-GeV and multi-GeV events and for throughgoing and stopping muons. The solid lines are the no oscillation MC predictions, the dashed lines refer to $\nu_\mu \longleftrightarrow \nu_\tau$ oscillations with maximal mixing and $\Delta m^2 = 2.5 \cdot 10^{-3}$ eV^2.

by SK, based on 1289 days of data, is $0.638^{+0.017}_{-0.017} \pm 0.050$ for the sub-GeV sample and $0.675^{+0.034}_{-0.032} \pm 0.080$ for the multi-GeV sample (both FC and PC). The ratio between observed and expected numbers of e-like and μ-like events as a function of L/E_ν is shown in Fig. 2.9. The ratio e-like events/MC do not depend from L/E_ν while μ-like events/MC show a dependence on L/E_ν consistent with the oscillation hypothesis. Interpreting the muon-like event deficit as the result of $\nu_\mu \longleftrightarrow \nu_\tau$ oscillations in a two-flavour mixing scheme, SuperKamiokande computes an allowed domain for the oscillation parameters. The best fit using FC, PC, UPMU and MRING events [31] corresponds to maximal mixing and $\Delta m^2 = 2.5 \cdot 10^{-3}$ eV^2, Fig. 2.16.

SK reported also data on upthroughgoing muons, which agree with the predictions with an oscillated flux with the above parameters. Notice that the average energies are larger than in MACRO.

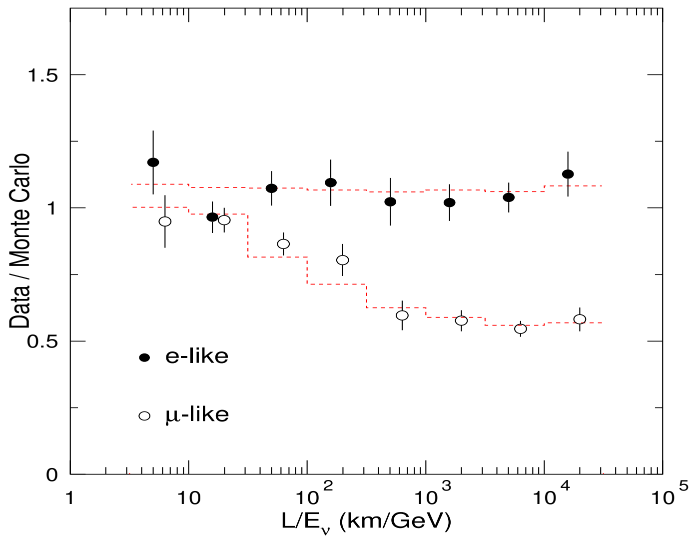

Figure 2.9: SK data: ratio between observed and expected number of e-like and μ-like events as a function of L/E_ν.

- $\boldsymbol{\nu_\mu \longleftrightarrow \nu_\tau}$ **against** $\boldsymbol{\nu_\mu \longleftrightarrow \nu_{sterile}}$

If the observed deficit of ν_μ is due to $\nu_\mu \longleftrightarrow \nu_{sterile}$ oscillations, then the number of events produced via NC interaction for up-going neutrinos should also be reduced. Moreover, in the case of $\nu_\mu \longleftrightarrow \nu_{sterile}$ oscillations, matter effects will suppress oscillations in the high energy ($E_\nu > 15$ GeV) region. The following data samples were used to search for these effects: (a) NC enriched sample, (b) the high energy ($E > 5$ GeV) PC sample and (c) upthroughgoing muons. The zenith angle distribution for each sample is shown in Fig. 2.10. The hypothesis test is performed using the up($-1 < \cos\Theta < -0.4$)/down($0.4 < \cos\Theta < 1$) ratio in samples (a) and (b) and the vertical($-1 < \cos\Theta < -0.4$)/horizontal($-0.4 < \cos\Theta < 0$) ratio in sample (c). The excluded regions obtained by a combined ((a),(b)and(c)) analysis and by the analysis of 1-ring-FC show that $\nu_\mu \longleftrightarrow \nu_{sterile}$ oscillations are disfavored with respect to $\nu_\mu \longleftrightarrow \nu_\tau$ oscillations at a C.L. of 99% [31].

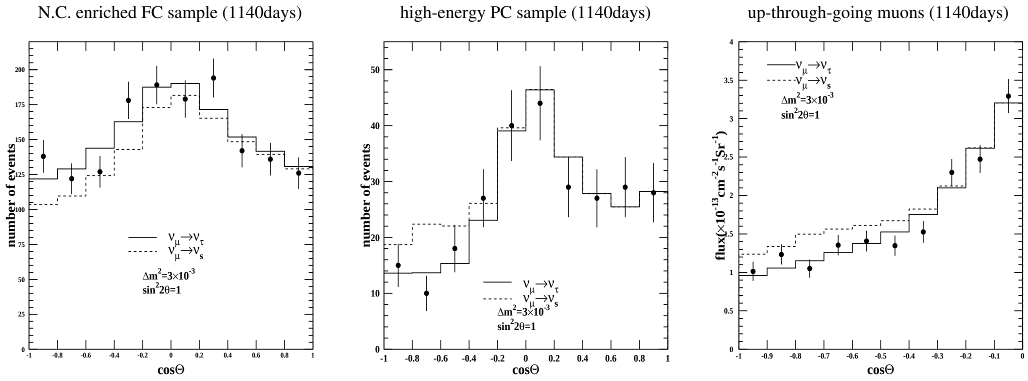

(a) (b) (c)

Figure 2.10: SK data: zenith angle distributions of (a) NC enriched sample, (b) high energy PC sample, (c) upthroughgoing muon sample.

Results from the Soudan 2 experiment

The Soudan 2 experiment uses a modular fine-grained tracking and showering calorimeter of 963 t. It is located 2100 m.w.e. underground in the Soudan Gold mine in Minnesota. The bulk of the mass consists of corrugated steel sheets interleaved with drift tubes. The detector is surrounded by an anticoincidence shield which covers the walls of the cavern. Topologies for contained events include single track and single shower events and multiprong events, see Fig. 2.11.

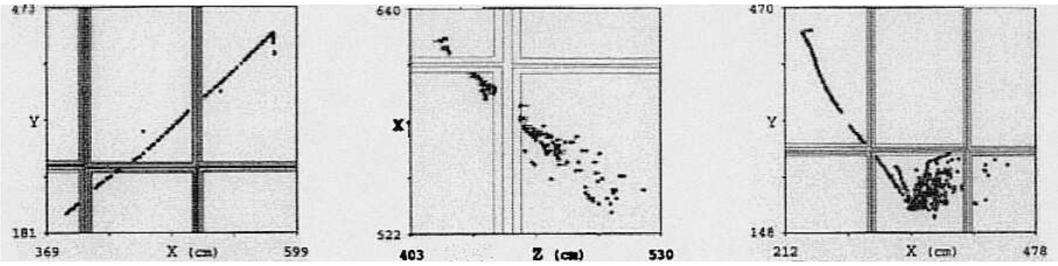

(a) (b) (c)

Figure 2.11: Topologies of contained neutrino events detected by the Soudan 2 detector: (a) single track, (b) single shower, (c) multiprong event.

	Data Raw	Data Back. removed	MC
Track	133	105.1 ± 2.7	193.1
Showers	193	142.3 ± 13.9	179.0

Table 2.4: Summary of the Soudan 2 Gold data.

An event having a leading, non-scattering track with ionization dE/dx compatible with that from a muon is a candidate CC event of ν_μ flavour; an event yielding a relatively energetic shower is a candidate ν_e CC event. Soudan 2 can follow the trajectory of μ events, reconstructing L with good precision ($\sim 0.1\%$); the energy is estimated by the muon range. Events without hits in the shield are called *Gold Events*, while events with two or more hits in the shield are called *Rock Events*.

A single track is due to a ν_μ, a single shower to a ν_e. The track and shower events for a 5.1 kt·yr exposure are summarized in Table 2.4, where they are compared with the MC predictions based on the Bartol neutrino flux [35]. After corrections for cosmic ray muon induced background, the Soudan 2 double ratio for the whole zenith angle range ($-1 \leq \cos\Theta \leq 1$) is $R'_{Sou2} = 0.68 \pm 0.11_{stat} \pm 0.06_{sys}$, which is consistent with muon neutrino oscillations.

Selecting a high resolution (HiRes) sample of events, for which the resolution in $\log(L/E_\nu)$ is better than 0.5, the flavour tagging is estimated to be correct for more than 92% of the events. After background subtraction there are 106.3 events of ν_μ flavour and 132.8 events of ν_e flavour. Using these events, whose mean energy is slightly higher, the double ratio is $R'_{Sou2-HiRes} = 0.67 \pm 0.12$. The $\log(L/E_\nu)$ distribution for ν_e and ν_μ charged current events compared to the no oscillation MC predictions normalized to the ν_e data is shown in Fig. 2.12. Notice that the ν_e data agree with the no oscillation MC predictions, while the ν_μ data are lower; this is consistent with oscillations in the ν_μ channel and no oscillations for ν_e.

The 90% C.L. allowed region in the $\sin^2 2\theta - \Delta m^2$ plane, computed using

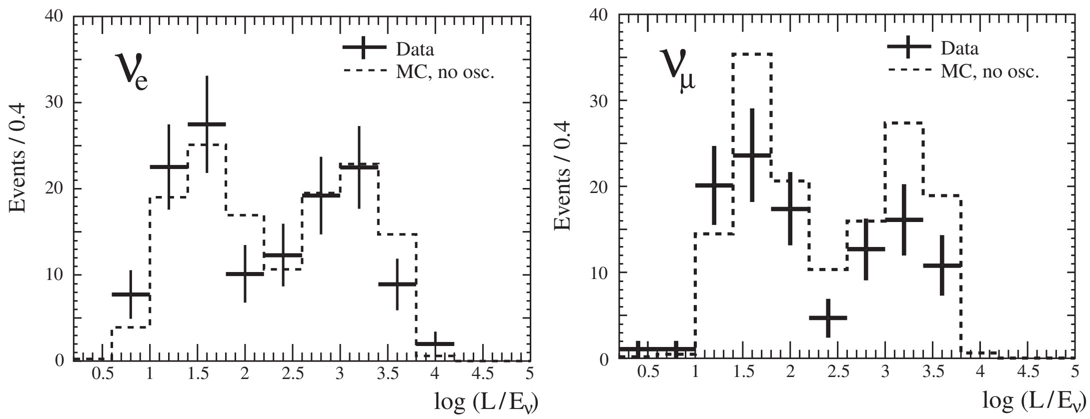

Figure 2.12: Distribution in $\log L/E_\nu$ for ν_e and ν_μ Soudan 2 CC HiRes events (black crosses) compared with the MC predictions for no oscillations (dashed line). Only statistical errors are shown. The MC is rate-normalized to the ν_e data.

the Feldman-Cousins method [36] is shown in Fig. 2.16, where it is compared with the allowed regions obtained by the SK and MACRO experiments.

Results from the MACRO experiment

The MACRO detector was located in Hall B of the Gran Sasso Laboratory, at an average rock overburden of 3700 hg/cm^2. For more technical details of the apparatus, see Chap. 4.

Fig. 2.13 is a vertical section of the detector and shows a sketch of the different topologies of ν_μ events: upthroughgoing muons, Internal Upgoing muons (IU$_\mu$), Upgoing Stopping muons (UGS$_\mu$) and Internal Downgoing muons (ID$_\mu$).

- **Upthroughgoing muons**

The *upthroughgoing muons* ($E_\mu > 1$ GeV) come from interactions in the rock below the detector of ν_μ with $\langle E_\nu \rangle \sim 50$ GeV. The tracking is performed with streamer tubes hits; the time information is provided by scintillation counters (T.o.F. method). The data refer to the full period of MACRO data

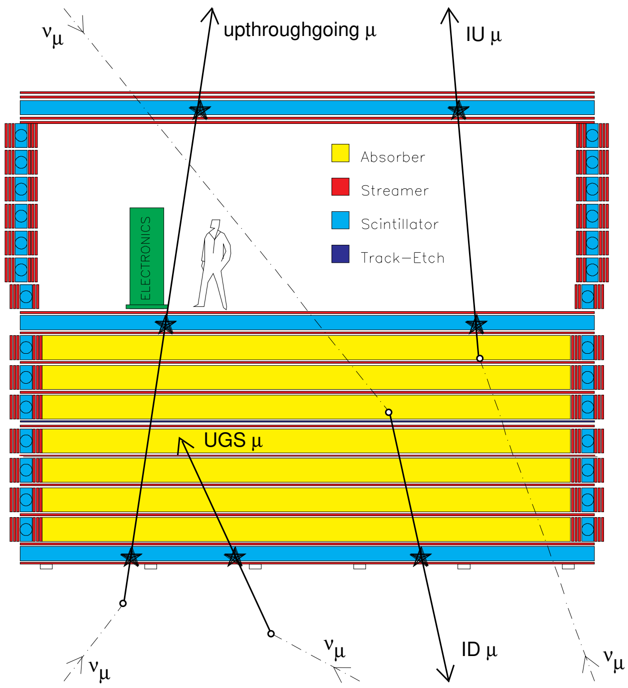

Figure 2.13: Vertical section of the MACRO detector. Event topologies induced by ν_μ interactions in or around the detector. IU_μ = semicontained Internal Upgoing μ; ID_μ = Internal Downgoing μ; UGS_μ = Upgoing Stopping μ; Upthroughgoing = upward throughgoing μ. The stars indicate the scintillator hits.

taking, 6.16 yr.

In the MC simulation, the neutrino flux computed by the Bartol group [35] is used. The cross sections for the neutrino interactions have been calculated using the deep inelastic parton distribution of ref. [37]. The propagation of muons to the detector has been done using the energy loss calculation in standard rock of ref. [38]. The uncertainty arising from the neutrino flux, cross section and muon propagation on the expected flux of muons is estimated to be $\sim 17\%$. This is mainly a scale error; the error on the shape of the angular distribution is considerably smaller, $\sim 5\%$.

In the angular range considered, $-1 < \cos\Theta < 0$, the MC prediction for upthroughgoing events is 1122 ± 191, while the observed number is 809; the

	Events	$MC_{\text{no osc}}$	$R = \text{Data}/MC_{\text{no osc}}$
Upthr.	809	1122 ± 190.7	$0.721 \pm 0.026_{stat} \pm 0.043_{sys} \pm 0.123_{th}$
IU	154	$285 \pm 28_{sys} \pm 71_{th}$	$0.54 \pm 0.04_{stat} \pm 0.05_{sys} \pm 0.13_{th}$
ID+UGS	262	$375 \pm 37_{sys} \pm 94_{th}$	$0.70 \pm 0.04_{stat} \pm 0.07_{sys} \pm 0.17_{th}$

Table 2.5: Summary of the MACRO events after background subtraction. For each topology the number of measured events, the MC predictions for no oscillations and the ratio $R = \text{Data}/MC_{\text{no osc}}$ are given.

ratio of the observed number of events to the expectation without oscillations is $R_{upthr} = (\text{Data}/MC_{\text{no osc}})_{upthr} = 0.721 \pm 0.026_{stat} \pm 0.043_{sys} \pm 0.123_{th}$.

Fig. 2.14a shows the zenith angle distribution of the measured flux of upthroughgoing muons; the MC expectation for no oscillations is indicated by the dashed line. The best result of the fit of the angular distribution and of the measured number of events, assuming $\nu_\mu \longleftrightarrow \nu_\tau$ oscillations, yields $\sin^2 2\theta = 1$ and $\Delta m^2 = 2.5 \cdot 10^{-3}$ eV^2 (solid line).

The 90% C.L. allowed region in the $\sin^2 2\theta - \Delta m^2$ plane, computed using the Feldman-Cousins method [36] is shown in Fig. 2.16, where it is compared with those obtained by the SuperKamiokande and Soudan 2 experiments.

- $\boldsymbol{\nu_\mu \longleftrightarrow \nu_\tau}$ **against** $\boldsymbol{\nu_\mu \longleftrightarrow \nu_{sterile}}$

Matter effects (§2.3.2) should produce different total number and different zenith distribution of upgoing muons. In Fig. 2.14b the measured ratio between the events with $-1 < \cos\Theta < -0.7$ and the events with $-0.4 < \cos\Theta < 0$ is shown (black point) [33]. In this ratio, most of the theoretical uncertainties on neutrino flux and cross sections cancel. The remaining theoretical error is estimated at $\leq 6\%$. MACRO measured 305 events with $-1 < \cos\Theta < -0.7$ and 206 with $-0.4 < \cos\Theta < 0$; the ratio is $R = 1.48 \pm 0.13_{stat} \pm 0.10_{sys}$. For $\Delta m^2 = 2.5 \cdot 10^{-3}$ eV^2 and maximal mixing, the minimum expected value of the ratio for $\nu_\mu \longleftrightarrow \nu_\tau$ is $R_\tau = 1.72$, while for $\nu_\mu \longleftrightarrow \nu_{sterile}$ is $R_{sterile} = 2.16$. We can conclude that $\nu_\mu \longleftrightarrow \nu_{sterile}$ oscillations (with any mixing) are disfavoured at the 99% C.L. compared to the $\nu_\mu \longleftrightarrow \nu_\tau$ channel with maximal mixing and $\Delta m^2 = 2.5 \cdot 10^{-3}$ eV^2.

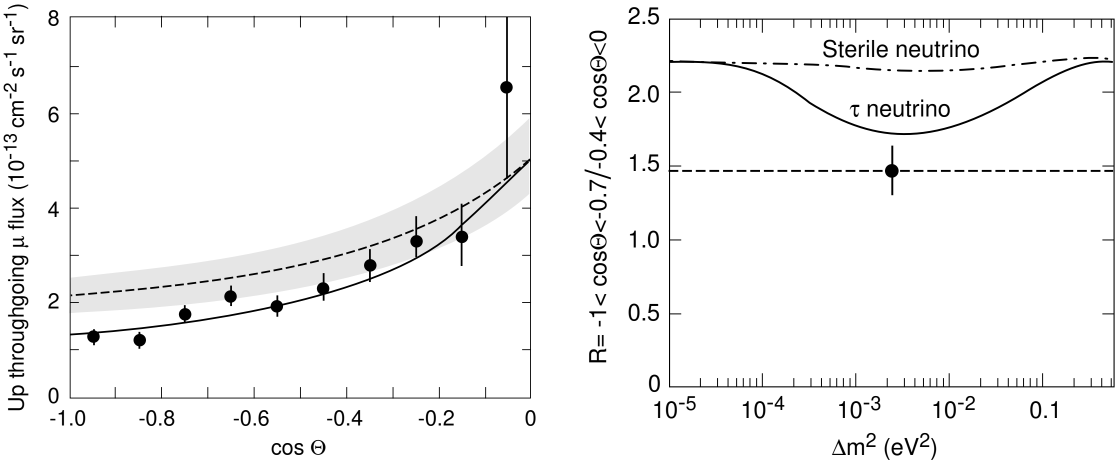

(a) (b)

Figure 2.14: (a) Zenith distribution for upthroughgoing muons in MACRO. The data (black points) have error bars with statistical and systematic errors added in quadrature. The shaded region shows the theoretical scale error band of $\pm 17\%$ on the normalization of the Bartol flux for no oscillations. The solid line is the fit to an oscillated flux which yields maximal mixing and $\Delta m^2 = 2.5 \cdot 10^{-3}$ eV^2. (b) Ratio of events with $-1 < \cos\Theta < -0.7$ to events with $-0.4 < \cos\Theta < 0$ as a function of Δm^2 for maximal mixing. The black point with error bar is the measured value, the solid line is the prediction for $\nu_\mu \longleftrightarrow \nu_\tau$ oscillations, the dotted-dashed line is the prediction for $\nu_\mu \longleftrightarrow \nu_{sterile}$ oscillations.

- **Low energy events**

The *semicontained upgoing muons* (IU) come from ν_μ interactions inside the lower apparatus, Fig. 2.13. Since two scintillation counters are intercepted, the T.o.F. method is applied to identify the upward going muons. The average parent neutrino energy for these events is ~ 4 GeV. If the atmospheric neutrino anomalies are the results of ν_μ oscillations with maximal mixing and $10^{-3} < \Delta m^2 < 10^{-2}$ eV^2, we expect a reduction of about a factor two in the flux of IU events, without distortion in the shape of the angular distribution.

The *up stopping muons* (UGS) are due to ν_μ interactions in the rock below the detector yielding upgoing muon tracks stopping in the detector; the *semi-contained downgoing muons* (ID) are ν_μ-induced downgoing tracks with vertex

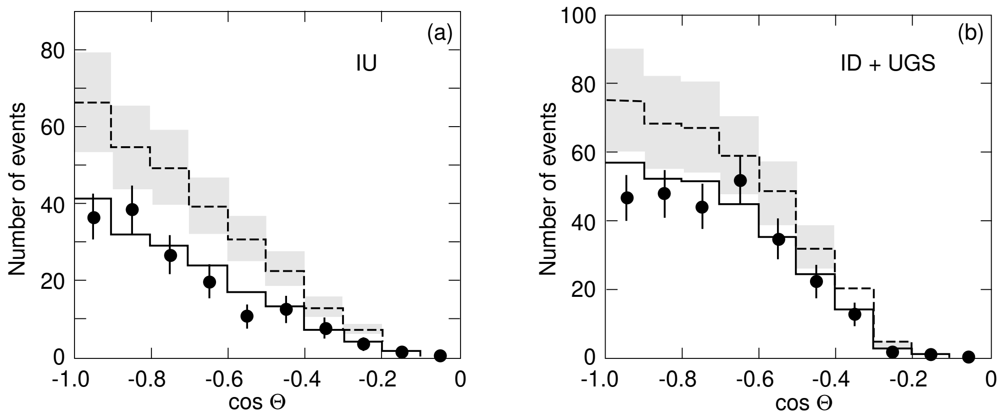

Figure 2.15: (a) Measured zenith distributions for the IU events and (b) for the ID+UGD events in MACRO represented by the black points. The shaded regions correspond to MC predictions assuming no oscillation. The full line is the expectation for $\nu_\mu \longleftrightarrow \nu_\tau$ oscillations with maximal mixing and $\Delta m^2 = 2.5 \cdot 10^{-3}$ eV^2.

in the lower MACRO, Fig. 2.13. The events are found by means of topological criteria; the lack of time information prevents to distinguish between the two subsamples. An almost equal number of UGS and ID events is expected. In case of oscillations, a 50% reduction in the flux of the UGS events is expected, while no reduction is expected for the ID events, coming from neutrinos which traveled ~ 20 km. For the sample of ID+UGS events, composed by 50% of ID and 50% of UGS events, a global reduction of $\sim 25\%$ is expected.

For the low energy data, the MC simulations use the Bartol neutrino flux and the low energy neutrino cross sections [39]. The MC prediction for IU events is $285 \pm 28_{sys} \pm 71_{th}$, while the observed number is $154 \pm 12_{stat}$; the ratio R_{IU} =(Data/MC$_{\text{no osc}})_{IU}$ is $0.54 \pm 0.04_{stat} \pm 0.05_{sys} \pm 0.13_{th} = 0.54 \pm 0.15$. The predictions for ID+UGS events is $375 \pm 37_{sys} \pm 94_{th}$, while the observed number is $262 \pm 16_{stat}$; the ratio R_{ID+UGS} =(Data/MC$_{\text{no osc}})_{ID+UGS}$ is $0.70 \pm 0.04_{stat} \pm 0.07_{sys} \pm 0.17_{th} = 0.70 \pm 0.19$.

The number of events and the angular distributions are compared with the predictions in Table 2.5 and Fig. 2.15. The low energy data show a uniform deficit of the measured number of events over the whole angular distribution

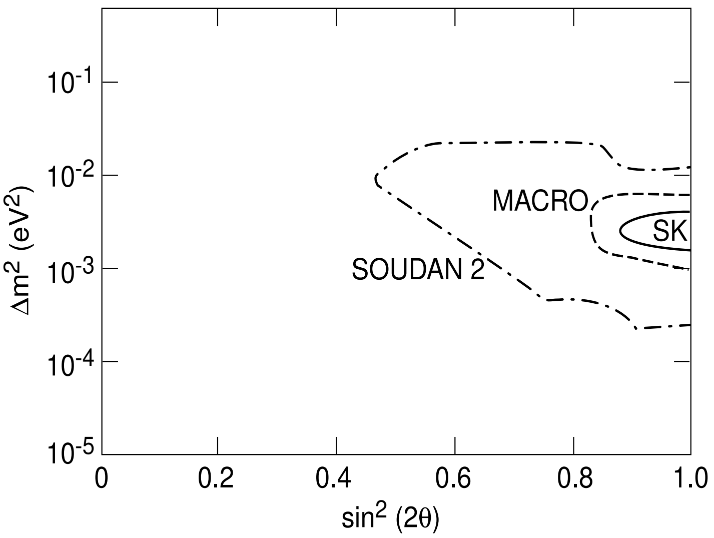

Figure 2.16: 90% C.L. allowed region contours for $\nu_\mu \longleftrightarrow \nu_\tau$ oscillations obtained by the SK, MACRO and Soudan 2 experiments.

with respect to the predictions; the data are in agreement with the predictions based on $\nu_\mu \longleftrightarrow \nu_\tau$ oscillations (continuous line) with the parameters obtained from the upthroughgoing muon sample.

2.6 Conclusions and outlook

In recent years, some experimental results provided hints for the existence of flavour mixing in the neutrino sector: the solar neutrino deficit and the atmospheric neutrino anomaly.

A global deficit of the solar ν_e flux measured by many experiments using different techniques can be interpreted as a signal of neutrino oscillations. Moreover, the SK and SNO results confirm the presence of different flavours in the solar neutrino flux reaching the Earth.

The results on atmospheric neutrinos obtained by the Soudan 2, MACRO and SuperKamiokande experiments were discussed in details. The observed number of ν_μ-induced muons disagree with the predicted values for the no oscillation hypothesis, while for ν_e-induced electrons there is no appreciable deviation from prediction. The ratio of muons to electrons normalized to the respective MC predictions enhances the anomaly. Moreover, the zenith angle distributions of upgoing muons are in agreement with the hypothesis of two flavour $\nu_\mu \longleftrightarrow \nu_\tau$ oscillations, with maximal mixing and $\Delta m^2 \sim 2.5 \cdot 10^{-3}$ eV^2.

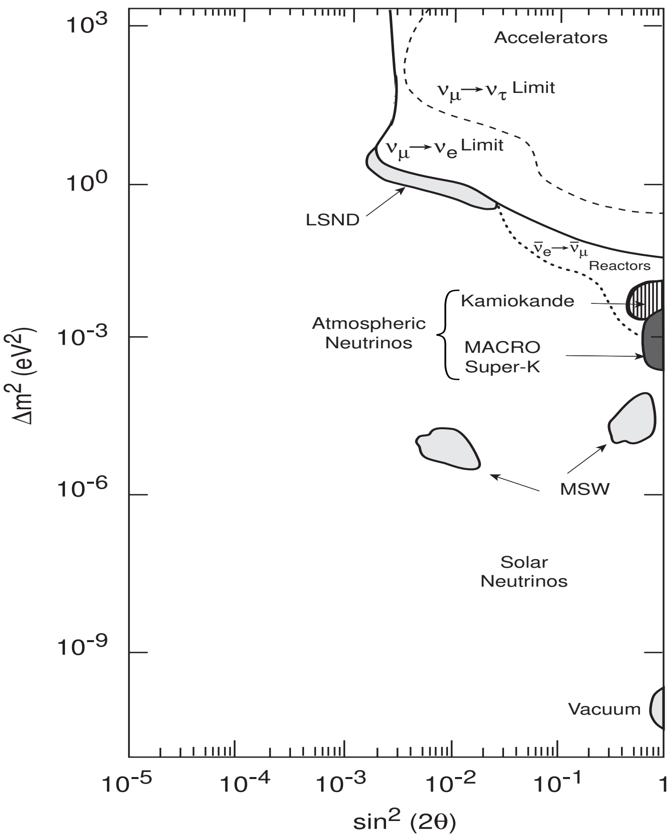

Figure 2.17: Global situation about neutrino oscillations. The reactor and accelerator experiments exclude the top-right regions in the plane considering two-flavour oscillations. The atmospheric neutrino experiments indicate $\nu_\mu \longleftrightarrow \nu_\tau$ oscillations with $\Delta m^2 \simeq 2.5 \cdot 10^{-3}$ eV^2 and $\sin^2 2\theta \simeq 1$. The solar neutrino experiments indicate oscillations in vacuum with $\Delta m^2 \simeq 10^{-10}$ eV^2 and $\sin^2 2\theta \simeq 1$ and in matter with $\Delta m^2 \simeq 10^{-5}$ eV^2 and low or large mixing. The figure should be slightly updated (see text).

A compilation of the allowed regions in the $\sin^2 2\theta - \Delta m^2$ plane obtained from the solar and atmospheric neutrino experiments is shown in Fig. 2.17. The limits obtained from reactor [40, 41] and accelerator [42] experiments are also shown. The reported data should be updated for solar and atmospheric neutrinos (see ref. [3] for solar neutrinos and Fig. 2.16 for atmospheric neutrinos).

The described experiments on atmospheric neutrinos are disappearance experiments; future atmospheric ν appearance experiments are under study. The main goals of these experiments are the study of the oscillation pattern, the appearance of ν_τ to really prove the oscillation hypothesis, the improvement in the measurements of the oscillation parameters, the discrimination of $\nu_\mu \longleftrightarrow \nu_\tau$ and $\nu_\mu \longleftrightarrow \nu_{sterile}$ oscillations, the detection of a possible $\nu_\mu \longleftrightarrow \nu_e$ contribution and complete informations on the oscillation matrix.

In the following chapters, I shall describe the study of the MACRO upthroughgoing muons in terms of L/E_ν. The energy of upthroughgoing events, induced by ν_μ with $\langle E_\nu \rangle \sim 50$ GeV, is estimated through the muon Multiple Coulomb Scattering (MCS) in the absorbers. The use of the limited streamer tubes in "drift mode" (Chap. 5), by using the TDCs of an electronic system designed for magnetic monopole searches, allows to improve the MACRO space resolution of a factor 3.5, from $\simeq 1$ cm to $\simeq 3$ mm. A neural network approach can estimate event by event the muon energy up to $E_\mu \sim 40$ GeV, corresponding to $E_\nu \sim 200$ GeV. Then I shall present the L/E_ν distribution and the allowed regions for the oscillation parameters in the $\sin^2 2\theta - \Delta m^2$ plane.

Chapter 3

Atmospheric neutrino flux calculations

3.1 Introduction

The existing data on atmospheric neutrinos, see §2.5.1, show convincing evidence for the existence of new physics, based on the observation of three effects: (i) a measured ν_μ/ν_e ratio smaller that the expectation [28, 31], (ii) the detection of a strong up/down asymmetry for μ-like events [31], and (iii) the distortion of the zenith angle distribution of ν_μ-induced upgoing muons [33]. The atmospheric ν fluxes have two properties that can be predicted in a model independent way: (i) the fluxes are up/down symmetric, that is $\phi_{\nu_\alpha}(E_\nu, \Theta) \simeq \phi_{\nu_\alpha}(E_\nu, \pi - \Theta)$; ($ii$) the fluxes of ν_e and ν_μ are strictly related. Therefore, the qualitative results of SK [31], showing a suppression of μ-like relative to e-like events and of upgoing (long L) relative to downgoing (short L) events, can indeed be considered as a model independent signature of new physics. Also the global deficit and the distortion of the zenith angle distribution of ν_μ-induced muons measured by the MACRO experiment can be interpreted as strong indications for neutrino oscillations.

The calculations of the atmospheric neutrino fluxes have been performed by the HKKM group [43] and by the Bartol group [35]. Both HKKM and

Bartol models are originally based on a one-dimensional (1-D) approximation: it implies that the transverse momentum of all secondary particles (hadrons, charged leptons and neutrinos) can be neglected, so that the secondary particles are assumed to be collinear with the parent primary cosmic ray. This approximation is reasonable in the multi-GeV region (the region of interest for upthroughgoing muons), while in the sub-GeV region it neglects an enhancement of the ν flux on the horizontal direction [44].

Several elements enter in the calculation of the atmospheric ν fluxes: the primary cosmic ray (c.r.) fluxes, the geomagnetic effects, the hadronic cross sections, the model for the c.r. shower development and the ν cross sections. In this chapter, I shall describe in details the contributions of these elements to the neutrino flux, giving also an estimate of their uncertainties.

3.2 The primary cosmic ray spectra

The primary cosmic ray spectrum is a fundamental input in the calculation of the atmospheric ν fluxes.

The algorithm used in all the atmospheric ν calculations to obtain the primary cosmic ray fluxes as a function of position and angle is based on two steps: (i) the primary cosmic rays are isotropic; (ii) the flux arriving at an imaginary surface in the vicinity of the Earth (the "top of the atmosphere") is equal to the isotropic primary flux after the subtraction of all "forbidden" trajectories. A trajectory is "allowed" if the back-tracking of the particle in the geomagnetic field from the interaction point shows that it reaches large distances from the Earth, otherwise it is "forbidden". The concept of allowed and forbidden trajectories in the Earth magnetic field $\vec{B}$ is illustrated in Fig. 3.1, for a ν detected by the SK experiment.

The theoretical basis for the subtraction algorithm is based on the fundamental assumptions that the cosmic ray spectrum in the absence of the Earth is isotropic, and that the field around the Earth is well described by a static

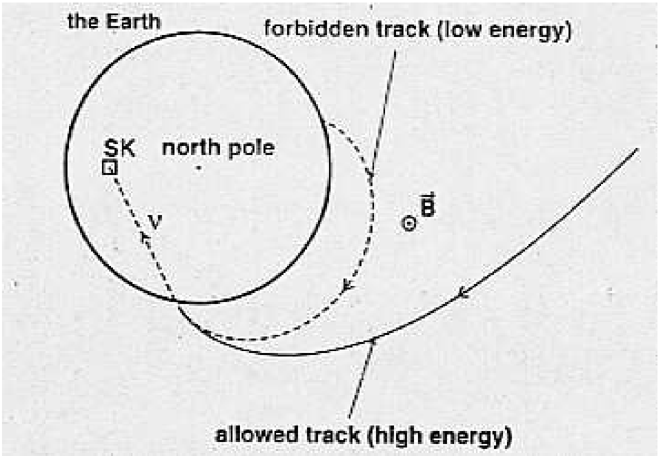

Figure 3.1: Typical allowed (solid line) and forbidden (dashed line) tracks of incident cosmic rays giving a neutrino incident on the SK detector.

purely magnetic field. The Liouville theorem states that the density of points in phase space volume is constant.

The flux $\phi(\vec{p}, \vec{x})$ is in fact proportional to the phase space density for relativistic particles ($\vec{p}$ and $\vec{x}$ indicate the momentum and the position of the particle, respectively); since the momentum of a charged particle in a magnetic field is constant, the differential flux $\phi(\vec{p}, \vec{x}(t))$[1] along a particle trajectory is constant. So, if the flux is isotropic at large distances from the Earth, then the flux in a small cone around any trajectory is constant and independent from the position. If a particle can reach the Earth, the momentum spectrum and the angular distribution around it are not deformed.

The described method has recently found a direct confirmation from the AMS [47] data. The AMS detector took data during a ten days flight aboard a space shuttle traveling on an orbit inclined of $51.7°$ with respect to the equator. During the flight, the fluxes of charged particles have been observed in a range

[1] The time dependence is connected with a modulation of the low energy component due to the solar activity (cycle of ~ 11 years) which induces fluctuations in the geomagnetic field [45]. The influence of the solar wind is sizeable ($\sim 15 \div 20\%$) for neutrino energies of 1 GeV or below and only at high geomagnetic latitudes (where the geomagnetic effect is minimal), while it becomes negligible at ~ 2 GeV [46].

of different magnetic latitudes. For allowed trajectories, the p fluxes in different regions are equal within statistical and systematic errors (with an uncertainty $\sim 10\%$). This confirms the assumption that the primary c.r. fluxes reaching two antipodal regions are equal; this is essential for the interpretation of the up/down asymmetry of μ-like events.

3.2.1 The primary c.r. composition

The spectrum of cosmic rays incident at the top of the atmosphere consists of protons, helium and heavier nuclei. The range of neutrino energies relevant for ν-induced muons is $1 \leq E_\nu \leq 10^3$ GeV [48]. The corresponding range of primary energy-per-nucleon is about a factor ten higher. The all-nucleon spectrum is dominated by hydrogen and helium; the percentage of heavier nuclei is expected to increase with energy. Ref. [49] shows, for example, that hydrogen contributes about 81 (68)% of the intensity at 10 (10^4) GeV and helium 72 (70)% of the remainder. The overall uncertainty is dominated by the uncertainty in the measurements of the hydrogen spectrum. The fraction of helium is crucial for determining the charge muon ratio and the $\nu/\overline{\nu}$ ratios because this is the origin of most of the incident neutrons. Heavy nuclei may become more important around 10^5 GeV/nucleon.

Recent data of the Caprice [50], AMS [47], BESS [51] and IMAX [52] experiments allowed a better determination of the proton fluxes, up to ~ 100 GeV/nucleon, Fig. 3.2. In the same figure, the HKKM [43] and Bartol [35] predictions are shown for comparison.

For the calculations, the Bartol group used the all-nucleon spectrum with an extrapolation based originally on the data summary of ref. [53] and extended to higher energy by including data from ref. [54] and other more recent data. At energies above 10^4 GeV/nucleon only the measurements of ref. [55] were used.

The data collected from the direct measurements of the primary protons, helium and heavier nuclei made with balloon and satellite experiments show

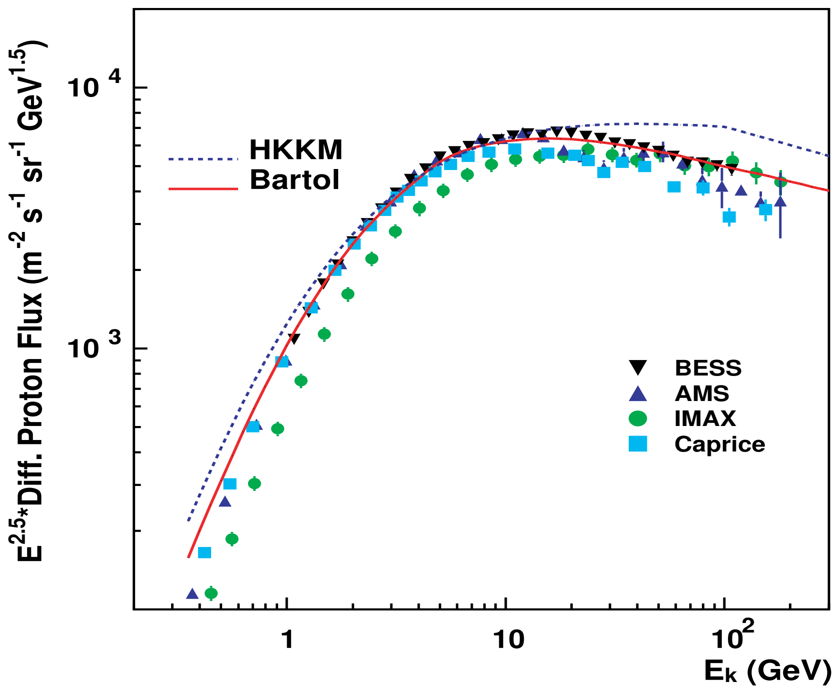

Figure 3.2: Primary cosmic ray proton fluxes measured by the BESS [51], AMS [47], IMAX [52] and Caprice [50] experiments (full symbols). The HKKM [43] (dashed line) and Bartol [35] (solid line) flux calculations are shown for comparison.

that, up to $\sim 10^4$ GeV, the envelope of the different measurements covers a range of about 30%. Thus a $\pm 15\%$ uncertainty is assigned to the all-nucleon spectrum in this energy range. Since primaries with $E > 10^4$ GeV/nucleon contribute only about 15% of the flux of upward muons, uncertainties at the level of $20 \div 30\%$ above this energy increase the uncertainty in the upwardgoing muon rate only by a few per cent.

The low energy part of the spectrum (< 20 GeV) is affected by the geomagnetic field and by the modulation of the solar wind, both of which prevent some fraction of the low energy galactic cosmic rays from reaching the atmosphere to produce secondaries. These effects are of great importance especially for the $\lesssim$ GeV neutrinos, which are responsible for contained neutrino interactions.

3.3 Geomagnetic effects

The trajectories of all charged particles in cosmic ray showers are curved because of the presence of the geomagnetic field. This effect is relevant for relatively low energy primary particles. If we define a system of coordinates with the z axis pointing up, the x axis pointing towards magnetic north and the y axis completing a right-handed system pointing towards the magnetic west, positive particles traveling east are bent up, while negative particles with the same initial direction are bent down [56]. The reverse happens for particle traveling in the west-ward direction.

The bending of the primary particles is a factor determining the average altitude of the primary interactions and the zenith angle distribution of the primaries at the interaction point.

Let us study the trajectories of two protons on allowed trajectories crossing an imaginary spherical surface above the Earth with the same zenith angles and different azimuth angles, with one particle traveling towards east and the other towards west. If the two trajectories are approximated as straight lines, the distributions of altitude of the interaction point $h_{\rm int}$ for the two particles are identical. Since the east-going particle is bent up and the west-going one is bent down, the first particle will on average interact higher and more "horizontally" in the Earth atmosphere:

$$\langle h_{\rm int}\rangle_E > \langle h_{\rm int}\rangle_W \quad , \quad \langle \cos\Theta_0^{\rm int}\rangle_E < \langle \cos\Theta_0^{\rm int}\rangle_W \tag{3.1}$$

The inequalities (3.1) result in an enhancement of the east-west effect for the neutrinos. The average number of neutrinos produced in a shower is larger when the primary particle interacts higher: the muons have a longer pathlength for decay, the shower develops in a medium of lower density, where the decays of mesons is enhanced, and muons lose less energy before decay. For the same reasons, more inclined showers produce more neutrinos.

Neutrinos produced in the decay of positive (negative) muons in showers of east-ward (west-ward) traveling primaries will be on average more "horizontal" than the primary particle; conversely, the neutrinos produced in the decay of positive (negative) muons in showers of west-ward (east-ward) traveling primaries will be on average more "vertical" than the primary particle. Fig. 3.3 shows the relation between the directions of the primary particle and of the neutrinos produced in muon decays.

In summary, the effect of the magnetic bending of the muons results in an enhancement for the flux of the neutrinos produced in the decay of μ^+ (ν_e and $\overline{\nu}_\mu$) traveling towards east and a suppression when the particles travel towards west. The net effect is a *positive* contribution to the east-west asymmetry. The effect of magnetic bending is opposite for the flux of neutrinos produced in the decay of μ^- ($\overline{\nu}_e$ and ν_μ), giving a global *negative* contribution to the east-west asymmetry.

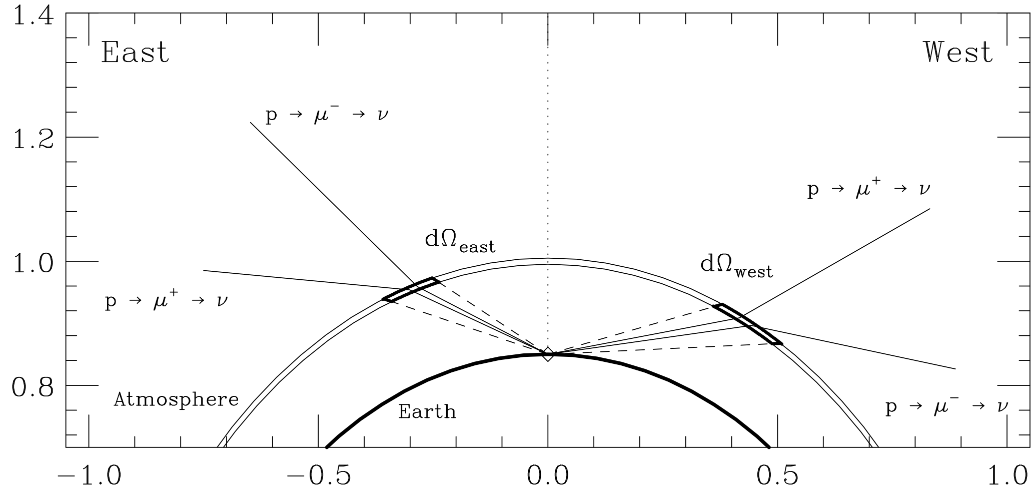

Figure 3.3: Relation between the directions of the primary particle and of the detected neutrinos produced in muon decays.

The magnetic bending of the muons has to be combined with the asymmetry generated by the geomagnetic effects on the primary particles; this results in an equal contribution to the asymmetry of all neutrino types.

3.4 Three-dimensional effects

The collinear approximation leads to an incorrect angular distribution of neutrinos at the Earth surface, which is relevant especially in the sub-GeV energy range [44, 57, 58]. In fact, low energy neutrinos have a large average angle $\langle \Theta_{0\nu} \rangle$ with respect to the primary particle direction. Moreover, they interact leading to a charged lepton, whose emission direction may be considerably different from the neutrino one.

Recently, a three-dimensional (3-D) description of the hadronic processes involved in the shower development was made using the FLUKA (FLUctuating KAskade) simulation package [44]. It is a Monte Carlo code for the interaction and transport of particles, containing detailed models of electromagnetic, hadron-hadron and hadron-nucleus interactions in the range from the MeV scale to the many-TeV one. A spherical representation of the Earth and of the surrounding atmosphere is implemented. The atmosphere is described as a medium composed by a mixture of N, O and Ar, arranged in 51 concentric spherical shells with density scaling according to the known profile of the standard atmosphere. Primary particles, sampled from a continuous spectrum, are injected at the top of atmosphere, at about 100 km of altitude. The primary flux is assumed to be uniform and isotropic, the flux of all secondary products is scored at different heights in the atmosphere and at the Earth boundary. Therefore, the code gives, besides neutrino fluxes, the flux of muons and hadrons.

A first result of the full simulation concerns the distribution of the angle between a neutrino crossing the Earth surface and the primary nucleon direction in different ranges of neutrino energy. From the distributions of $\Theta_{0\nu}$ for ν_μ [44], in the multi-GeV region the collinear approximation is reasonable, while in the sub-GeV region the average angle with respect to the primary direction is quite large, according to $\langle \Theta_{0\nu} \rangle \simeq 4.3^\circ / E_\nu(\mathrm{GeV})$.

If the geomagnetic effects are absent and the zenith angle dependence of the neutrino yield is negligible, a 1-D calculation predicts an isotropic neutrino flux, while the 3-D calculation predicts an enhancement of the ν flux on the horizontal plane, that is more important with increasing $\langle\Theta_{0\nu}\rangle$ (that is for decreasing E_ν) [44, 57].

The enhancement on the horizontal plane for low energy ν is difficult to observe directly because of the poor experimental angular resolution of the existing detectors. Since it implies a different pathlength distribution for the neutrinos, it could in principle have some consequences, for example, on the Δm^2 allowed regions. Preliminary analysis of SK suggest that the effect on the allowed region is only a modest shift.

3.5 Hadronic interactions

The most important informations needed about the interactions of primary protons with air are the forward inclusive cross sections for pion and kaon production. The important range of interaction energies extends up to ~ 100 GeV for sub-GeV events and ~ 1 TeV for multi-GeV events.

To describe the hadronic interactions, it is useful to characterize the inclusive cross sections by their moments, weighted by the shape of the primary spectrum. For example, the contribution of pions is approximately proportional to

$$Z_{p\pi^\pm} = \int_0^1 x^\gamma \frac{\mathrm{d}N_{p\pi}}{\mathrm{d}x}\,\mathrm{d}x \tag{3.2}$$

where $\mathrm{d}N/\mathrm{d}x$ is the distribution of charged pions produced in collisions of protons with nuclei in the atmosphere, $x = E_\pi/E_p$ and γ is the integral spectral index of the primary cosmic ray spectrum. The corresponding factors $Z_{pK^\pm}$, Z_{pK^0}, $Z_{p\pi^0}$, Z_{pp}, etc., are defined analogously.

Fig. 3.4 shows the distributions of π^+ produced in p-Nitrogen interactions obtained with the Bartol [35] and FLUKA [44] interaction models, compared with the available data. As we can observe, the FLUKA model predicts that a smaller fraction of the primary energy is converted into charged pions; this results in smaller fluxes, both for ν_e and for ν_μ, Fig. 3.5.

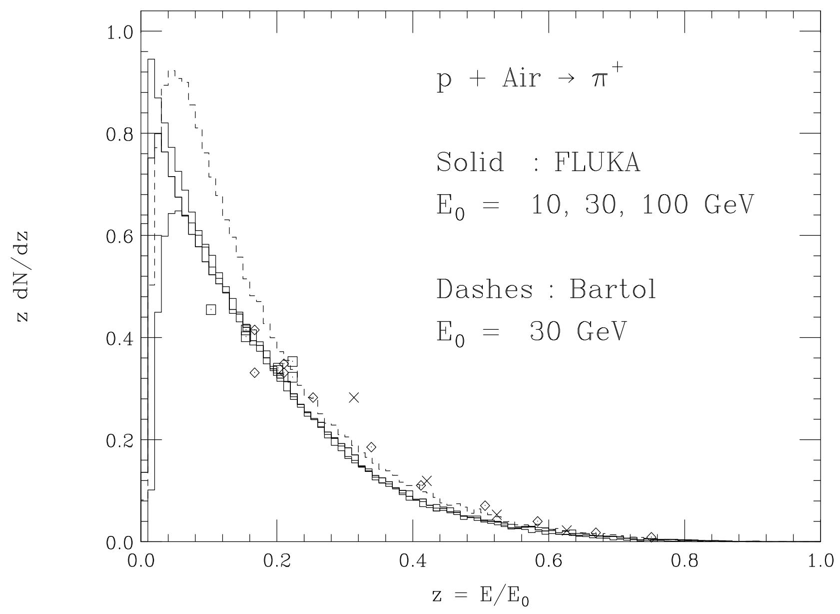

Figure 3.4: Inclusive differential cross section for π^+ production obtained by the Bartol [35] and FLUKA [44] models.

Studies of the A-dependence of inclusive cross sections on a variety of nuclear targets (excluding hydrogen) showed a significant variation in the fragmentation region, with a tendency for the K/π ratio to increase with target mass [59]. Production of both pions and kaons is enhanced in collisions on nuclear targets, but kaons may be more enhanced than pions. Associated production of kaons through $p \to \Lambda K^+$ in the fragmentation region accounts for the large ratio of Z_{pK^+}/Z_{pK^-}, since K^- are produced only through K^+/K^- pair production in the central region.

Production of K^+/K^- pairs is determined in TARGET by the energy-dependent multiplicity of K^- [60], with an assumed enhancement of 1.45 for target "air" nuclei ($A = 14.5$). The resulting distributions of produced $\pi^\pm$ and $K^\pm$ agree with the existing $19 \div 24$ GeV/c data [59].

The increasing (decreasing) of the K/π ratio results in larger (smaller) ratio vertical/horizontal (V/H) events, because the decay of a high momentum $K^\pm$

is easier than the decay of a $\pi^{\pm}$ of the same momentum, due to the shorter lifetime and larger mass. Kaons with E_K of few hundreds GeV decay for all zenith angles with a probability close to unity and give an approximately isotropic contribution to the upgoing muon flux, while $\pi^{\pm}$ decay more easily when inclined and give a contribution peaked for horizontal directions.

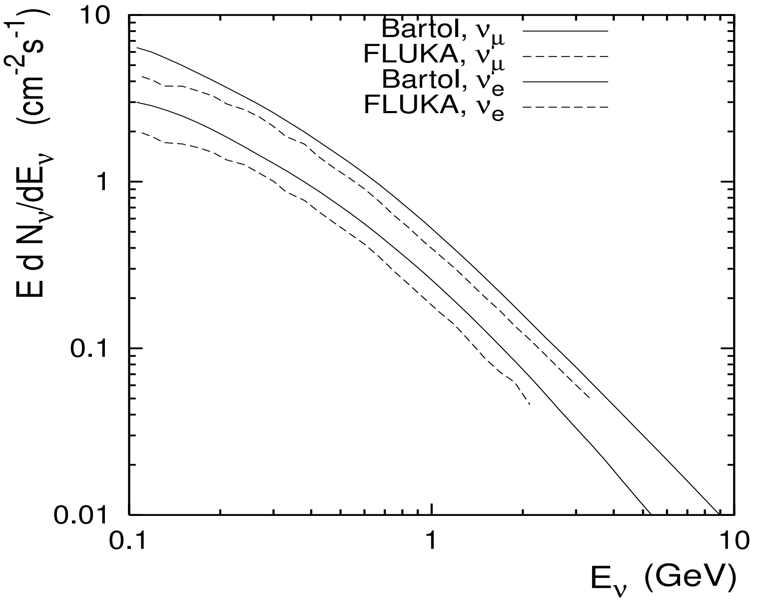

Figure 3.5: Fluxes of atmospheric ν_μ, ν_e from the Bartol (solid lines) [35] and FLUKA (dashed lines) [44] models.

The distribution of secondary nucleons is also important because a significant fraction of the neutrino production occurs in secondary or tertiary interactions of the nucleons. Neutral pions and η mesons are also to be considered because the energy deposited in the electromagnetic part of the cascade is not available for production of neutrinos.

The Bartol calculation [35] uses a phenomenological hadronic event generator (TARGET) developed for cosmic ray cascade simulations. FLUKA [44] uses a more sophisticated microscopic model of particle production with intranuclear cascading. It incorporates the event generator as an integral part of a cascade code capable of simulating interactions and cascades in complex detector geometries.

For the ν fluxes with $E_\nu \gtrsim 1$ GeV, calculated with the Bartol and FLUKA models assuming the same primary c.r. fluxes, the main difference is in the absolute normalization of $\sim 15\%$. Both models assume the approximate validity of Feynman scaling for projectile particles with $E_0 > 20$ GeV (Fig. 3.4). In fact, the spectrum of secondary particles produced with a Feynman scaling inclusive distribution, from a power law primary spectrum is simply proportional to the primary spectrum, independently from the (scaling) shape of the differential cross section [61].

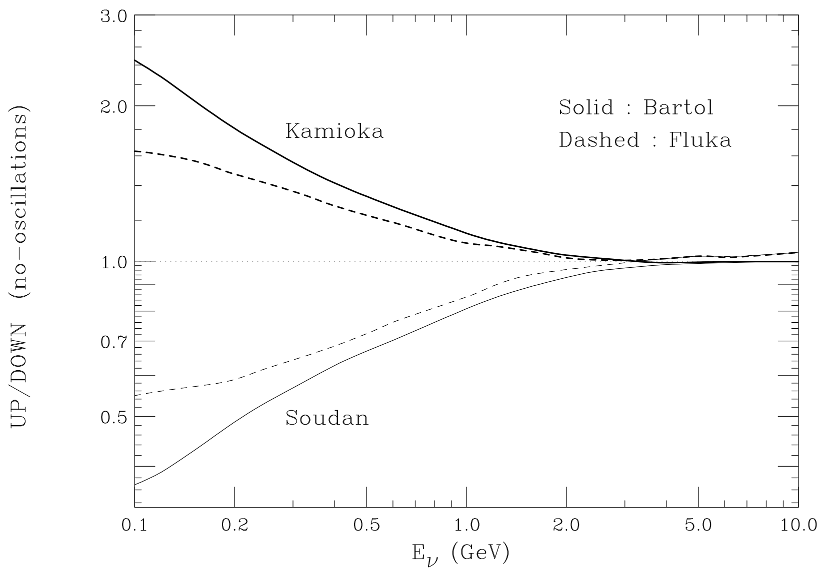

Figure 3.6: Predictions for the no oscillation up/down ratio for neutrinos with the Bartol [35] and FLUKA [44] models.

The difference between the Bartol and FLUKA models is more important in the sub-GeV regions, reflecting larger differences in the modeling of low energy interactions ($E_0 \lesssim 10$ GeV) when Feynman scaling is not a good approximation. The Bartol calculation predicts for this region a larger ν yield. This has some important consequences for the up/down asymmetry in the absence of oscillations. This is illustrated in Fig. 3.6, that shows, as a function of E_ν, the up/down ratio calculated in the absence of oscillations at the Kamioka and Soudan sites, using the same primary flux, and the two interaction models.

The ratio is approximately unity for $E_\nu \gtrsim 2$ GeV, but the up/down symmetry is broken by geomagnetic effects at lower energy. For SK, the no oscillation downgoing flux is smaller than the upgoing one, because the detector is placed near the magnetic equator, and the low energy downgoing primary flux is more strongly suppressed by the geomagnetic field, while the reverse happens for the Soudan site (located closer to the magnetic pole). It is important to note that the Bartol calculation, with a larger ν yield for low energy primaries, has a large no oscillation intrinsic asymmetry.

3.5.1 Uncertainties on the production cross sections

To estimate the uncertainties in the neutrino fluxes arising from uncertainties in the hadronic interactions, we have to consider the contributions defined in Eq. (3.2).

Inspection of the analytic approximations for neutrino and muon fluxes from power-law primary spectra is sufficient to determine which are the most important sources of uncertainty in different ranges of primary energy. For vertically incident leptons with energy below 100 GeV, approximately 95% of muons and 65% of ν_μ come from pions, whereas above 1 TeV about 50% of muons but less than $\sim$ 10% of ν_μ come from decay of pions. Most of the remainder come from decay of charged kaons. For horizontal leptons, this transition region is shifted to higher energy, so that kaons are less important for production of horizontal ν_μ-induced muons.

The relative importance of kaons for production of neutrinos at high energy is a consequence of the kinematics of meson decay coupled with the primary spectrum. In the low energy region, the uncertainties in both the muon and the neutrino fluxes are dominated by the uncertainty in pion production, as represented by $Z_{p\pi}$. At high energy, the dominant source of uncertainty in the neutrino flux is the kaon production.

Considering all the estimates, the $Z_{p\pi^\pm}$ cover a range of approximately $\pm12\%$. The corresponding range for $Z_{pK^\pm}$ is $\pm17\%$. These numbers are used to estimate the uncertainty in the expected flux of neutrino-induced muons.

3.6 The neutrino fluxes at high energy

The fluxes of atmospheric ν decrease rapidly with increasing energy, therefore the rate of interactions of high energy neutrinos in the detector fiducial volume is small; the fluxes of muon neutrinos can be studied through the study of upgoing muon events. These measurements allow to obtain information about the survival probability $P(\nu_\mu \rightarrow \nu_\mu)$ and to discriminate between the oscillation hypothesis and alternative mechanisms characterized by transition probabilities with different energy dependences.

The study of upgoing muons is also important for the discrimination between the $\nu_\mu \longleftrightarrow \nu_\tau$ and $\nu_\mu \longleftrightarrow \nu_{sterile}$ hypothesis. The two hypothesis can be separated because in the case $\nu_\mu \longleftrightarrow \nu_{sterile}$ the oscillation parameters are modified by matter effects (§2.3.2), which become important for $E_\nu/|\Delta m^2| > 10^3$ GeV/eV^2.

The measurement of the effects of oscillations on high energy ν_μ and $\overline{\nu}_\mu$ implies a direct comparison of the upgoing muon data with a calculation. The shape of the upgoing muons angular distribution is particularly important, because it can be distorted by oscillations or other forms of new physics. In the presence of standard oscillations, the shape is distorted since vertical neutrinos are suppressed more strongly than horizontal ones. The no oscillation shape can be understood qualitatively as the result of the competition between decay and interaction for the parent mesons ($\pi^\pm$ and $K^\pm$).

3.7 Neutrino-induced upgoing muons in MACRO

The simulation of upthroughgoing muons can be in principle obtained in two different ways. The upgoing muon flux has been parametrized as a function of the neutrino energy flux. Such method is quite fast, although the trace back of the muons is not possible: for instance, the energy and the distance traveled by the parent neutrino corresponding to a muon is not directly available. On the other hand, the full simulation starting with the neutrino interaction in the material below the detector, followed by the tracking of the muon, is extremely CPU consuming: it results in a small MC statistics collected, because the bulk of the muons generated in the neutrino interactions in the materials below the detectors does not reach the detector. Nevertheless the interaction region has to be large enough, to avoid systematic biases. To compare the real data with the MC predictions (see Chap. 6), we used a full simulation technique, spanning from $E_\nu = 1$ GeV to $E_\nu = 5$ TeV, which allowed us to collect a large statistics and to use a reasonable CPU time.

3.7.1 The simulation method

Our full Monte Carlo simulation uses the neutrino flux computed by the Bartol group [35]; the neutrino interactions includes the quasi elastic and the resonant interactions and the deep inelastic scattering, where the structure functions of ref. [37] have been used. The FLUKA [44] code is used to track muons from the interaction point to the underground hall floor. The simplest method to perform such simulation is to spread out the generated neutrino interactions over a semisphere. To avoid biases, the corresponding radius has to be larger than the range of the highest energy muon produced in the whole data sample. The number of events produced can be expressed as

$$N_{ev} = \frac{2}{3}\pi R^3 \rho \frac{N_{Av}}{A} \int_{Emin}^{Emax} \phi(E)\sigma(E)dE \qquad (3.3)$$

where R is the maximum range of the highest energy muon, N_{Av} is the Avogadro's number, $\phi(E)$ is the neutrino flux and $\sigma(E)$ is the neutrino cross section.

Although such method is correct, it requires a very large CPU time, since the bulk of atmospheric neutrinos, having low energies, spread out over the semisphere and produce muons never reaching the underground detector. To solve this problem, we divided the neutrino flux $\phi(E)$ in 5 energy intervals. For each energy interval, the range R is chosen so that only 1% of the muons with the highest interval energy would survive from a distance greater than R.

The method quoted above can be used if the geometrical dimensions of the detector are smaller compared with the size of the neutrino interaction region. As an example, in the first interval the radius of the semisphere is $R_1 = 20.3$ m. Since the most part of the neutrino detectors have an horizontal surface larger that R_1, the usual sampling method cannot be used, because it would introduce a bias on the simulation. To solve such problem, the semisphere has to be spread out over a given area below the surface of the detector. The dimension of such area depends on the angular limit to which we want to restrict our analysis. For just vertical tracks, the semisphere has to be spread out just over the horizontal area of the detector, for nearly horizontal muons a very large area is needed.

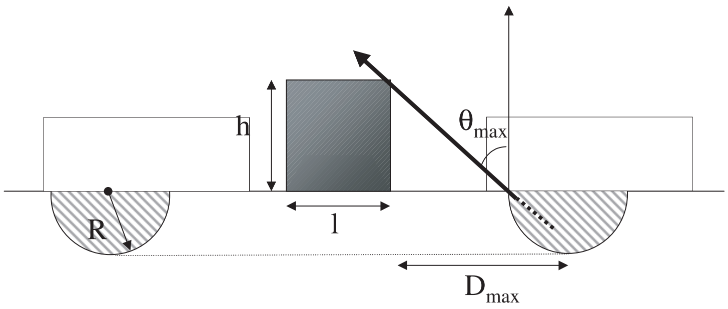

Figure 3.7: Sketch used for the simulation of ν_μ-induced upgoing muons.

Let us consider, as an example, a detector with dimensions $l \times p \times h$. Once the maximum angle Θ_{max} for upgoing muons is fixed, the maximum distance of the center of the semisphere at which a muon produced inside can still hit

E_ν(GeV)	$1 \div 4000$	$1000 \div 2000$	$2000 \div 3000$	$3000 \div 4000$	$4000 \div 5000$
N_μ	84178	2143	774	389	225

Table 3.1: Number of generated upgoing muons for the neutrino energy intervals listed in the first line. The data refer to a livetime of 60 years and $\Theta \leq 60°$.

the detector is given by (see Fig. 3.7)

$$D_{max} = h \cdot \tan(\pi/2 - \Theta) \tag{3.4}$$

The total volume in which the semisphere has to be moved is given by:

$$V = (l + 2D_{max}) \cdot (p + 2D_{max}) \cdot R + 2\pi R^2/4 \cdot [f + (l + 2D_{max})] + \pi R^2/2 \tag{3.5}$$

To compute the correct number of events to be simulated in a given energy region, the quantity in Eq. (3.3) has to be substituted with the effective volume in which the semisphere can be spread out. In our case, we limited the simulation to $\Theta \leq 60°$.

3.7.2 Simulation results

Most of our Monte Carlo simulation stops at neutrino energies $E_\nu = 1$ TeV, due to the low flux at such energies. Going beyond such limit is CPU time consuming, since neutrinos have to be spread out over a very large semisphere; for instance, a 5 TeV muon has just a 1% survival probability for a distance $L = 2.65$ km. We included in our simulation an energy interval from 1 TeV to 5 TeV. As a result, we obtained that the fraction of upgoing muons coming from neutrinos with energy $E_\nu \geq 1$ TeV is at least 5%. Table 3.1 shows the number of upgoing muons N_μ coming from the different energy windows between 1 TeV and 5 TeV and the total N_μ for energy between 1 and 4000 GeV.

Fig. 3.8 shows the energy spectra (*i*) of muon neutrinos giving a surviving muon at the underground hall level (continuous line), (*ii*) of the muons in the neutrino interaction point (dotted line) and (*iii*) of the muons after traveling through the rock (dotted line with full squares).

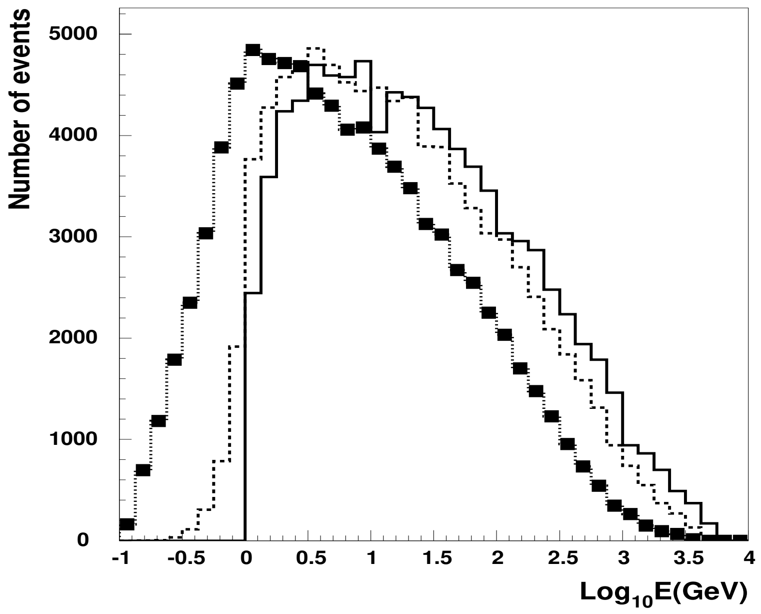

Figure 3.8: Energy spectra of muon neutrinos giving a surviving muon at the underground hall level (continuous line), of the muons at the neutrino interaction point (dotted line) and of the muons after traveling through the rock (dotted line with full squares).

Fig. 3.9 shows the ratio between the energy of muons in their production point $E_{\mu_{prod}}$ and the neutrino energy E_ν (empty squares) and the ratio between the energy of muons at the detector level $E_{\mu_{surv}}$ and the neutrino energy E_ν (full squares) as a function of the neutrino energy. The average neutrino energy fraction carried out by the muon when it is produced is about 75%. The small growth for $E_\nu \leq 5$ GeV comes from the quasi-elastic scattering, in which a larger fraction of energy is carried out by the lepton with respect to the DIS interaction.

On average, 37% of the neutrino energy is preserved by the upgoing muon, when, after rock propagation, it is detected by an underground experiment. The flatness of the distribution with respect to the neutrino energy is an important feature of upgoing muons: although smeared by the rock propagation, the upgoing muon energy shows a linear dependence from the neutrino energy.

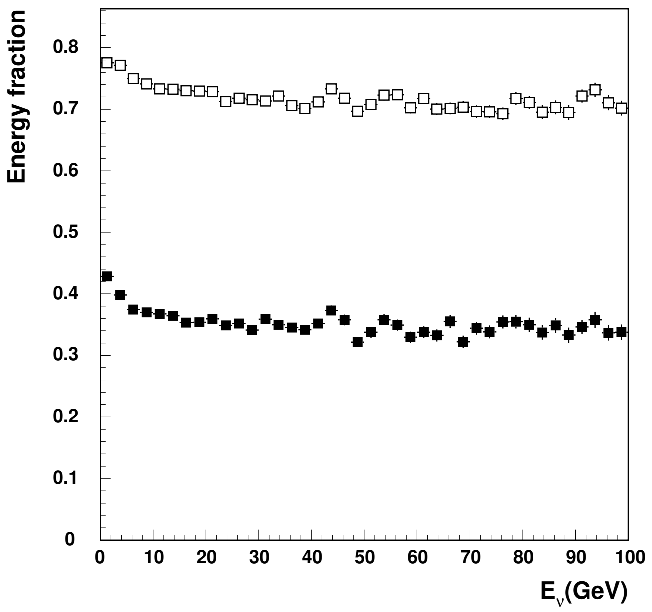

Figure 3.9: Ratio between the energy of muons at their production point $E_{\mu_{prod}}$ and the neutrino energy E_ν (empty squares) and ratio between the energy of the muons at the detector level $E_{\mu_{surv}}$ and the neutrino energy E_ν (full squares) as a function of the neutrino energy.

Fig. 3.10 shows the ratio of the L/E distribution computed considering the oscillation hypothesis and the L/E distribution computed neglecting it for neutrinos (continuous line), muons at the production point (dashed line) and at the detector level (dotted line). It is evident an oscillation modulation in neutrino curve and the first two peaks are still present in the muon data referring to the neutrino interaction point. On the contrary, the propagation through the rock produces a smearing in the L/E reconstruction and the "dip" disappears.

3.8 Uncertainty in the neutrino flux

Uncertainties in the calculated neutrino intensity arise from lack of precise knowledge of the input quantities, which are the primary spectrum and the

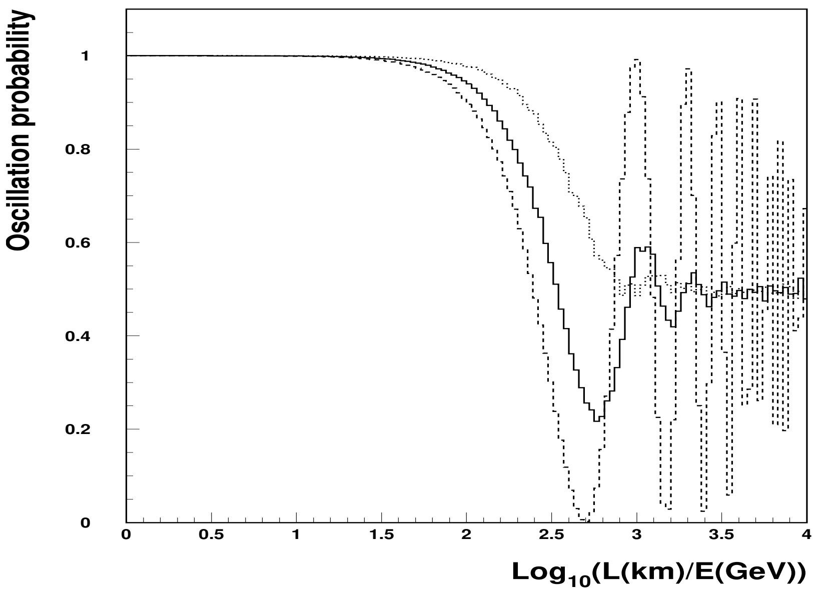

Figure 3.10: Ratio of the L/E distribution computed considering the oscillation hypothesis and the L/E distribution computed neglecting it, for neutrinos (dashed line), muons at the production point (continuous line) and at the detector level (dotted line).

inclusive cross section for production of pions and kaons by hadronic interactions in the atmosphere. As the relative contributions of kaons and pions to the neutrino flux depends both on the energy and on the angle, it is not possible to assign a single estimate of the uncertainty in the calculation.

A harder primary spectrum results in a smaller vertical/horizontal (V/H) ratio, because a harder primary spectrum results in a harder spectrum for the secondary mesons, and the decay enhancement becomes more important at high energy, when the decay probability is suppressed because of the Lorentz expansion of the particle laboratory decay time. Approximating the primary spectrum with a power law ($\phi_0 \propto E_0^{-\alpha}$), the uncertainty in the slope is translated in a systematic uncertainty on the V/H ratio. The uncertainty on the primary spectrum is estimated to be $\pm 15\%$ [61].

The K/π ratio is the dominant source of uncertainty on V/H. The $\pm 12\%$ uncertainty in the $\pi^{\pm}$ flux and the independent $\pm 17\%$ uncertainty in the $K^{\pm}$ flux give contribution respectively of $\pm 6\%$ and $\pm 8.5\%$ to the V/H ratio. Combining these uncertainties with the $\pm 15\%$ one in the primary spectrum, a $\pm 17\%$ uncertainty has been estimated [35].

The level of systematic uncertainties allows to use the upgoing muon measurement to put limits on oscillations with sterile neutrinos and on alternative models.

3.9 The neutrino survival probability

As already said, the upgoing muon measurements allow to obtain information about the survival probability $P(\nu_\mu \to \nu_\mu)$ and to exclude alternative mechanisms characterized by transition probabilities with different energy dependences. The transition probability has the form $P = F(L\ E_\nu^{-1})$ for standard oscillations, $P = F(E_\nu^0)$ for models with flavour changing neutral currents and $P = F(L\ E_\nu)$ for models violating the equivalence principle. To discriminate between these models, it is useful to study a broad range of E_ν.

The study of the survival probability $P(\nu_\mu \to \nu_\mu)$ to determine the dependence on the neutrino energy and path indicates the following qualitative features:

1. When E_ν is in the range of the contained events (less than few GeV), the probability is ~ 1 for downgoing neutrino directions and ~ 0.5 for upgoing ones. Near the horizontal, the probability has intermediate values.

2. For $E_\nu \gtrsim 100$ GeV, the informations on the probability P can be obtained from upgoing muons (averaging over a broad range of energy). The probability depends on the zenith angle from a minimum value of ~ 0.7

near the vertical, to a value of ~ 1 near the horizontal.

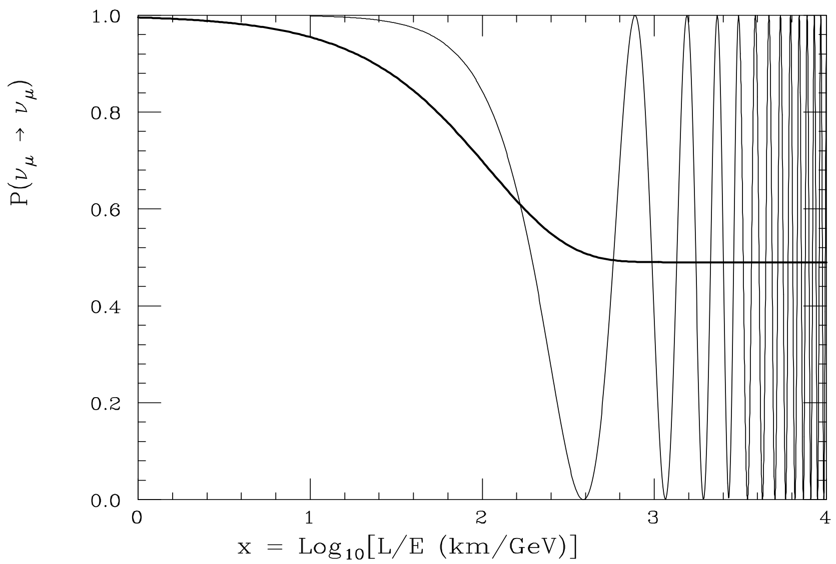

Figure 3.11: Best fit survival probabilities for ν_μ as a function of $\log_{10}(L/E_\nu)$. The thin line refers to standard oscillations, Eq. (3.6); the thick line, referring to the "decay model", is shown for comparison.

These features can be immediately understood, taking into account the finite resolution in the determination of the ν energy and direction if we assume that the probability has the form (thin line in Fig. 3.11)

$$P(\nu_\mu \to \nu_\mu) = 1 - \sin^2 2\theta \ \sin^2\left(\frac{\Delta m^2 \ L}{4E_\nu}\right) \tag{3.6}$$

The present experimental situation can not give informations about "oscillations" in the sense of a survival probability with minima and maxima. The resolution of the current experiments is not enough to study the oscillation pattern. This is the source of alternative models for the disappearance, like the "decoherence model" [62] and the "decay model" [63], where the survival probability goes smoothly from unity to a minimum value $\sin^4\theta$ with increasing L/E_ν (thick line in Fig. 3.11).

3.10 Conclusions

In this chapter, a description of the Monte Carlo simulations used for the atmospheric neutrino fluxes has been given. The elements entering in the ν flux predictions are the primary c.r. composition, the geomagnetic effects on the primary particles and on the showers, the models for the hadronic interactions and for the shower development and the production of $K^{\pm}$ and $\pi^{\pm}$ mesons.

The HKKM and Bartol models are based on a 1-D approximation, that is all secondary particles (hadrons, charged leptons and neutrinos) are assumed to be collinear with the parent primary cosmic ray. The implementation of a 3-D calculation, taking into account the angle between the primary cosmic rays and the produced neutrinos, showed an enhancement of the ν, $\overline{\nu}$ flux in the horizontal direction. This effect is particularly important in the Sub-GeV region, while for $E_\nu \geq 1$ GeV, the collinear approximation does not introduce important consequences.

The full simulation made to compare the MACRO data concerning upgoing ν_μ-induced muons used the Bartol neutrino flux and the FLUKA code for the rock propagation of muons from the production point to the detector level. The method to divide the neutrino flux in 5 energy intervals, from 1 GeV to 5 TeV, allowed to obtain a large statistics in a reasonable CPU time for 60 years of livetime.

Chapter 4

The MACRO experiment

4.1 Introduction

MACRO (Monopole, Astrophysics and Cosmic Ray Observatory) is a large area underground experiment located in the hall B of the Gran Sasso National Laboratory, Fig. 4.1. The average overburden of calcareous rock is $h \sim 3700$ hg cm^{-2}; the minimum overburden is $h \sim 3100$ hg cm^{-2} corresponding to a muon threshold energy $E_\mu^{th} \sim 1.4$ TeV. At the average depth of the Laboratory, the muon flux is reduced of a factor $\sim 10^6$.

The main goals of the experiment are the detailed study of the penetrating cosmic radiation, the search for rare particles [64] (supermassive magnetic monopoles predicted by Grand Unification Theories of the electroweak and strong interactions [65], nuclearites [66], WIMPs [67], LIPs [68]), the study of atmospheric neutrinos [69, 70] and the search for neutrinos from gravitational stellar collapses. Two primary characteristics of the detector are modularity and redundancy. Modularity allowed completed sections of the detector to operate while other sections were being completed (the completed detector has been in operation since August 1995) or undergoing tests or shut off for maintenance. Redundancy is offered by the three types of "sub-detectors" used: liquid scintillation counters, limited streamer tubes and nuclear track detectors.

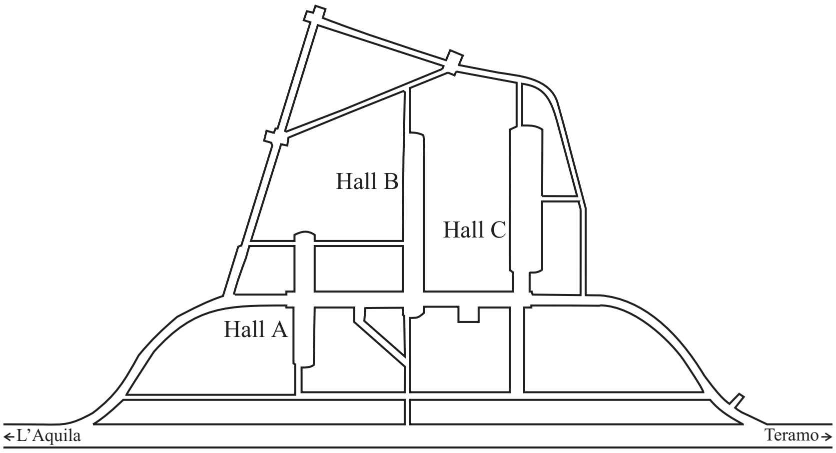

Figure 4.1: Map of the tunnel of the Gran Sasso Laboratory. The MACRO detector is located in the Hall B.

The large acceptance (~ 10000 m^2 sr for an isotropic flux of particles) and the relatively long period of data taking (MACRO started data taking in 1989 with 1 lower supermodule and was turned off at the end of year 2000) were important to collect data, especially in the framework of rare processes.

4.2 The MACRO detector

The MACRO detector [71] is composed by six 12m×12m×9.3m *supermodules*, Fig. 4.2. Each supermodule consists of a 4.8 m lower part (the "Base") and a 4.2 m upper part (the "Attico"). The global dimensions of MACRO are 77m×12m×9.3m.

Each lower supermodule consists of a horizontal sandwich of two layers of liquid scintillation counters, ten layers of limited streamer tubes separated by absorbers, one layer of passive nuclear track detectors located in the middle, Fig. 2.13. The upper part has on the top one horizontal layer of scintillators and four horizontal layers of limited streamer tubes. The vertical sides and the two extreme lower ends of the detector (north and south end-caps) are covered with one layer of scintillators and six layers of limited streamer tubes.

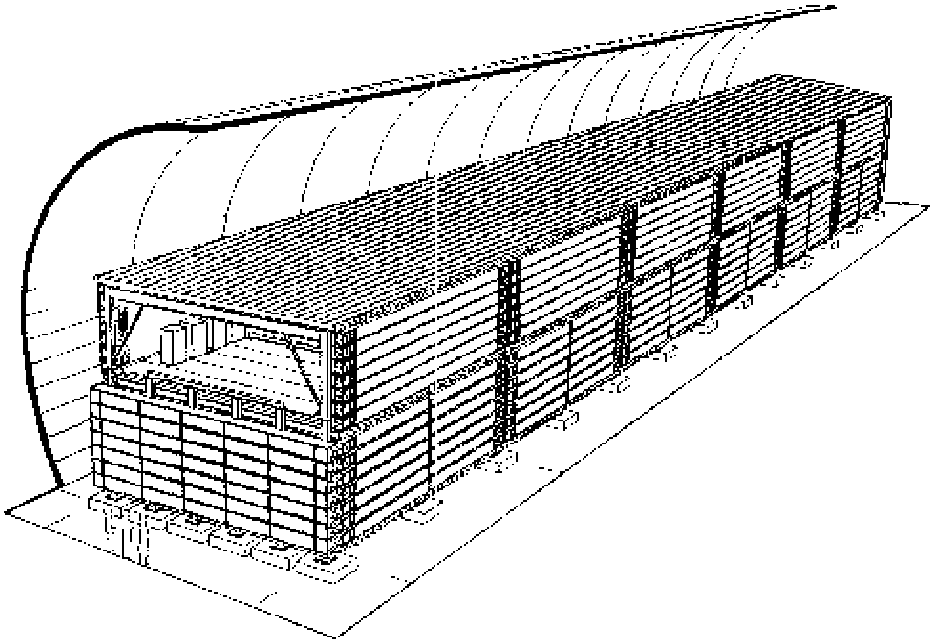

Figure 4.2: Global view of the MACRO detector.

The east side vertical wall (both lower and upper) and the north lower part are covered with nuclear track detectors. The attico has a "roof" which covers the whole apparatus and an empty space where the electronics is placed.

4.2.1 The streamer tube system

The main purpose of the limited streamer tube system is the tracking of crossing particles like muons. The elemental unit of the streamer tube system is a 25cm×3.2cm×12m chamber composed of eight *cells* of dimension 3cm×3cm×12m, Fig. 4.4. The whole chamber is enveloped in a PVC container. Three of the four internal sides of each cell are coated with low resistivity graphite which acts as cathode, while the anode is a silvered Be-Cu wire 12 m long and with a diameter of 100 μm, disposed in the center of the cell. The tubes operate in limited streamer regime and have a gas mixture of 73%

He and 27% n-pentane; this mixture provides a good detection efficiency for slow monopoles via the Drell-Penning effect [72].

In each of the 14 horizontal planes are placed 24 chambers, in the vertical walls are placed 14 chambers, for a total number of 6192 chambers in the whole detector (corresponding to 49536 wires). The total gas volume in the active streamer tubes elements of MACRO is about 465 m^3; a continuous recirculation system ensures the "good quality" of the gas. When a charged particle crosses a cell, the electrons stripped from the gas molecules migrate towards the wire. The particular choice of the wire diameter and of the gas mixture allows a single electron to produce an avalanche. This is due to the high electric field near the anode, since the electric potential goes as $\log(r)$ ($r =$ distance from the wire). The freed electrons and secondary photons produce the avalanche of secondary electrons which proceeds as a column towards the anode wire producing the streamer. The ultraviolet photons are absorbed by the gas and limit the streamer formation near the anode. The HV working point for a specific chamber can be determined by counting the single rates using a β source. The working point is usually set at $\sim$ 4200 V. The drift time of the streamer inside a cell has a distribution with a maximum value of $\sim$ 600 ns and an average value of $\sim$ 150 ns, which is the time resolution.

In the lower part, the limited streamer tubes are distributed in ten horizontal planes separated by seven $\sim$ 60 g cm^{-2} of $CaCO_3$ absorber; vertically there are six planes along each wall. In the attico, four planes are disposed in the horizontal part (the roof) and six planes in the vertical walls, Fig. 2.13.

For each horizontal plane of the lower part a tridimensional readout is performed using signals from the anode wires (x-view) and 3 cm aluminium 26.5° stereo pickup strips (D-view). In the attico also the vertical walls are provided with strips, at 90° with respect to the wire view. The average efficiencies of the streamer tube wire and strip systems are 95% and 88%, respectively.

The average width of a cluster, defined as a group of contiguous muon "hits", is 4.5 cm and 8.9 cm for the wire and strip views, respectively. The

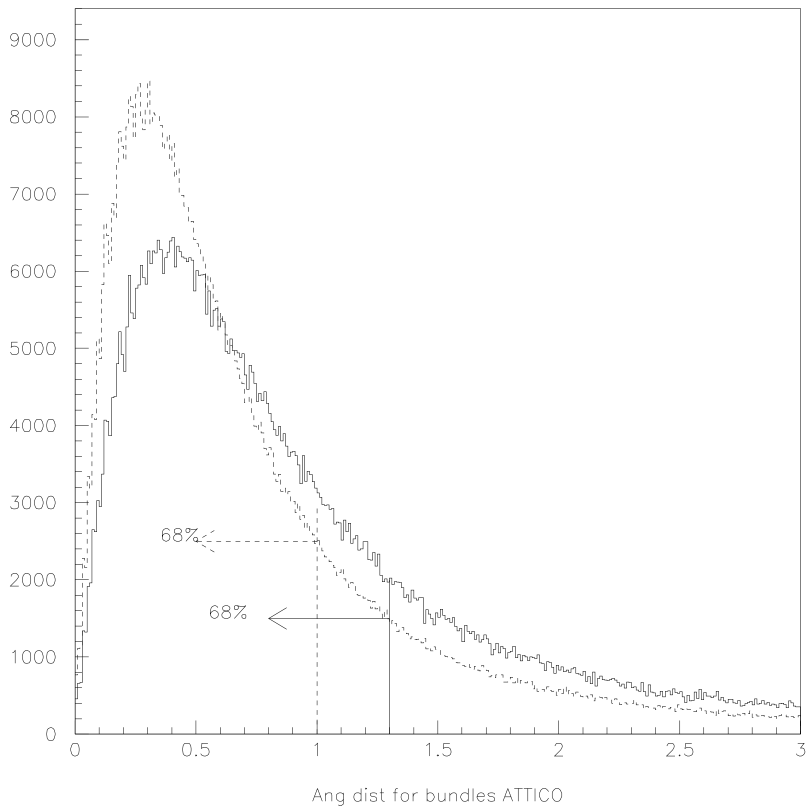

Figure 4.3: Distribution of the angular separation of dimuons for events with (dotted line) and without the attico (solid line).

muon track recognition is performed requiring at least 4 aligned clusters, through which a straight line is fitted. The distribution of the distances between the cluster centers and the fitting line (residuals) for muons crossing ten horizontal planes determines spatial resolutions of $\sigma_x = 1.1$ cm for the wire view and $\sigma_D = 1.2$ cm for the strip view. These resolutions would correspond to an angular accuracy of $0.2°$ over the 9.3 m height of the detector; this value must be compared with the angular resolution due to the multiple Coulomb scattering in the rock. The correct value can be extracted from the dimuon angular separation distribution. Fig. 4.3 shows the angular separation between muon pairs. The 1σ integral of the distribution is at $1.3°$ and $1.0°$ for the cases without and with the attico, respectively; they correspond to an intrinsic angular resolution of $1.3/\sqrt{2} = 0.92°$ and $0.70°$, respectively [73].

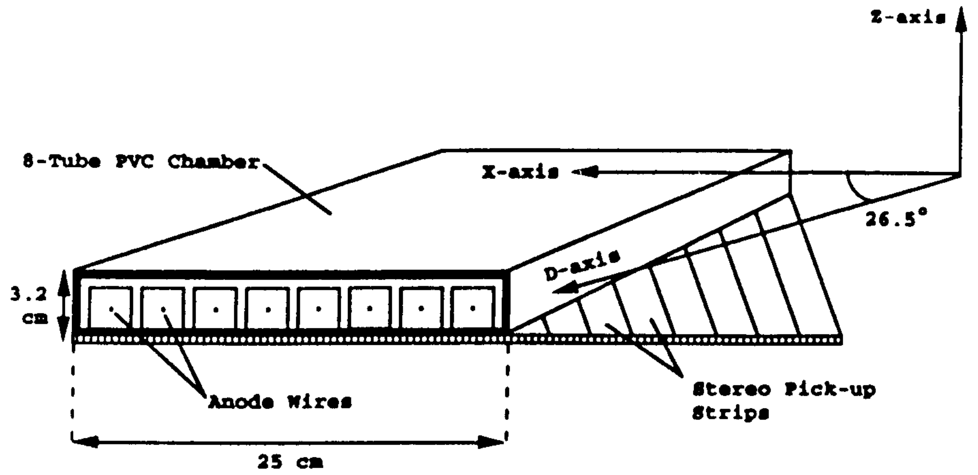

Figure 4.4: Structure of one eight-cell chamber of limited streamer tubes.

The readout of each chamber is provided by an eight channel card, directly connected to the HV with a 16 pin connector. The analogic signal is amplified, discriminated and sent to an ADC/TDC system (QTP modules) and to the trigger electronics. The output is a TTL signal with pulse width 10 μs for fast particles and 550 μs for slow particles; it is sent to shift registers (FAST and SLOW chain, respectively) and then to the Streamer Tube Acquisition System (STAS) by electronic modules called *splitter boards.* The wire readout card provides also the OR of TTL signals and additional digital OR (DigOR) from all the wires of each plane. Each strip readout card reads a group of 32 strips and contains an hybrid CMOS integrated circuit which amplifies and discriminates the signal. A 4.43 MHz clock determines the width of the output signal, which is shaped at 600 μs for the slow chain and 14 μs for the fast chain.

Streamer tube triggers

The streamer tube triggers can be classified on the basis of the particle velocity.

• *Fast particle triggers.* The triggering conditions are codified in three EPROM components: one for signals coming from horizontal planes, one for signals coming from vertical planes and one for mixed cases. The EPROM input is the OR of the discriminated signals coming from each horizontal or vertical plane of each supermodule. The triggering conditions are:
– 6/10 horizontal planes in coincidence;
– 5/10 contiguous horizontal planes in coincidence, excluding the first and the last plane;
– 3/10 horizontal and 3/6 vertical East in coincidence;
– 3/10 horizontal and 3/6 vertical West in coincidence;
– 3/6 vertical East and 3/6 vertical West in coincidence;
– 5/6 vertical East in coincidence;
– 5/6 vertical West in coincidence.

• *Slow particle triggers.* The goal of these triggers is to distinguish a slow monopole from random background signals occurring during the gate time of the slow chain. The streamer tube system is a low noise device, so the background is only due to local radioactivity ($\sim$ 40 Hz m^{-2}). The background signals are generated randomly in positions and times; thus they do not agree with those expected from the passage of a massive slow monopole. The triggering condition requires the spatial and time alignment of the hits.

The QTP system

The QTP (Charge and Time Processor) system [74] was designed to provide signals for triggering and to measure the charge, the arrival time and the width of the streamer pulse of the particle crossing the tubes. It is an ADC/TDC system; the ADCs are devoted to the measurement of the charge released by ionizing particles in the streamer tubes, while the TDCs measure the rise time and the duration of the streamer tube signals. In order to reduce the number of electronic channels, a single QTP channel serves the OR of 4 chambers, for a total of 32 wires.

A slow ($\beta \sim 10^{-4}$) monopole in MACRO would take ~ 200 μs to cross the apparatus on the vertical; as the crossing time increases with the zenith angle, the maximum time acceptance is set at 600 μs to include the complete angular coverage. The QTP system is optimized to distinguish in such time window the randomly distributed background from a slow particle, which, during the time required to cross the detector, describes a line in the space-time plane.

A QTP board, see Fig. 4.5, consists of three separate channels. Each channel is divided into an input stage, a section performing TDC functions and an ADC. The input signal is amplified ($\times 5$), discriminated and shaped. The rising and falling edges of each signal are measured by a 16 bit 6.6 MHz counter; it implies that the arrival time and the duration of the streamer signals are obtained with a time resolution of 150 ns. A linear integrator and an 8 bit FADC provide the signal charge in a range from 3 to 700 pC. The FADC reads the integrator output a clock cycle after the trailing edge of the signal. In this way, for each signal, the arrival time, the falling time and the charge are stored in a cyclic 32 bit memory which serves the three channels. For each hit, in this memory are written three words (two TDC words referring to the signal rise and fall and an ADC word referring to the signal charge), a 2 bit code to distinguish TDC words from ADC words and a 6 bit code to identify the channel corresponding to the signal rise or the signal fall. The QTP memory depth, 63$\times$32 bit words, can record up to 6 noise signals on each input channel.

The flow of the data from the QTP memory to the CAMAC processor is done by a transceiver board; it generates the 150 ns clock common to the QTP and to the CAMAC card in such a way to obtain the synchronization of the whole system. The CAMAC processor has three different memories: (*i*) a cache memory where TDC and ADC informations are first read, (*ii*) a memory where these informations are stored and ordered, (*iii*) a FIFO memory to permit the zero suppression for the host transfer. When a trigger occurs, a

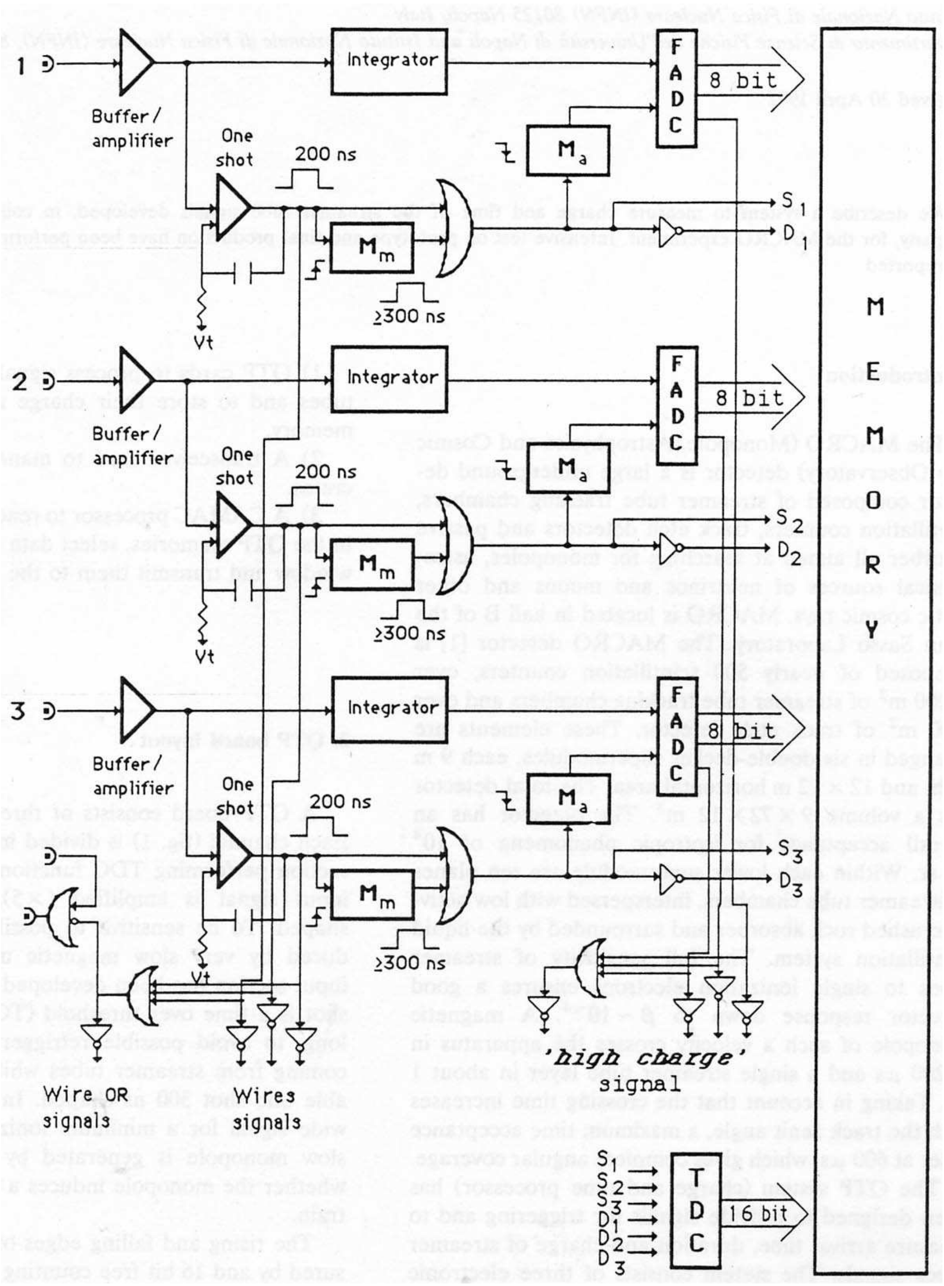

Figure 4.5: QTP system layout.

16 bit counter, synchronous with the TDC counters, gives the trigger time and a 600 μs window is opened. Only the events in this window are transferred to the cache memory. The differences between the trigger and the TDC times gives the absolute time of single hits. When the transfer is completed for all the QTP cards of a CRATE, a general reset and clear signal is sent to the TDC counters, to the QTP memories and to the trigger counter, to enable the acquisition. The time requested for this operation is $\simeq$ 300 ns/word. The CAMAC memory is logically divided in 60 channels, each corresponding to a single QTP channel. Data from QTP are ordered temporally and spatially for an easy acquisition and processing.

4.2.2 The scintillator system

The liquid scintillation counters are devoted to measurements of energy loss dE/dX, velocity, versus and time of flight of crossing particles and to detect bursts of low energy $\overline{\nu}_e$ from gravitational collapses.

The liquid scintillator is composed of high purity mineral oil (96.4%), pseudocumene (3.6%), 1.44 g l^{-1} PPO, 1.44 mg l^{-1} bis-MSB and antioxidants. The density of the mixture is 0.85 g cm^{-3} and the attenuation length is $\sim$ 12 m.

In each supermodule, 32 horizontal and 21 vertical counters are placed in the lower part of the detector, 16 horizontal and 14 vertical counters are placed in the attico. The active liquid scintillator length is 11.2 m for the horizontal counters and 11.1 m for the vertical ones. The whole apparatus consists of 476 scintillation counters for a total amount of $\sim$ 600 tons of liquid scintillator.

The horizontal counters consist of PVC 12m$\times$75cm$\times$25cm tanks, lined with FEP teflon and equipped at each end with two hemispherical photomultipliers (PMTs), Fig. 4.6a. The vertical counters, which close the sides and ends of the detector, have dimensions of 12m$\times$50cm$\times$24cm and are viewed by one PMT at each end, Fig. 4.6b.

The PMTs have $\sim$ 20 cm diameter photocathodes and 14 dynodes disposed in a venetian blind structure. The typical gain for a single photo-electron, $\sim 10^7$, corresponds to a pulse height of 3 mV. The used HV is about -1500 V: 550 V between the photocathode and the first dynode and the remaining 950 V uniformly distributed between the other dynodes.

Each scintillator box is divided into three chambers separated by transparent PVC windows: the longer chamber is the central one ($\sim$ 11 m) which is filled with the liquid scintillator; the other ones, placed at the two box ends, contain the PMTs and are filled with the same mineral oil of the middle chamber to ensure a good optical coupling (the optical transmission is $> 90\%$ for wavelength > 400 nm). This geometry allows the rejection of spurious signals near the PMT coming from natural radioactivity. The inner walls of the middle chamber are lined with a vinyl-FEP material, with a refractive index $n' = 1.33$. The difference with the refractive index of the liquid scintillator $n = 1.47$ gives, through the formula $\theta_c = \arccos(n'/n)$, a critical incidence angle for total reflection $\theta_c = 25.6°$. Total reflection is also provided by the air/scintillator interface in the middle chamber. In this case the critical angle for total reflection is $\theta_c = 47.3°$.

The readout electronics can reconstruct the energy loss in a counter from a threshold value of $\sim$ 7 MeV, independently of the interaction point and with an energy resolution $\sigma_E/E \simeq 0.3/\sqrt{E}$, with E in MeV. The scintillator/PMT coupling readout system consists of TDCs and ADCs on the PMT anode and the last dynode. Slow (20 MHz), fast (50 MHz) and very fast (200 MHz) waveform digitizers record the light yield and thus the energy loss and velocity of slow and fast particles crossing the counters.

The monitoring of the scintillators is performed with LEDs mounted in the end chambers near the PMTs and UV light from N laser coupled to the scintillator liquid with optical fibres. Global calibrations are performed weekly, tests are made every four hours to verify on line the performance of the data taking.

The difference of arrival time at each counter allows to estimate the po-

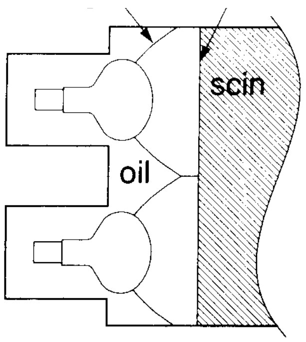

(a)

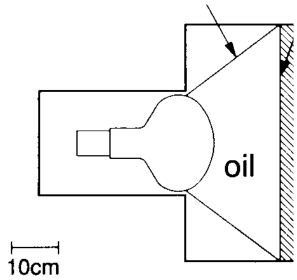

(b)

Figure 4.6: Details of each end of the horizontal (a) and vertical (b) scintillation counters.

sition of the crossing particle in the scintillator. The difference between this value and the one obtained from the streamer tubes is used to estimate the spatial resolution of the scintillator system. The standard deviation of the distribution of the difference is $\simeq 11$ cm, corresponding to a time resolution for the single counter of $\simeq 520$ ps. Therefore, the time resolution on the time of flight measurement is $\sigma_{TOF} \simeq 520 \cdot \sqrt{2} \simeq 750$ ps. This value is used to discriminate the arrival direction of relativistic particles and to recognize upwardgoing neutrino-induced muons.

Scintillator triggers

The signals from the PMTs are sent to the trigger electronics, to the ADCs, TDCs and to the Wave Form Digitizers (WFD) circuits. All the scintillator triggers, except ERP-GC and PHRASE, send early stops to the 200 MHz WFD to read the registered data. The scintillator system is provided of some complementary triggers, ensuring the detection of different physics events.

• CSPAM (Chuck Steve P. Ahlen Muon): considers each lateral wall as a unique "supercounter" and takes in input the two signals generated by the sum of each PMT in the two "supercounter" ends. If the two signals are in a 100 ns window with a minimum amplitude of 200 μV, a pretrigger signal is generated. Then, if two opposite walls generate a pretrigger in a 1 μs window, a trigger signal is generated.

• ERP (Energy Reconstruction Processor): reconstructs the energy loss by muons in the scintillator tanks and provides the crossing time. The signals at the two PMTs are compared with the ones contained in RAM look-up tables (LUT). For each pair of signals, the corresponding energy is computed and if it exceeds a threshold value of 10 MeV, the trigger is generated.

• FMT (Fast Monopole Trigger): operates in anticoincidence with CSPAM, using the same electronics and requires a time window of 10 μs.

• PHRASE (Pulse Height Recorder And Synchronous Encoder): searches for low energy ($\sim$ 10 MeV) $\overline{\nu}_e$ from gravitational stellar collapses, through the CC reaction $\overline{\nu}_e + p \to n + e^+$ with the protons of the scintillator.

• TOHM (Time Over Half Maximum): is a slow monopole trigger. The analog signals from PMT anodes are converted into TTL signals, whose duration is the time that the input pulse is larger than its half height. This trigger is studied to suppress large and sharp pulses produced by muons and natural radioactivity. A circuit integrates the TOHM output, giving a wide signal if the input is a wide pulse or a dense burst of single photoelectrons in the case of slow monopoles.

• LaMoSsKa : provides an early stop of the WFDs for high energy events. The signals from the CSPAM "supercounters" are discriminated and 110 μs delayed before to sent the stop to WFDs.

• St-Sc trigger: uses the informations from the streamer tube and the scintillator systems. In presence of a slow monopole trigger, the WFDs of the corresponding modules are read.

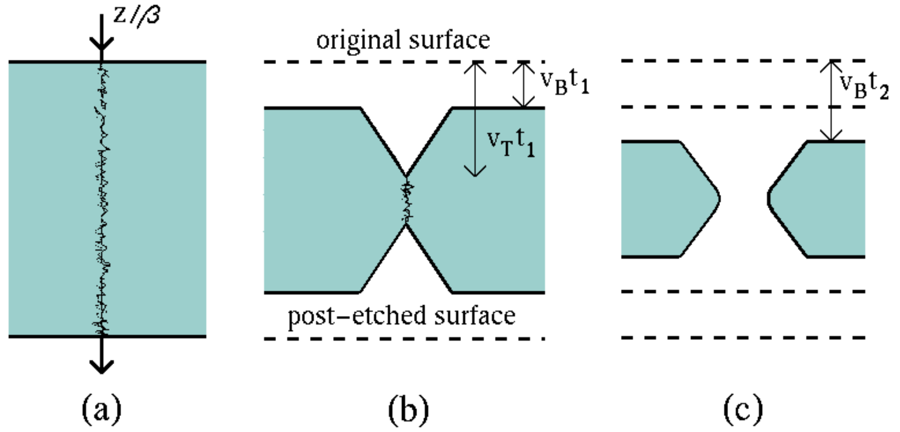

Figure 4.7: (a) In a polymeric nuclear track detector, a heavily ionizing particle breaks the polymeric bonds along its path, leaving reactive molecules; (b) a chemical etching in a basic water solution acts globally with velocity v_B and preferentially along the path of the particle with velocity v_T, forming, after the time t_1, observable cones on the post-etched surfaces and, after t_2, a hole (c).

4.2.3 The nuclear track detector

The main purpose of the nuclear track detector is to offer independent measurements for the search for magnetic monopoles. The MACRO track-etch system consists of two types of nuclear track detectors, CR39 and Lexan. Lexan has a higher detection threshold ($Z/\beta \sim 55e$) compared to the CR39 one ($Z/\beta \sim 5e$), making it sensitive to relativistic monopoles only. Until now Lexan has not been used for monopole searches and most of the work concerns the development and processing of CR39.

When a heavily ionizing particle crosses a nuclear track detector foil, it produces damages at the level of molecular bonds, forming the so called "latent track". During the chemical etching of the detector in a basic water solution, as the etching velocity along the "latent track", v_T, is larger than that in the bulk material, v_B, etch-pit cones of equal size are formed on both sides of the foil, Fig. 4.7. The base area and the height of each cone are functions of the Restricted Energy Loss (REL) of the incident ion and thus of the charge Z

[75, 76].

The MACRO track-etch detector is organized in stacks ("wagons") consisting of three CR39 layers each about 1.4 mm thick, three Lexan layers each 0.25 mm thick, and an aluminium absorber 1 mm thick, Fig. 4.8. Each stack has a surface of 24.5×24.5 cm^2 and is placed in an aluminized mylar bag filled with dry air. The detector is placed on the vertical walls on the east and north sites and horizontally in the middle of the lower apparatus, for a total area of 1263 m^2.

After extraction from the MACRO apparatus, three fiducial holes are drilled in each wagon by a precision drilling machine. The next steps are: (i) a "strong" etching in 8N NaOH water solution at 85 °C for 50 hours is applied to the first upper sheet of each wagon; (ii) after etching, we perform a first scan in transparency and a successive analysis with a binocular microscope with low magnification (16×), looking for holes and/or corresponding double etch-pits; (iii) in case of a candidate in the upper sheet, a "standard" etching in 6N NaOH water solution at 70 °C for 30 hours is applied to the third sheet. A good candidate track must satisfy a three-fold coincidence of the position, incident angles among the layers and should also give the same value of REL.

The detection of MMs is limited to poles with incidence angles smaller than a critical value δ_c with respect the normal; one has $\delta_c = \arccos\ (p^{-1})$, where $p = v_T/v_B$ [75].

The acceptance of the MACRO CR39 was determined with a Monte Carlo simulation assuming an isotropic flux of monopoles. This requires that the monopole masses should be greater than 10^{17} GeV and their velocities should be larger than $\beta = 3\cdot10^{-5}$ for $g = g_D$ monopoles and $5\cdot10^{-5}$ for $g = 2g_D,\ 3g_D$ (g_D is the Dirac charge [77]) monopoles and monopole-proton aggregates. The total acceptance of the MACRO CR39 subdetector is 7100 m^2 sr for an isotropic flux of fast monopoles.

The track-etch detector can be used as a "stand alone" detector [78] and in a "triggered" mode, where the triggers are scintillation counters and/or streamer tube monopole candidates. In this last case, when a candidate is triggered by the scintillation counters and/or by the streamer tubes, the corresponding wagon around the expected position is extracted and analyzed with the described procedure.

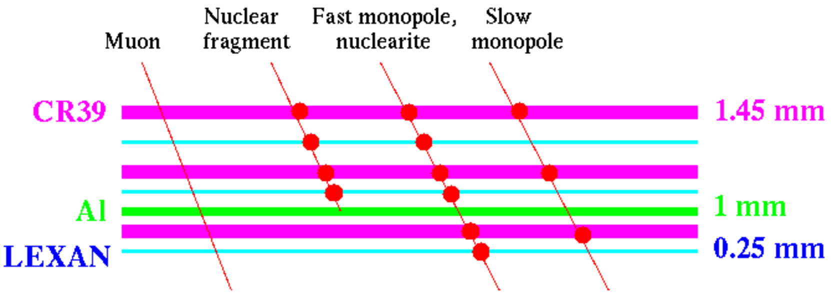

Figure 4.8: Stack of nuclear track detectors used in MACRO. The red points indicate the breaking of polymeric bonds forming the "latent track" for different particles.

4.3 The MACRO Data Acquisition System

The layout of the MACRO Data Acquisition System (DAS) is shown in Fig. 4.9. It is based on a network of KAV 30 Vax Processors and MicroVAX-II supported by a VME and CAMAC system crates. After a first period in which the MACRO DAS was based only an a network of MicroVAX-IIs, the system has been upgraded to include VME front-end electronics of the new Wave Form Digitizers [79] for the scintillation counters. The system runs under VAXELN, a dedicated operating system of VAX computers with an I/O speed of ~ 300 kb s^{-1}. The processors are located in VME crates, which act as "Master Crates" from which remote VME and CAMAC crates may be accessed.

Each of the three KAV 30 processors controls two supermodules, while the three MicroVAX-IIs control the PHRASE trigger. A central VAX 4000/500 running under VAX/VMS performs the data logging and is used as interface

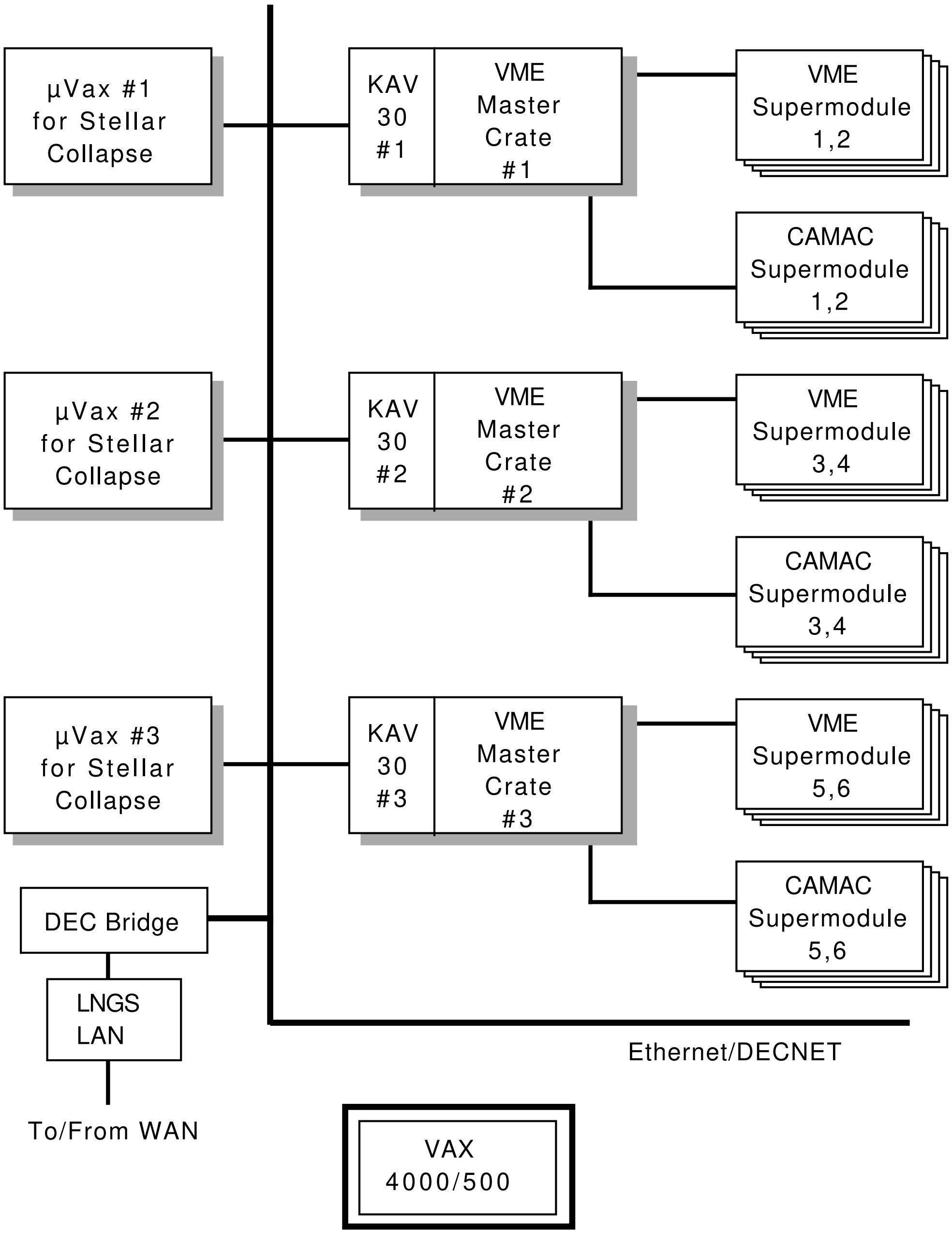

Figure 4.9: General layout of the MACRO Data Acquisition System.

from the user to the MACRO DAS. All the computers are connected with Ethernet/DECNET and a DEC bridge connects the MACRO LAN (Local Area Network) to the LNGS LAN of outside Laboratories. From outside, the user can connect to the MACRO LAN and copy raw data files or submit directives to execute CAMAC operations.

The timing is given by the LNGS atomic clock, synchronized with the UTC/USNO standard using the satellitar GPS system. Each second the GPS system transmits a signal containing satellite status and timing to a "Master Clock" located on the outside Laboratories. This generates the local time with a 10 MHz signal using a rubidium oscillator and drives a set of six "Slave Clocks" located underground near the apparatus which corrects the signal and reproduces the UTC/USNO time with a $\sim$ 100 ns accuracy.

4.4 The MACRO offline analysis

The MACRO offline program organization follows the choices specified for the online system. For this purpose a dedicated code is necessary to face all the offline needs from the first production of Standard Tapes (ST) up to more refined analysis on Data Summary Tapes (DST). These operations are accomplished by DREAM (Data Reduction and Event Analysis for MACRO) [80], a FORTRAN 77 code which performs the decoding and reconstruction of MACRO events. The code is structured in "passes". The pass 0 is a pre-analysis step which processes the raw data collected online and stores them on disks of the online computer. The result of this pre-analysis pass consists in the evaluation of the most relevant physical quantities of the events and in the output of data on ST in a machine independent format. The data are structured into banks at different stages of the program. The data elements are stored in vectors Q(link+I) and the links in LQ(link), where Q and LQ are the names of the fortran arrays managed by ZEBRA. Data structures can store banks of different types (bit, string, integer, floating point, double precision,...) according to the initial declaration.

Pass 1 corresponds to the event decoding, i.e. the program reads the equipments and decodes the informations (from codified words to digital informations). Pass 2 reconstructs the relevant physical parameters of each event (from digital informations to analogic informations). The last pass, 3, produces the complete event reconstruction, including the number of tracks and their coordinates in the absolute frame of the detector. The informations contained in the output of pass 3 are written in DST files. This operation preserves all the relevant parameters of the event performing a data reduction of a factor ~ 60.

DREAM uses software packages from the CERN Program Library, like ZEBRA [81] for I/O operations and data structure managing and HBOOK [82] for printing, histogramming, event display. The run control commands are input to DREAM with a DATA CARD list, where the user defines the values of the variables associated to the keywords defined in the program. These input variables are used inside the program to decide, according to their values, the operation to perform. The package used for these operations is FFREAD [83]; it allows input of variables in a format-free way, has the capability of reading input from files and of calling a user action routine.

4.5 The MACRO Monte Carlo simulation

The simulation of the response of the MACRO detector to any possible physical event detectable in the experiment is performed with the Monte Carlo program GMACRO [84], based on the GEANT3 package. The routines available in GEANT3 are called by the user, who assembles the main program and a number of subprograms. The input variables used inside the program are given with the FFREAD package; all data structures are stored in ZEBRA banks and written in a machine independent format.

Any set-up where the particles are transported is represented by a structure of geometrical volumes, each of which is filled with matter. The first and largest volume used in GMACRO is the full detector box filled with air. The Master Reference Frame used in the program has its origin in the geometri-

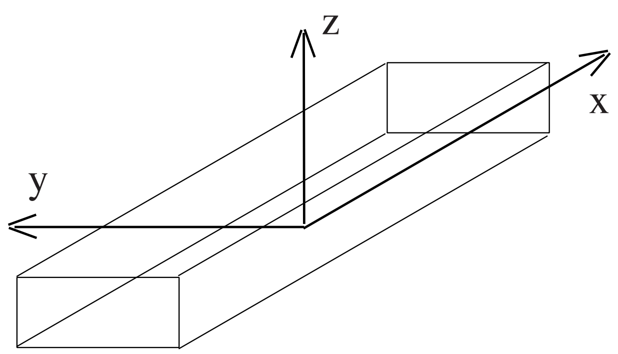

Figure 4.10: GMACRO Master Reference Frame: the x-axis runs along the major side of the detector, the z-axis points towards the ceiling of the Gran Sasso gallery.

cal center of this "mother" volume and the orientation of the axes shown in Fig. 4.10: the x-axis runs along the major side of the detector, the z-axis points towards the ceiling of the gallery. The "mother" volume contains supermodules and modules; every module is a stack of planes identified by a symbolic code; tube and scintillator planes are subdivided in smaller boxes called "elements", further subdivided into "cells". With this criterion, all the informations about planes, elements and cells are stored in arrays whose raws correspond to different types of volumes.

The matter composing the volumes is described by two sets of attributes, one relative to the nature of the material (atomic number, atomic mass, density,... etc.) and one referring to the process of particle transport (magnetic field, tracking precision, maximum energy lost in one step,... etc.). For each particle crossing a sensitive volume the x,y,z coordinates of input and output points, the mean momentum, the energy loss, the mean time of flight in the sensitive volume and the number of the track producing the hit are stored. The digitization consists in the simulation of STAS chains and in the evaluation of timing and charge released by the streamer tubes on the wires. A slow chain and a fast one are associated to different readout systems. The signals produced on strips and wires are stored in shift register chains, which are read by the STAS that encodes the position and the cluster of "fired" strips and wires.

All the data read or produced by GMACRO are stored in ZEBRA banks in a machine independent format. The output can be read either from GMACRO or using different programs performing analysis jobs. Some dummy routines, inserted in the tracking sequence, allow the user to control the job. In this way, it is possible to read the produced data and to store all the parameters in a non standard format.

Chapter 5

Multiple Coulomb Scattering analysis

5.1 Introduction

The deficit of events and the distortion of the zenith angle distribution for upthroughgoing muons in MACRO provided evidence for muon neutrino oscillations, confirmed by the lower energy data (§2.5.1). As already seen, the neutrino oscillation probability depends on the ratio L/E_ν, where L is the distance traveled by the neutrino between the production and the interaction points and E_ν is the neutrino energy (§2.3.1, Eq. (2.19)).

For high energy muons, L is measured by MACRO using the reconstructed zenith angle of the tracked muons. The energy of upgoing neutrinos, interacting in the rock below the apparatus, is shared by the upgoing muon and by the hadrons, the latter being definitively undetectable. Independently of the detector resolution, a precise measurement of the muon energy is prevented by the energy lost by the muon in the rock. Nevertheless, Monte Carlo simulations show that the muon energy at the detector level (residual muon energy) still preserves informations about the parent neutrino energy (see §3.7). Fig. 5.1 shows the predicted residual muon energy E_μ as a function of E_ν, for $E_\nu \leq 100$ GeV. Thus, the measurement of the ν_μ-induced muon energy adds an important piece of information to the study of the oscillation probability.

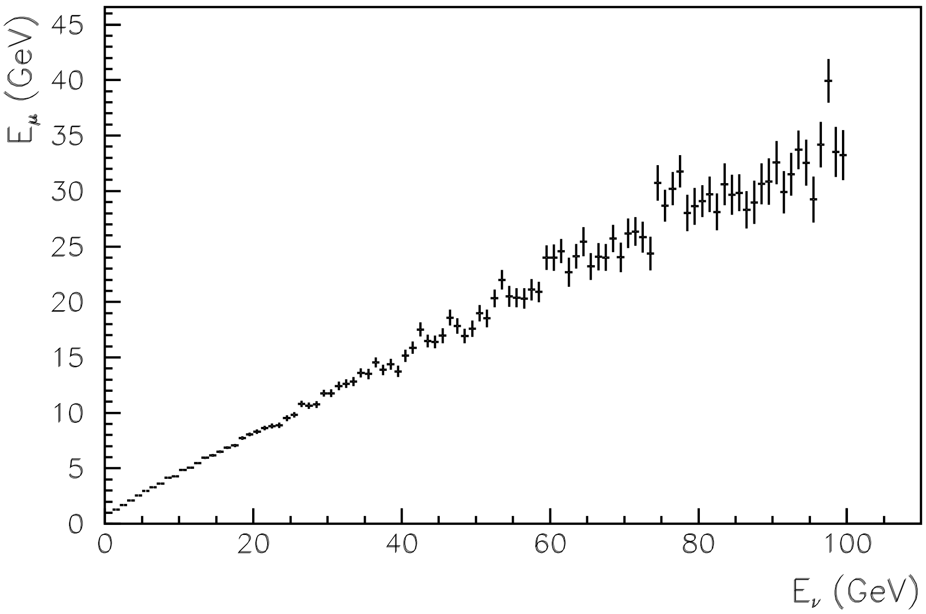

Figure 5.1: MC simulation: residual muon energy E_μ as a function of the parent neutrino energy E_ν.

Since MACRO is not equipped with a magnet and the mass is not large enough to stop most of the upgoing muons, the only way to estimate the muon energy is through their MCS in the MACRO absorbers.

The r.m.s. of the lateral displacement of a relativistic muon crossing a layer of material with depth X and radiation length X^0 is

$$\sigma_{MCS} \simeq \frac{X}{\sqrt{3}} \frac{13.6 \text{ MeV}}{p_\mu \beta c} \sqrt{\frac{X}{X^0}} (1 + 0.0038 \ln(X/X^0)) \tag{5.1}$$

where p_μ (GeV) is the muon momentum. For a given amount of crossed material, a correct measurement of the track deflection is possible only when σ_{MCS} is larger than the detector space resolution. In MACRO, $X \simeq 25X^0/\cos\Theta$, giving on the vertical $\sigma_{MCS} \simeq 10(\text{cm})/E_\mu(\text{GeV})$. The space resolution of the tracking system (streamer tubes used in digital mode) is ~ 1 cm, providing a muon energy estimate through MCS up to $\simeq 10$ GeV; this value is not enough to fully exploit the oscillation informations given by neutrino-induced upgoing muons.

In fact, in the case of neutrino oscillations with $\Delta m^2 \sim 10^{-3}$ eV^2 and $\sin^2 2\theta \simeq 1$, the neutrino-induced upgoing muons are not expected to experience neutrino oscillations at all energies. At the upgoing muon median energy in MACRO, 11 GeV, the oscillation probability is still 50%, while it is just 10% for $E_\mu \simeq 40$ GeV (Fig. 5.2). An improvement of the space resolution is then essential to have the possibility of evaluating the muon energy in a sufficiently wide energy range.

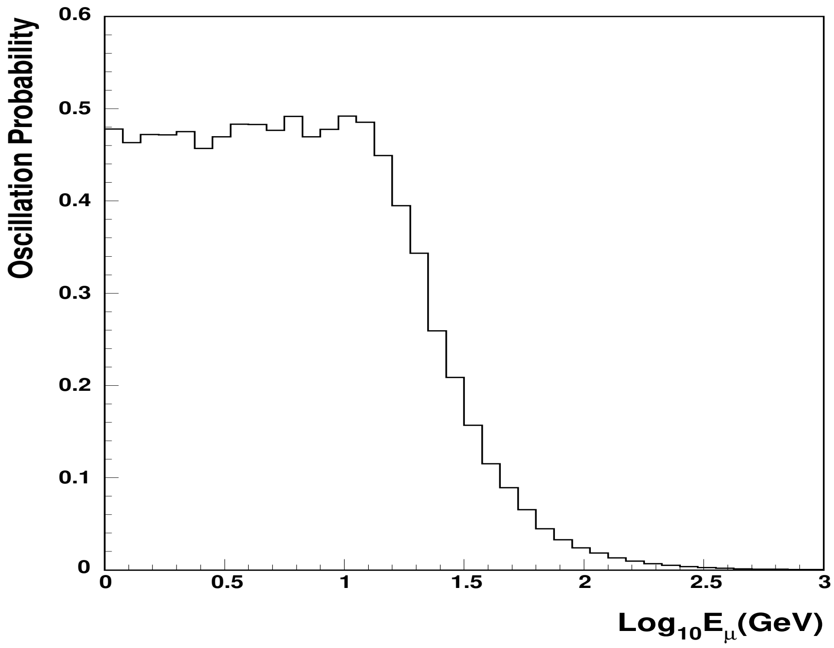

Figure 5.2: Oscillation probability as a function of the muon energy in MACRO for $\Delta m^2 = 2.5 \cdot 10^{-3}$ eV^2 and $\sin^2 2\theta = 1$.

The momentum resolution obtainable from MCS measurements is the result of two different contributions: the number of sampling planes N and the spatial resolution of the detector σ_{MCS}. In our case $N = 8$ (the number of streamer tube planes interleaved with scattering material), and $\sigma_{MCS} \simeq 1$ cm.

If we define a characteristic momentum scale ($\simeq 2.2$ GeV for MACRO):

$$p_{MCS} = \frac{0.015 \cdot \Delta\sqrt{\Delta/X_0}}{\sigma_{MCS}} \tag{5.2}$$

where Δ is the distance between two tracking planes and X_0 is the material radiation length, then the momentum resolution can be expressed as:

$$\frac{\sigma_p}{p} = \frac{1}{\sqrt{2N}}\left[1 + \text{const}\left(\frac{p}{p_{MCS}}\right)^2\right] \tag{5.3}$$

The σ_p/p limit for infinite spatial resolution is then $1/\sqrt{2N}$. If the intrinsic chamber resolution dominates (as in our case), the MCS-based momentum estimates behave as the square of the space resolution. Thus, an improvement of a factor k in the spatial resolution yields an improvement of a factor k^2 in the momentum resolution.

I shall explain in this chapter how the MACRO limited streamer tube system can be operated in drift mode by retrieving the time information from the TDCs implemented in the QTP (Charge and Time Processor) system, §4.2.1. In this way, a successful improvement of the space resolution can be obtained, allowing the analysis of muon tracks in terms of Multiple Coulomb Scattering (MCS) and to obtain an energy estimate of upgoing muons crossing the detector. I shall describe the application of this method to evaluate the MCS effect along a muon track, showing the results obtained in two dedicated tests, performed at CERN PS-T9 and SPS-X7 beams, to provide a full check of the electronics and to exploit the feasibility of the MCS analysis. By using a neural network approach, it is possible to estimate the muon energy for $E_\mu \lesssim 40$ GeV. The test beam data provided then an absolute energy calibration, which allowed to apply this method to the MACRO data.

5.2 The MACRO limited streamer tubes in drift mode

Streamer tubes in drift mode have been studied in ref. [85], showing that for tubes with a 0.9×0.9 cm^2 cross section, a space resolution $\sigma \simeq 150$ μm can be achieved. The MACRO streamer tubes, with a 3×3 cm^2 cross section, were built in "coverless" mode, so the electric field on the inner four walls is not exactly the same (§4.2.1), see Fig. 5.3.

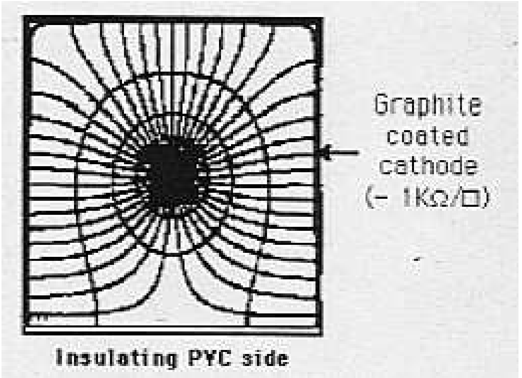

Figure 5.3: Electric field configuration in a MACRO limited streamer tube.

Such feature, anyway, does not spoil in a significant way the space resolution [86]. Using a MACRO-like streamer tube in drift mode, a resolution of $\sigma \simeq 250$ μm has been obtained using standard Lecroy 2228A TDC (250 ps/bin) [86]. Such value has to be considered the best resolution obtainable with our streamer tubes.

The clock frequency for the QTP-TDCs, 150 ns, is coarse for drift timing measurements, because the maximum drift time for the MACRO streamer tubes is $\simeq$ 600 ns. The ultimate space resolution achievable with such device is $\sigma \simeq v_{drift} \cdot \Delta T/\sqrt{12} \simeq 2$ mm.

The use of the MACRO streamer tubes in drift mode is illustrated in Fig. 5.4. Given a muon track reconstructed with the standard tracking, we select the hits made by a single fired tube. In this way, the association with the fired

QTP channel is uniquely determined. For each plane, the corresponding TDC value, multiplied by the drift velocity, allows to reconstruct a drift circle. At this point, the muon track is reconstructed as the best line tangent to the drift circles (Fig. 5.4).

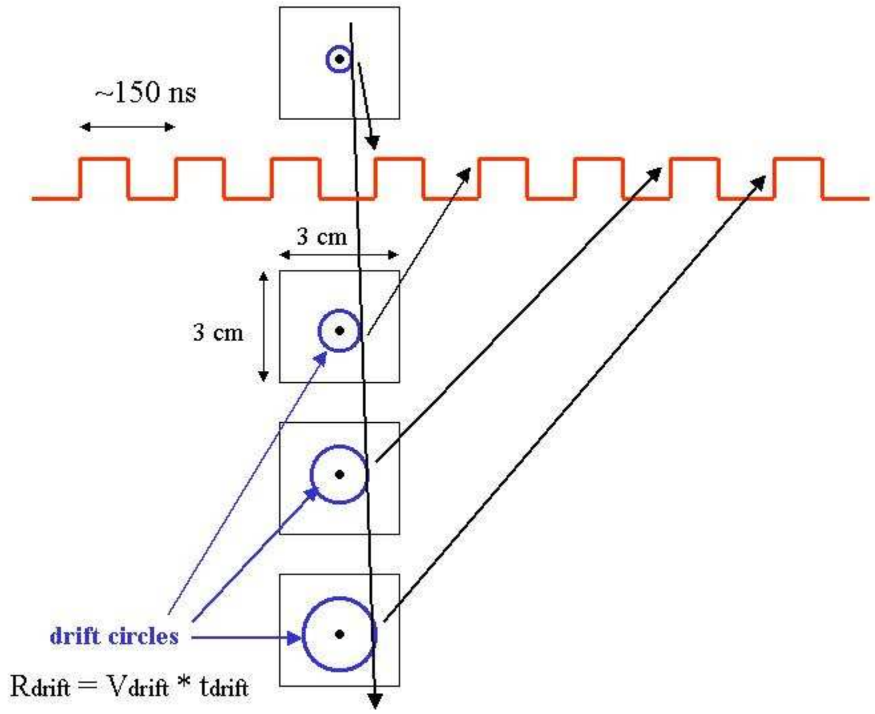

Figure 5.4: Limited streamer tubes used in drift mode: for each fired tube, the corresponding drift time is multiplied by the v_{drift} obtaining the drift circles. The muon track is reconstructed as the best line tangent to the drift circles.

The QTP electronics was not designed for drift time measurement and its relative linearity was tested only at larger time scale than 600 ns. Therefore, to avoid systematic effects and to fully understand the capability of the QTP system in such context, the electronics was checked in a test beam at CERN PS-T9 [87].

5.3 The CERN PS-T9 test beam

A slice of MACRO, Fig. 5.5, was reproduced using 14 coverless streamer tube chambers, each with dimension 25cm×3cm×200cm. For the rock absorbers, seven 40cm×40cm×32cm iron boxes were filled with rock from the Gran Sasso tunnel ($\rho = 2$ g cm^{-3}). As in MACRO, the gas mixture was He(73%)/n-pentane(27%). The test beam layout is shown in Fig. 5.5: the trigger was provided by the fast coincidence of the scintillators S1,S2,S3. The last scintillator, following a 60 cm iron slab, was used to suppress the $\pi^{\pm}$, $K^{\pm}$ contamination at high energy.

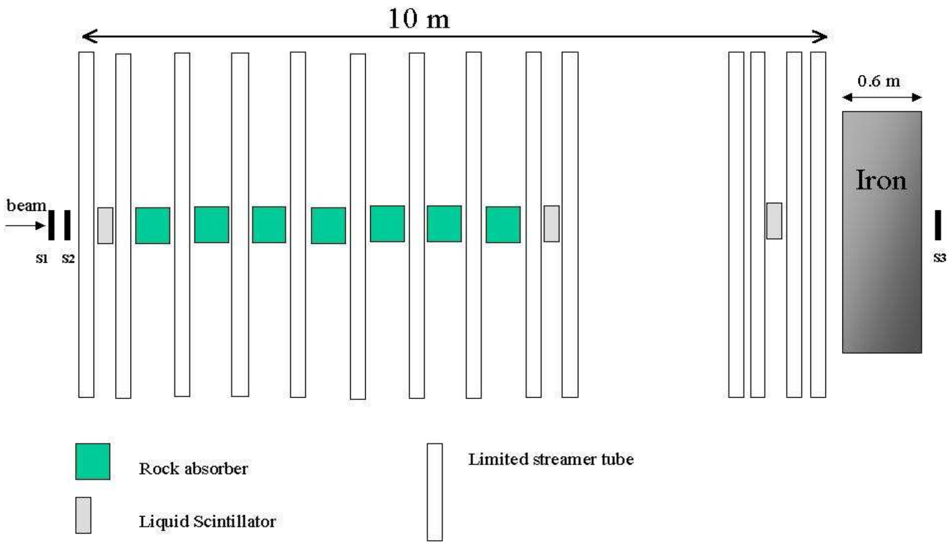

Figure 5.5: CERN PS-T9 test beam layout.

Each streamer tube chamber was equipped with a MACRO read-out card. As in MACRO, the analog output of a chamber was sent to a QTP channel (150 ns/bin), while the digital output, OR of the chamber signals, was sent to a Lecroy 2228A TDC (250 ps/bin). Such double measurement of the drift time allowed to make a comparison between QTP-TDCs and Lecroy TDCs event by event. The data acquisition was performed using LabView, running on a MacIntosh Quadra 950. Fig. 5.6 shows the plateau curve of the streamer tubes used in the test beam: a full efficiency is reached at HV=4050 V.

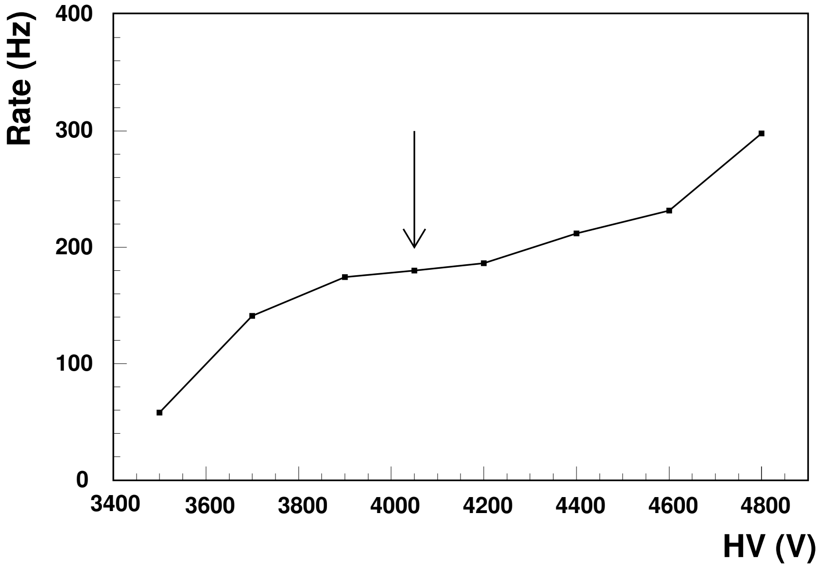

Figure 5.6: Plateau of the streamer tubes: the arrow indicates the working point (HV=4050 V).

The goals of the test beam runs were: (*i*) the study of the QTP-TDCs linearity, (*ii*) the study of the drift velocity in He/n-pentane mixture, (*iii*) the test of the software used for muon tracking. Moreover, the comparison of the muon energy reconstructed with the MCS analysis with respect to the beam nominal energy offered the possibility of an absolute energy calibration.

5.3.1 Test beam results

We collected 60 runs, with the beam stoppers closed, for about 10^5 muons with energy ranging from 2 to 12 GeV. As far as the check of the QTP electronics is concerned, we used only runs with absorbers out, i.e. the rock absorber were removed to allow the space resolution evaluation, otherwise spoiled by multiple scattering of muons.

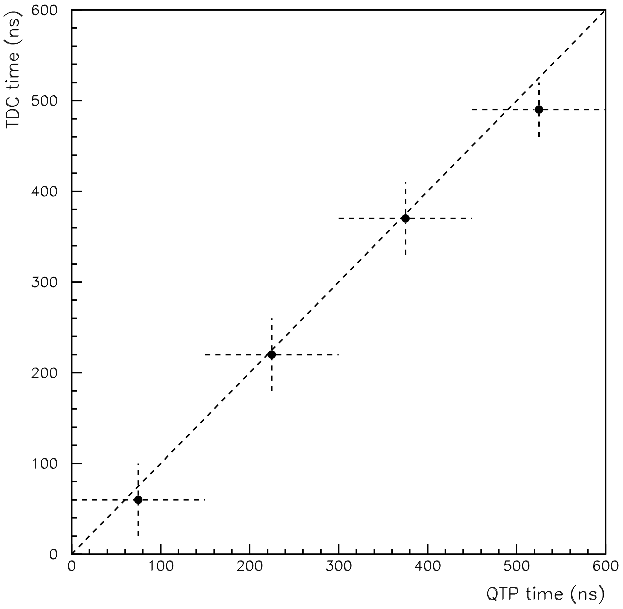

Figure 5.7: (a) Lecroy TDCs drift times as a function of QTP-TDCs times. The horizontal errors represent the bin width of the QTP-TDCs, the vertical errors represent the sigma of the gaussian fit of the corresponding Lecroy TDCs distributions.

As a first step we evaluated the QTP-TDCs linearity, by comparing their response to the one of the Lecroy TDCs. Fig. 5.7 shows the profile plot of such variables: for 4 given value of the QTP-TDC system (75 ns, 225 ns, 375 ns, 525 ns), we performed a gaussian fit of the Lecroy TDCs time distribution. The horizontal errors on the figure represent the bin width of the QTP-TDCs, while vertical errors represent the sigma of such gaussian fit: the QTP-TDCs response is linear within 8%.

The next step was the study of the drift velocity in He/n-pentane mixture. Since in the test beam configuration the muons hitted the detector perpendicularly, we used (r is the distance between the track and the center of the cell: it may range from 100 μm, which is the radius of the anode wire, to 1.5 cm,

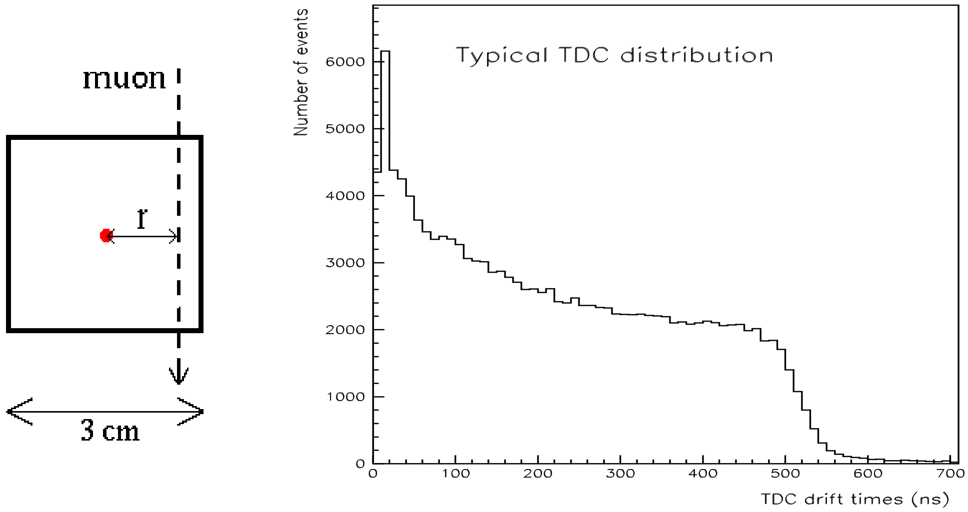

(a) (b)

Figure 5.8: (a) PS-T9 test beam: a muon crosses perpendicularly a streamer tube. (b) Typical TDC drift time distribution fitted to obtain the drift velocity.

see Fig. 5.8a)

$$\frac{dN}{dt} = \frac{dN}{dr}\frac{dr}{dt} = \frac{dN}{dr} \cdot v_{drift} = K \cdot v_{drift} \tag{5.4}$$

where dN/dt is the TDC drift time distribution, dN/dr is constant because the muon flux was the same on the whole cell and dr/dt is the drift velocity. The evaluation of v_{drift} can be obtained fitting the Lecroy TDC spectrum distribution. An example of a TDC drift time distribution is shown in Fig. 5.8b. The experimental results (black points in Fig. 5.9) were compared with the Monte Carlo predictions, given by the GARFIELD simulation [88]. We simulate the $3{\times}3$ cm^2 tubes filled with the MACRO gas mixture, obtaining for the drift velocity the continuous line of Fig. 5.9. The systematic error on the MC prediction (dashed lines in Fig. 5.9) was estimated introducing a 15% gas mixture variation. The experimental data are in satisfactory agreement with the simulation.

Once the TDC linearity has been checked and the v_{drift} has been measured, the test beam data were used to measure the space resolution. Fig. 5.10 shows

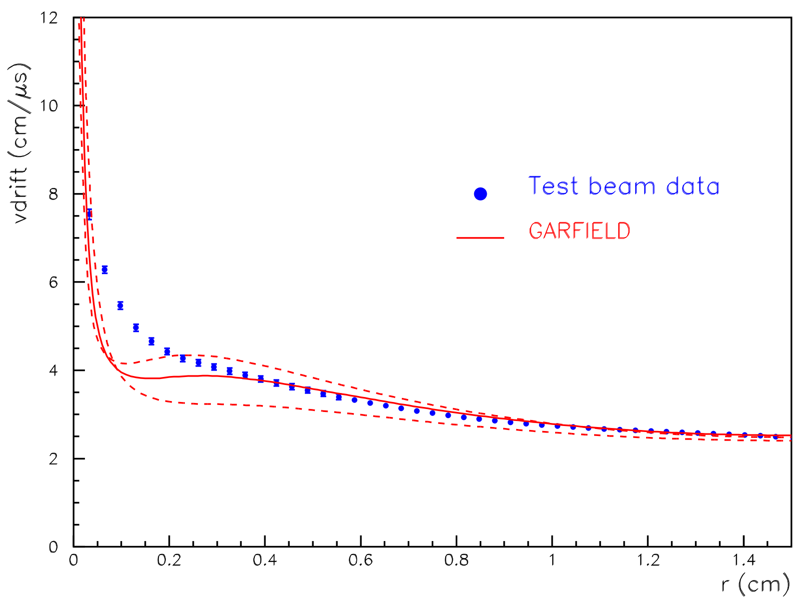

Figure 5.9: Drift velocity measured at the test beam (black points) compared with the GARFIELD expectation (continuous line). The dotted lines represent the effect of a 15% gas mixture variation.

the distribution of the residuals for the streamer tubes in drift mode using the Lecroy TDCs and the QTP-TDCs. In the first case a resolution of $\simeq 500$ μm is found, while for the second one we obtained a resolution of $\sigma \simeq 2$ mm. Such limit is very close to the value estimated by the QTP-TDCs resolution $\sigma = v_{drift} \cdot 150\text{ns}/\sqrt{12} \simeq 4\text{cm}/\mu\text{s} \cdot 150\text{ns}/\sqrt{12} \simeq 1.9$ mm.

Summarizing, the PS-T9 test beam have shown that: (i) no "hot-effects" are present in the QTP electronics: although designed for a different goal, such electronics can be successfully used to operate the streamer tubes in drift mode; (ii) the QTP-TDCs have a reasonable linearity; (iii) the drift velocity in He/n-pentane mixture is in good agreement with the GARFIELD simulation; (iv) the software tools are adequate to perform a reasonable muon track fit; (v) the ultimate space resolution of the MACRO streamer tubes, operated in

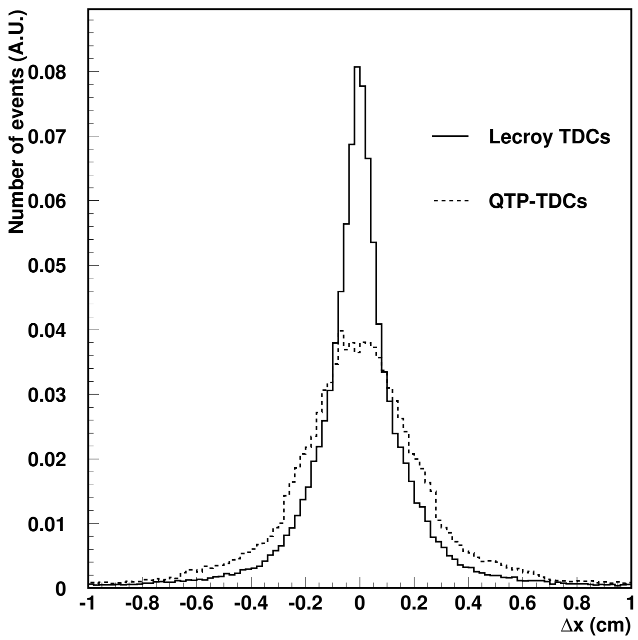

Figure 5.10: PS-T9 test beam data: residuals distribution from Lecroy TDCs (continuous line) and QTP-TDCs (dotted line).

drift mode, is $\sigma_{QTP} \simeq 2$ mm.

5.3.2 Test beam simulation

In the PS-T9 test beam, the nominal energy of the different runs refer to charged pions, produced in the proton-target interactions. The pions arrived to the experimental set-up already selected in momentum. The knowledge of the energy of muons incident on the detector is needed to make an absolute energy calibration, through a comparison between the muon energies reconstructed by the NN and the real ones. In order to obtain this goal, a GEANT based simulation of the apparatus was made: 10^6 charged pions with the nominal energy of the runs were sent normally to the experimental set-up. Their initial distance from the detector was about 65 m. For each event, the interactions with the materials were recorded step by step and also the produced particles were analyzed. We selected muons produced by pions which decayed before entering the detector: we registered the initial energies of those events which crossed the whole detector and the successive S4 scintillator (Fig. 5.5). The mean value and the sigma of the obtained initial energy spectra were compared to the reconstructed energy. These events represented the MC input of the muon energy estimate procedure, which I shall describe in the following section.

5.4 Muon energy estimate

The muon energies can be estimated in MACRO by measuring their multiple Coulomb scattering through the rock absorbers: the tests performed at CERN allow to calibrate such method making a comparison with the reconstructed value and the nominal energy of incident muons.

The muon mean deflection between two contiguous streamer tube planes is below the ultimate resolution obtainable with the MACRO streamer tubes in drift mode ($\sim$ 2 mm); it is thus not appreciable. For each muon event, we computed the following variables, sensitive to MCS: (*i*) the sigma of the residual distribution, (*ii*) the highest residual between the 14 available, (*iii*) the average of the residuals, (*iv*) the difference of the residuals of the three farthest hits along the track, (*v*) the slope of the "progressive fit" and (*vi*) the intercept of the "progressive fit".

We define "progressive fit" the absolute value of the residuals as a function of the number of the streamer tube plane (i=1,14). The concept of "progressive fit" is illustrated in Fig. 5.11. For a high energy muon, the average residual is roughly constant in the different planes, since the muon energy is almost constant while crossing the experimental setup. For instance, a 20 GeV muon loses less than 5% of its energy after crossing the detector. On the contrary, a low energy muon loses, by ionization, a high fraction of its energy when crossing the rock absorbers: as a result, the average residuals are higher for the last crossed planes. The linear fit of the absolute value of the residuals as a function of the streamer tube number, gives a relatively small slope for a high energy muon, while such slope is much larger for low energy muons (see Fig. 5.11).

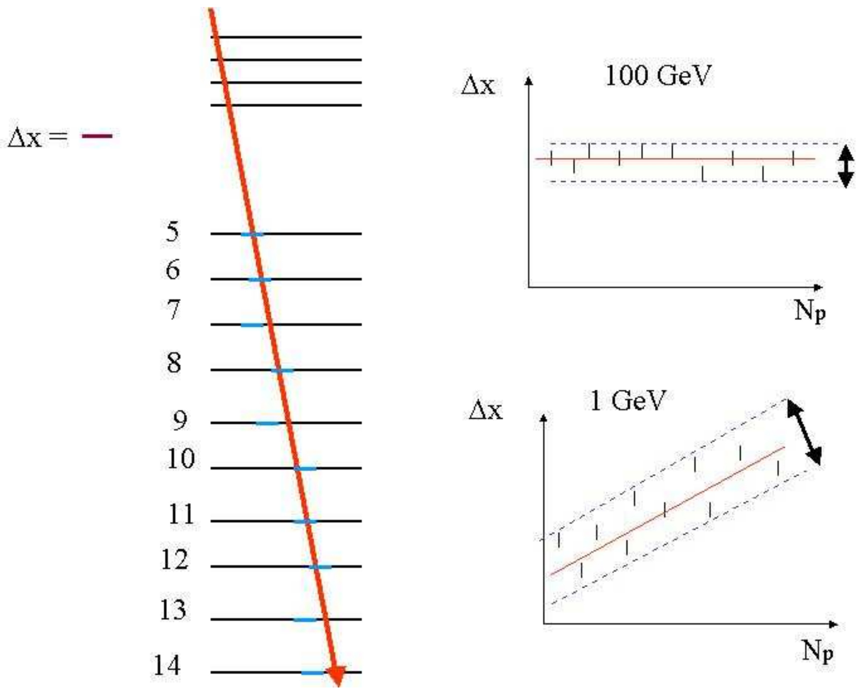

Figure 5.11: Illustration of the "progressive fit" of the absolute value of the residuals as a function of the number of the streamer tube planes.

5.4.1 The Neural Network

As already seen, we defined several input variables, each sensitive to MCS in different energy ranges. For these variables, a direct relation, like Eq. (5.1), between the sigma of the distribution and the muon energy does not exist; we needed a selection of cuts optimizing the result.

We followed a Neural Network (NN) approach choosing JETNET 3.0 [89], a standard package with a multilayer perceptron architecture and with back-propagation updating. If we indicate with $\vec{x}$ the vector of the input variables, a specific selection of cuts corresponds to a particular set of functions $o_i =$

$F_i(x_1, x_2, ...) = F_i(\vec{x})$. The aim of a NN is to give an automated choice of the function F_i which optimizes the results. In our algorithm, we have chosen the standard form

$$F_i(\vec{x}) = g\left[\frac{1}{T}\sum_j w_{ij}\, g\left(\frac{1}{T}\sum_k w_{jk}x_k + \theta_j\right) + \theta_i\right] \tag{5.5}$$

which corresponds to the "architecture" of Fig. 5.12. The "weights" w_{ij} and w_{jk} are the parameters to adapt to the data distributions and $g(x)$ is the non linear neuron activation function, of the form

$$g(x) = \frac{1}{2}\left[1 + \tanh(x)\right] = (1 + e^{-2x})^{-1} \tag{5.6}$$

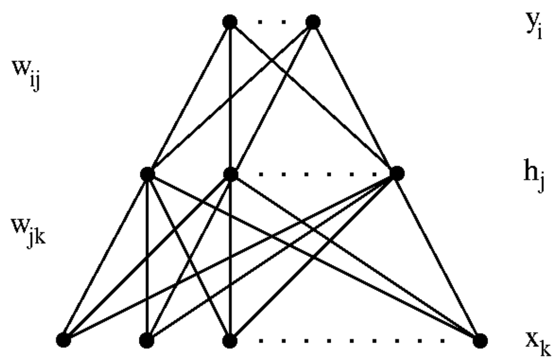

Figure 5.12: Architecture of a one hidden layer (h_j) neural network.

The bottom layer in Fig. 5.12 corresponds to the variables x_k and the top layer to the features o_i (F_i). The hidden layer enables non-linear modeling of the data. The scheme of Fig. 5.12 can be easily implemented with many hidden layers, increasing the complexity and the execution time of the program.

Before studying a set of new data, a NN needs a first step of training, during which it learns to recognize and to classify the events. The training procedure uses two separate samples of events, called "training events" and "testing events". In our case, the training files are MC data, containing, for each event, the MCS sensitive variables and the energy. We used 2 samples of 500 events; this number, statistically compatible with the ~ 400 MACRO events we had to analyze, was chosen after some checks as the one which optimized the NN performances. During the first cycle ("epoch"), the algorithm processes the training events, compares the reconstructed muon energy with the known value given in input and associates to the fit a mean square error.

The initial weights w_{ij}, w_{jk}, normalized to unit size, are changed by minimizing the error of the fit. At this point, the same algorithm is applied to the testing events and the same mean square error between the responses and the known initial values is calculated. For this architecture with non linear hidden nodes, there is not an exact procedure for minimizing the errors and to calculate the best values for the weights, so we used an iterative method, repeating the same procedure for about 100 times. While the error on the training events become smaller and smaller, at a certain point the error on the testing files starts to increase: this is the "overtraining" situation, where the NN learns to recognize only the events with precise characteristics and becomes not able to classify events with similar, but not equal, characteristics. In our case, 100 epochs were enough to give a good precision in estimating the muon energies. The output of the NN is a parameter ranging between 0 and 1. Since the best feature of a NN is a binary classification of the events and our output must be a continuous variable (it estimates event by event the energy of muons in a large range), we made the energy values of $E_\mu = 1.5, 3, 20, 50$ and 100 GeV corresponding to the $\log_{10} E_\mu$ values for the output parameter. The training was also made separately for 6 values of the zenith angle Θ $(1^\circ, 10^\circ, 20^\circ, 30^\circ, 40^\circ, 50^\circ)$, because different values of Θ correspond to different amounts of crossed material.

Fig. 5.13 shows the results: the average NN parameter output (empty squares) increases as a function of the muon energy up to $E_\mu \simeq 40$ GeV and saturates at higher energies. The use of the streamer tube system in drift mode combined with a neural network approach allows therefore to estimate the muon energy up to $\simeq 40$ GeV.

The data collected during the PS-T9 test beam runs provide an absolute

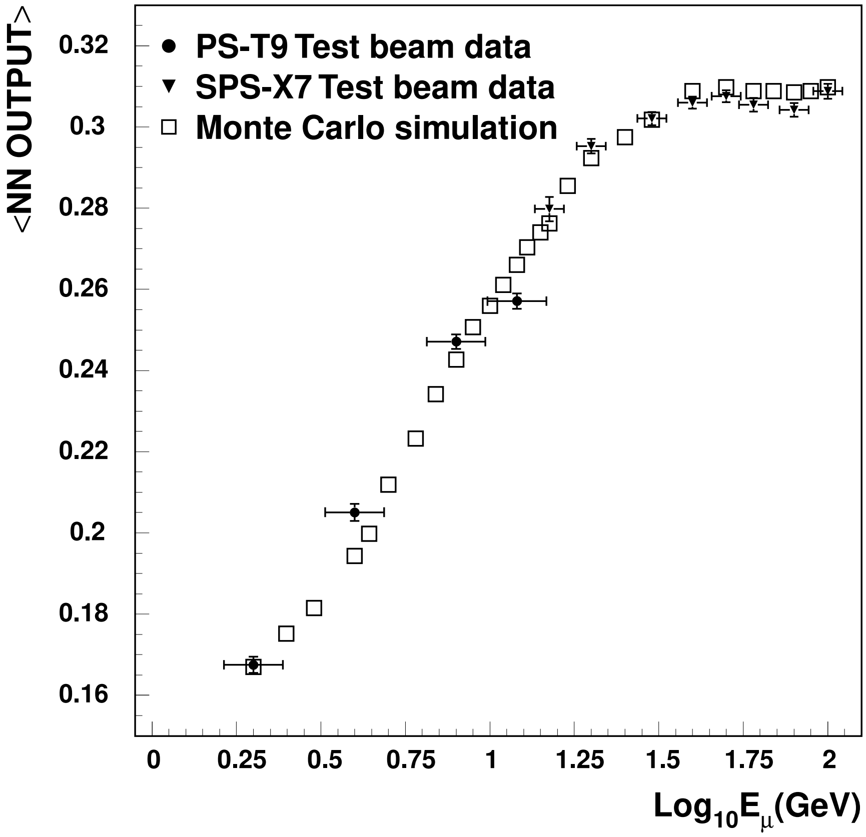

Figure 5.13: Average neural network output as a function of $\log_{10} E_\mu$: PS-T9 test beam data (black circles), SPS-X7 test beam data (black triangles) and MC prediction (empty squares).

energy calibration of the method, up to muon energies of 12 GeV. In order to check the NN output in all the energy range below the saturated region, we performed a second test at the CERN SPS-X7 beam. Muons with energy ranging between 15 and 100 GeV were collected, by the same setup used previously, Fig. 5.5.

Fig. 5.13 shows the comparison between the test beam data and the Monte Carlo prediction: the empty squares represent the Monte Carlo expectation, the full circles show the PS-T9 test beam data, while full triangles show the SPS-X7 test beam data.

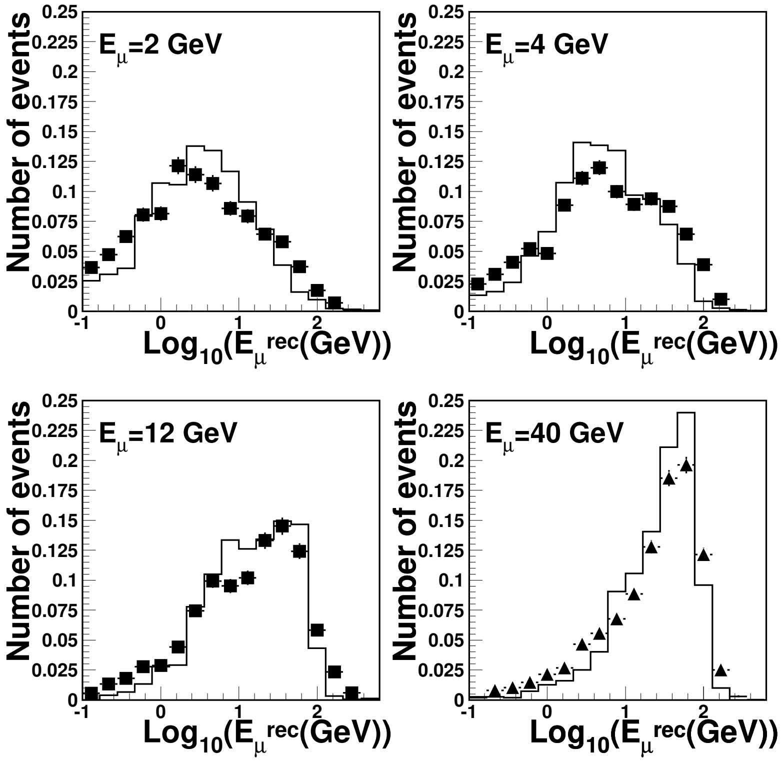

Figure 5.14: Reconstructed muon energy for 2, 4, 12 and 40 GeV muons: the black squares ad triangles refer, respectively, to the PS-T9 and SPS-X7 test beam data, the continuous line represents the MC simulation.

The MC simulation of Fig. 5.13 took into account the background measured at the CERN-PS/SPS; to both Monte Carlo and test beam events we applied a selection requiring at least 3 fired limited streamer tube layers over the last 4 ones (see Fig. 5.5). The NN output obtained with the test beam data is properly reproduced by the Monte Carlo simulation.

To reconstruct the muon energy, the NN output was calibrated on an event by event basis, using the following procedure: a function $f(output)$ of the NN output was chosen to obtain for each event the real energy E_μ^{real}. In this way, for each muon we had $E_\mu^{real} = f(output)$. At this point, for a given NN output value, the energy of the corresponding muon E_μ^{rec} was estimated by $f(output)$. Fig. 5.14 shows the reconstructed energy for $E_\mu = 2, 4, 12, 40$ GeV: the data

E_μ^{real} (GeV)	2.	3.	5.	10.	40.
E_μ^{rec} (GeV)	$(2^{+6}_{-1.5})$	$(3^{+12}_{-2.5})$	(5^{+18}_{-4})	(10^{+30}_{-8})	(40^{+60}_{-21})

Table 5.1: Comparison between the reconstructed muon energy E_μ^{rec} and the real one E_μ^{real}, for 5 different values.

collected at the PS-T9 test beam (full squares) and at the SPS-X7 test beam (full triangles) are compared with the Monte Carlo expectation (continuous line), showing a reasonable agreement. The nominal and reconstructed energies are given in Table 5.1. The errors were estimated by the E_μ^{rec} distribution; the quoted intervals contain the $\pm 1\sigma$ of the events.

5.5 Conclusions

The QTP-TDCs offered the possibility of using the MACRO limited streamer tubes in drift mode. The test beam runs performed at the CERN PS/SPS confirmed such possibility, excluding the presence of undesired effects in the QTP electronics. The QTP system allows to improve the streamer tube space resolution by a factor $\simeq 3.5$, from $\sigma \simeq 1$ cm to $\sigma \simeq 3$ mm. These performances were fully exploited by using a neural network approach in order to obtain an energy estimate of the muons crossing the detector: the average neural network output increases as a function of the muon energy up to $\simeq 40$ GeV and the comparison between MC expectations and test beam data shows a good agreement. Such comparison demonstrates the proper implementation of the analysis method, which can be successfully applied to the data collected by MACRO. As we shall see in the following chapters, this procedure allowed to estimate the energies of neutrino induced upgoing muons in MACRO and thus to study ν_μ oscillations in terms of L/E_ν.

Chapter 6

The MACRO data analysis

6.1 Introduction

The PS and SPS tests showed the feasibility of a Multiple Coulomb Scattering analysis to estimate the energy of upgoing muons in MACRO (Chap. 5). The improvement of the space resolution obtained by using the streamer tubes in drift mode and the NN approach allowed to estimate the muon energy event by event up to $E_\mu \simeq 40$ GeV. In this chapter, I shall describe the same procedure of Chap. 5 applied to the MACRO data. After the study of the space resolution performed with the downgoing muons and the software alignment of the apparatus, the whole sample of upthroughgoing muons has been analyzed in terms of neutrino oscillations. The NN output was used to divide the upthroughgoing muons in 4 energy subsamples and to estimate the ratio L/E_ν for each event.

6.2 Data analysis

6.2.1 The MACRO space resolution

To estimate the performance of the streamer tubes operated in drift mode in MACRO, we analyzed a downgoing muon sample, whose average energies is

$\langle E_\mu \rangle \simeq 250$ GeV [90].

We considered the muon tracks reconstructed with the standard MACRO tracking, selecting those hits made of a single fired tube. For each digit used in the standard tracking, a dedicated subroutine filled a matrix containing the QTP addresses and timing informations; for each hit, the corresponding QTP-TDC value was read in a time window of 2 μs. Given the background rate in the MACRO streamer tubes, $\simeq 40$ Hz m^{-2}, this corresponds to $\simeq 480$ Hz on 4 chambers (1 QTP channel), giving a probability $\simeq 10^{-3}$ for a spurious hit to mimic a genuine QTP-TDC count. The time corresponding to each digit has been obtained subtracting it from the minimum time of the event. Such procedure assumes that the shorter time corresponds to the digit closer to the wire. The delay due to the signal propagation along the wire was added to each time. After converting the TDC values in drift radii, by using the drift velocity measured at test beam, we reconstruct for each plane a drift circle. A global fit of the track tangent to the circles is performed (Fig. 5.4).

As a first step, this procedure was used to produce an alignment database of the detector. The standard MACRO database was in fact computed using the streamer tube in digital mode ($\sigma \simeq 1$ cm): the improved space resolution achieved by this method requires an improvement also in the database precision. We used $15 \cdot 10^6$ downgoing muon tracks, to align the wire positions with the iterative software procedure described below. Since the MACRO streamer tubes are made of PVC (§4.2.1), a high flexibility material, part of the disalignment may come from the deviation from a straight line along the main axis of each streamer tube (sagitta effect): the streamer tube length (12 m) was divided in six slices and we computed the residuals in each slice separately. We handled a matrix of $14 \times 2304 \times 6$ elements, where the first index runs on the number of horizontal planes, the second one on the wire number and the last one on the portion of the wire over his main axis. We adopted an iterative procedure, by adding at each step, for each element of the matrix, the mean value of the gaussian of the residuals belonging to each portion of wire. As a results of this procedure, the residuals of the downgoing muons reached a $\sigma = 3$ mm. To compare this resolution with the MC predictions, we inserted the drift velocity measured at the test beam (see §5.3.1) in the simulation code GMACRO. Fig. 6.1 shows the distribution of the track residuals for the MACRO streamer tubes in drift mode (black circles) and the MC simulation (continuous line). The residuals of the downgoing muons show a good agreement with the MACRO simulation; the dotted line shows the residuals distribution for the streamer tubes used in digital mode ($\sigma = 1$ cm). An improvement of a factor $\simeq 3.5$ in the space resolution ($\simeq 12$ in σ_p/p, see Eq. (5.3)) has been obtained.

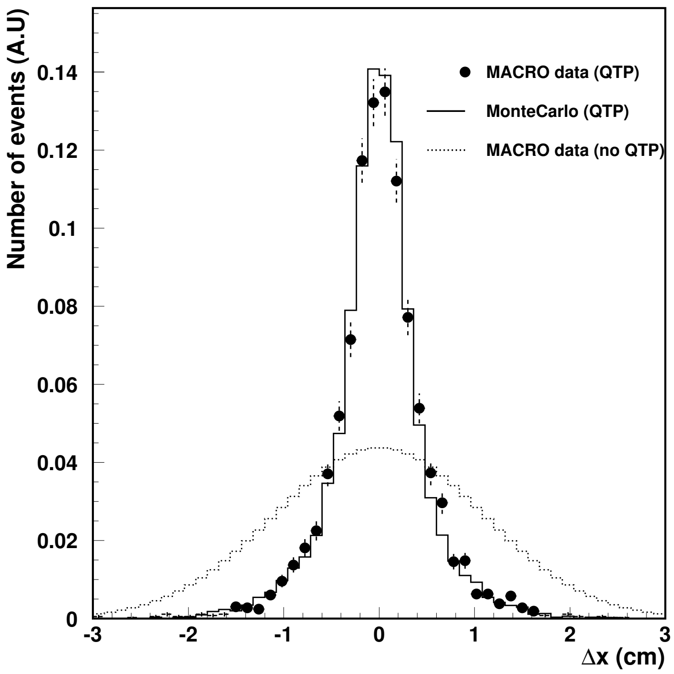

Figure 6.1: MACRO residual distribution (black points) obtained using the streamer tubes in drift mode ($\sigma \simeq 3$ mm) compared with the MC expectation (continuous line). The dotted line represents the same distribution obtained using the streamer tubes in digital mode ($\sigma \simeq 1$ cm).

As far as MACRO data is concerned, the resolution is spoiled with respect to that measured at the PS-T9 test beam ($\sigma = 2$ mm), obtained without the absorbers. According with our simulation, the most important contribution to this difference comes from both δ-rays and radiated photons produced in the rock absorbers. They sometimes spoil the space resolution, producing early streamers with respect to those produced by the muon, resulting in smaller drift radii. Moreover, the MACRO downgoing muons, although with average energy $\langle E_\mu \rangle \simeq 250$ GeV, still suffer multiple scattering, mainly coming from the low energy tail. Finally, streamer tube gas mixture variations may affect the drift velocity.

This hypothesis has been demonstrated during the second test beam (see §5.3), performed at the CERN SPS-X7, where high energy muons were available. The sigma of the residuals obtained with $E_\mu = 100$ GeV and rock absorbers inserted, was $\sigma \simeq 0.294 \pm 0.003$ cm, in good agreement with that obtained using the MACRO downgoing muon data.

6.2.2 The upthroughgoing muon standard selection

For the MCS analysis, we used the whole sample of upthroughgoing muons collected with the MACRO attico in full operation, that is from April 1994 to December 2000, for a total livetime of 5.5 years. We considered the upgoing muons selected by the time of flight method, performed by the scintillators with a 600 ps resolution, and tracked with the streamer tubes, which reconstruct the trajectory with a 1 cm resolution on each plane.

The discrimination technique of upgoing muons from the downgoing atmospheric ones was the time of flight measurement, illustrated schematically in Fig. 6.2. The analysis of more than 40 million atmospheric muons yielded a rejection factor of $\sim 10^{-7}$ against the background caused by showering events and radioactivity in coincidence with muons. The main cut was the requirement that the position of a muon hit along a scintillation counter evaluated from timing agrees within ± 70 cm with that from streamer tubes.

The $1/\beta$ distributions are important because they are proportional to the

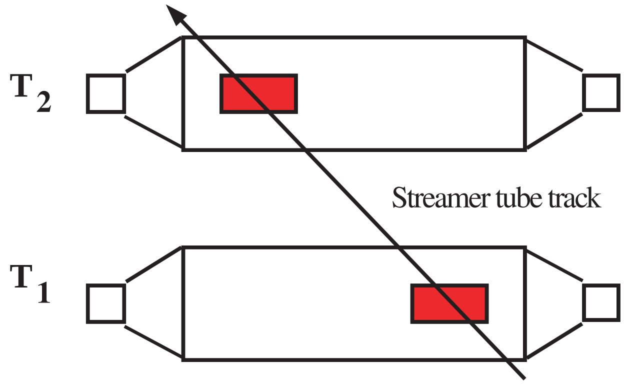

Figure 6.2: Illustration of the time of flight technique.

time of flight of particles. They are given by

$$1/\beta = \frac{c \cdot (T_1 - T_2)}{L} \tag{6.1}$$

where L is the path length, c is the light velocity in vacuum, T_1 and T_2 are the measured times in the 2 scintillation counters. Fig. 6.3 shows the $1/\beta$ distribution for the events collected with the detector in full configuration. The shaded area refers to events crossing 3 scintillator boxes, the larger area refer to events crossing 2 or 3 scintillator boxes. In our convention, upgoing muons have $1/\beta \simeq -1$ and downgoing muons have $1/\beta \simeq 1$. The upgoing muons were selected requiring $-1.25 \leq 1/\beta \leq -0.75$ (dotted lines in Fig. 6.3). MACRO measured 863 events in this $1/\beta$ range. The background due to incorrect β measurements, 22.5 events, was estimated from the events outside the upgoing muon peak.

The background due to low energy upgoing particles, mainly pions, induced by undetected downgoing muons interacting in the rock surrounding the detector, is reduced to $\sim 1\%$ requiring more than 200 gr cm^{-2} of material crossed in the lower part of MACRO [91]. The upgoing particles due to atmospheric downgoing muon interactions and surviving this cut were 14.2.

Moreover, the azimuth angle region from $-30°$ to $120°$ is excluded for horizontal upgoing muons ($\cos\Theta > 0.1$), due to insufficient rock overburden.

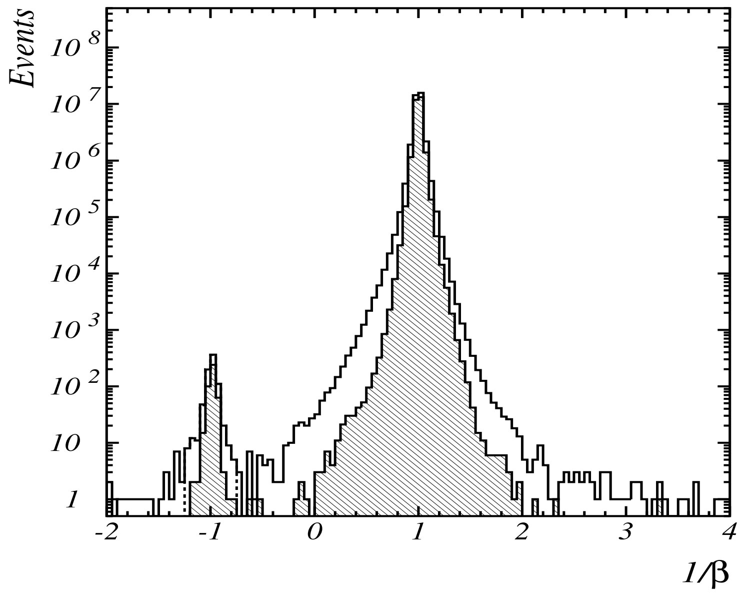

Figure 6.3: $1/\beta$ distribution for the events collected during the full detector run. The shaded area refers to events crossing 3 scintillator boxes, the larger area refer to events crossing 2 or 3 scintillator boxes. The vertical dotted lines show the range $-1.25 \leq 1/\beta \leq -0.75$ of upthroughgoing muons.

For muons crossing 3 scintillator layers, a linear fit of the times as a function of the path length is performed and a cut is applied on the χ^2. Further minor cuts are applied to the events crossing only two scintillation counters. Moreover, 17 events resulting from the neutrino interactions in the bottom scintillator layer were excluded from the analysis.

The total number of events survived after the analysis cuts and the background subtraction was 809.

6.2.3 The upthroughgoing muon MCS analysis

Among the upthroughgoing muon tracks, we selected hits belonging to the track and made of a single fire tube, to associate without ambiguity the QTP time informations. Spurious background hits have been avoided requiring a time window of 2 μs around the trigger time. Finally, we selected events with at least four streamer tube planes with valid QTP informations. The drift circles were reconstructed and fitted using the same tracking procedure developed to analyze the test beam data. After the described selection cuts, 348 events survived.

The Neural Network was trained using a special set of MC events with known input energy, crossing the detector at different zenith angles. Moreover, a different training for events crossing and non-crossing the attico was performed, because for the first case the energy is independent from the zenith angle, while for the latter case the energy is related to the zenith angle. This happens because a fraction ($\leq 10\%$) of upgoing muons stopping in the lower part of MACRO survives the selection cuts for upthroughgoing muons. For example, an upgoing muon stopping just below the second horizontal scintillator layer (see Fig. 2.13) can produce a shower hitting the scintillator and is interpreted as an upthroughgoing muon. In this case, both the zenith angle and the energy are related to the range traveled through the absorbers.

The procedure of calibration of the NN output described in §5.4.1 was used to reconstruct event by event the residual muon energy E_μ and the corresponding neutrino energy E_ν. The relative uncertainties on the reconstructed values are estimated to be $\sigma_{E_\mu} \simeq 100\%$ for E_μ and $\sigma_{E_\nu} \simeq 150\%$ for E_ν. They were computed as $\sigma(E^{rec} - E^{real})/E^{real}$.

Fig. 6.4 shows the average NN output as a function of E_μ (top) and E_ν (bottom). The saturation value for the residual muon energy, $E_\mu \simeq 40$ GeV, corresponds to a neutrino energy $E_\nu \simeq 200$ GeV. The comparison with the muon and neutrino energy spectra (dotted lines in Fig. 6.4) shows that about 80% of muon and neutrino energies are below the saturation point.

To compare the real data with the Monte Carlo expectations, we performed a full simulation chain by using the Bartol neutrino flux [35] and the parton distributions of ref. [37], as explained in §3.7. The muon propagation from the interaction point up to the detector level was performed with the FLUKA [44]

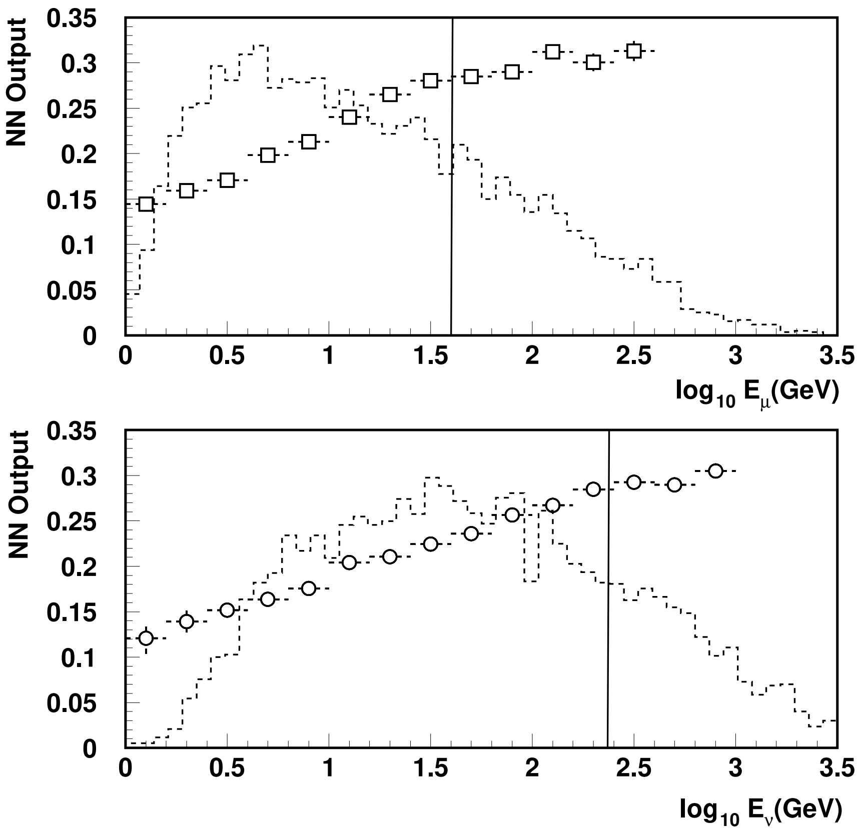

Figure 6.4: NN output as a function of the residual muon energy E_μ (top) and of the neutrino energy E_ν (bottom). The dotted lines represent the muon (top) and neutrino (bottom) energy spectra. The vertical lines indicate the saturation energy value: the $\simeq 80\%$ of muon and neutrino energies are below such value.

code; the muon simulation in the detector was performed with the GMACRO Monte Carlo (§4.5). For each muon crossing the apparatus, the complete history (parent neutrino energy, interaction point, muon energy, etc.) of the event has been recorded, for a total livetime of 35 years.

If the upgoing muon deficit and the zenith distribution distortion were due to neutrino oscillations with parameters $\Delta m^2 \sim 10^{-3}$ eV^2 and $\sin^2 2\theta \simeq 1$, they would not manifest at all neutrino energies. As shown in Fig. 5.2, for $\Delta m^2 = 2.5 \cdot 10^{-3}$ eV^2 the effect of oscillations is expected to be stronger at

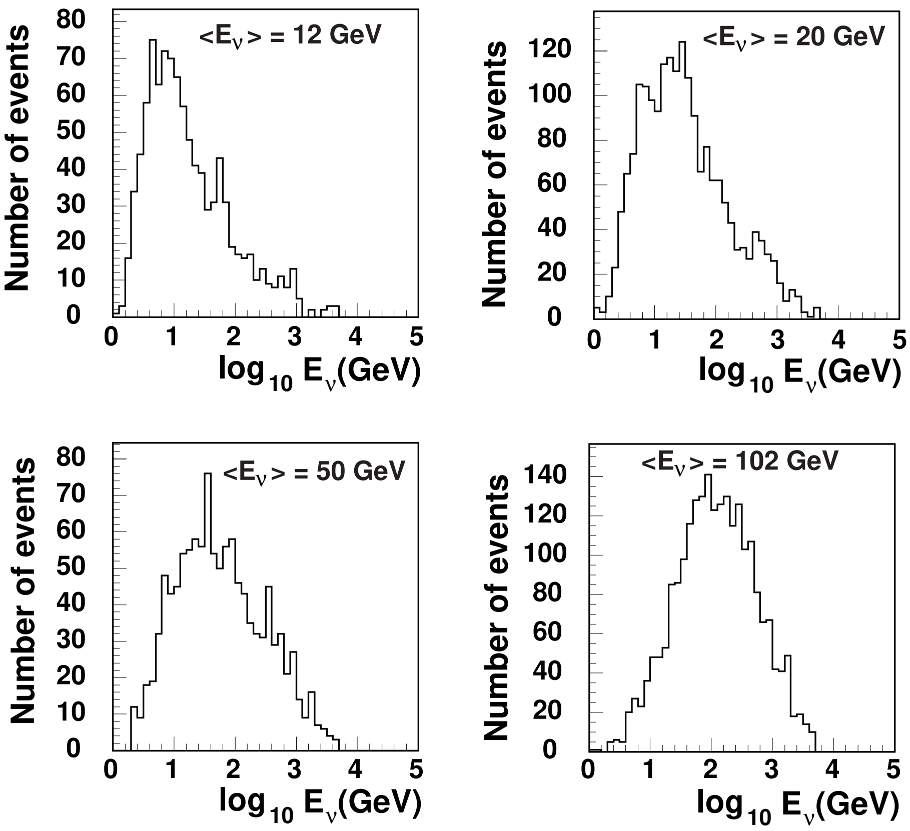

Figure 6.5: Neutrino energy distributions of upthroughgoing muons in four energy windows selected by the neural network.

low muon energies ($E_\mu \leq 20$ GeV) and to become $< 5\%$ at higher energies ($E_\mu \geq 100$ GeV).

The informations on the reconstructed neutrino energy given by the neural network were used to separate the upgoing muons in four energy subsamples and to study them in terms of neutrino oscillations. This choice was the result of two requests: (i) the number of events in each subsample had to be comparable; (ii) we had to take into account the resolution of the E_ν estimate. Fig. 6.5 shows the neutrino energy distributions corresponding to the four energy windows selected. The median neutrino energies of these four windows were 12 GeV (low), 20 GeV (medium-low), 50 GeV (medium-high) and 102

GeV (high), respectively.

The zenith angle distributions of the ν_μ-induced muons in the four subsamples are compared with the MC simulations assuming no oscillations (blue boxes) in Fig. 6.6. The errors on the Monte Carlo simulation contain the $\pm 17\%$ uncertainty on the neutrino flux (see Chap. 3) and the statistical error, added in quadrature. The plots show that at low energies there is a disagreement between the data and the no-oscillation Monte Carlo, while the agreement increases with muon energies, according with the oscillation hypothesis.

We performed a χ^2 analysis. To compute the χ^2 we used the formula:

$$\chi^2 = \sum_{i=1}^{Nbin} \frac{(N^i_{data} - \alpha N^i_{MC})^2}{\sigma^2} + \frac{(1-\alpha)^2}{\sigma^2_\alpha} \tag{6.2}$$

where $Nbin$ is the number of bins of the distributions, N_{data} and N_{MC} are the experimental and simulated events/year, α is the ratio $\sum N_{data}/\sum N_{MC}$ computed for each window, $\sigma = \sqrt{(\alpha N^i_{MC})^2 + (0.05 \cdot \alpha N^i_{MC})^2}$ and $\sigma_\alpha = 0.17$. The first term of Eq. (6.2) is the shape contribution to the χ^2 computation; in this case we quoted a 5% systematic error. The second term of Eq. (6.2) takes into account the normalization contribution to the χ^2; in this case, the systematic (scale) uncertainty σ_α has been quoted at 17%, see Chap. 3.

The χ^2 probabilities for the no-oscillation hypothesis in these four subsamples were computed on the basis of the zenith angle shape distribution and are 1.8% (low), 28% (medium-low), 33% (medium-high) and 88% (high), respectively. The χ^2 probabilities increase with the neutrino energy.

A similar plot, Fig. 6.7, was obtained putting in the Monte Carlo simulation the oscillation parameters $\Delta m^2 = 2.5 \cdot 10^{-3}$ eV^2 and $\sin^2 2\theta = 1$. The corresponding probabilities, always greater than 10%, are essentially energy independent.

6.2.4 The L/E_ν distribution

The main purpose of this thesis is the study of the oscillation probability as a function of L/E_ν. For this goal, the output of the NN has been calibrated on an event by event basis to have a linear response as a function of $\log_{10}(L/E_\nu)$, as already seen for the previous estimates of E_μ and E_ν. The distance L traveled by the neutrino from the production to the interaction points is measured with a $\sim 3\%$ precision by using the reconstructed zenith angle of the tracked muons. The resolution on the ratio L/E_ν is fully dominated by the uncertainty in the neutrino energy estimate, giving a global relative uncertainty of $\simeq 150\%$. The oscillation probability (Data/MC distribution) as a function of $\log_{10}(L/E_\nu)$ is shown in Fig. 6.8. The black points indicate the trend of the real data, the shaded regions, referring to the no-oscillation and oscillation MC, indicate the statistics uncertainties.

6.3 Conclusions

The sample of upthroughgoing muons measured by MACRO has been analyzed in terms of two flavours neutrino oscillations, using the MCS informations to estimate the residual muon energy and, then, the neutrino energy. The improvement in the spatial resolution by a factor 3.5, from ~ 1 cm to ~ 3 mm, allowed the estimate of the neutrino energy up to $\simeq 200$ GeV. The output of the Neural Network allowed to separate the whole sample of upthroughgoing muons in four subsamples, whose zenith angle distributions are in agreement with the oscillation MC with the parameters determined by the standard MACRO analysis. As expected, the agreement between the data and the MC without oscillations increase with the muon energy. The NN output was calibrated on an event by event basis to obtain for each event the reconstructed $\log_{10}(L/E_\nu)$. The oscillation probability (Data/MC distribution) as a function of $\log_{10}(L/E_\nu)$ shows a good agreement with the MC with $\nu_\mu \longleftrightarrow \nu_\tau$ oscillations and is inconsistent with the no-oscillation MC.

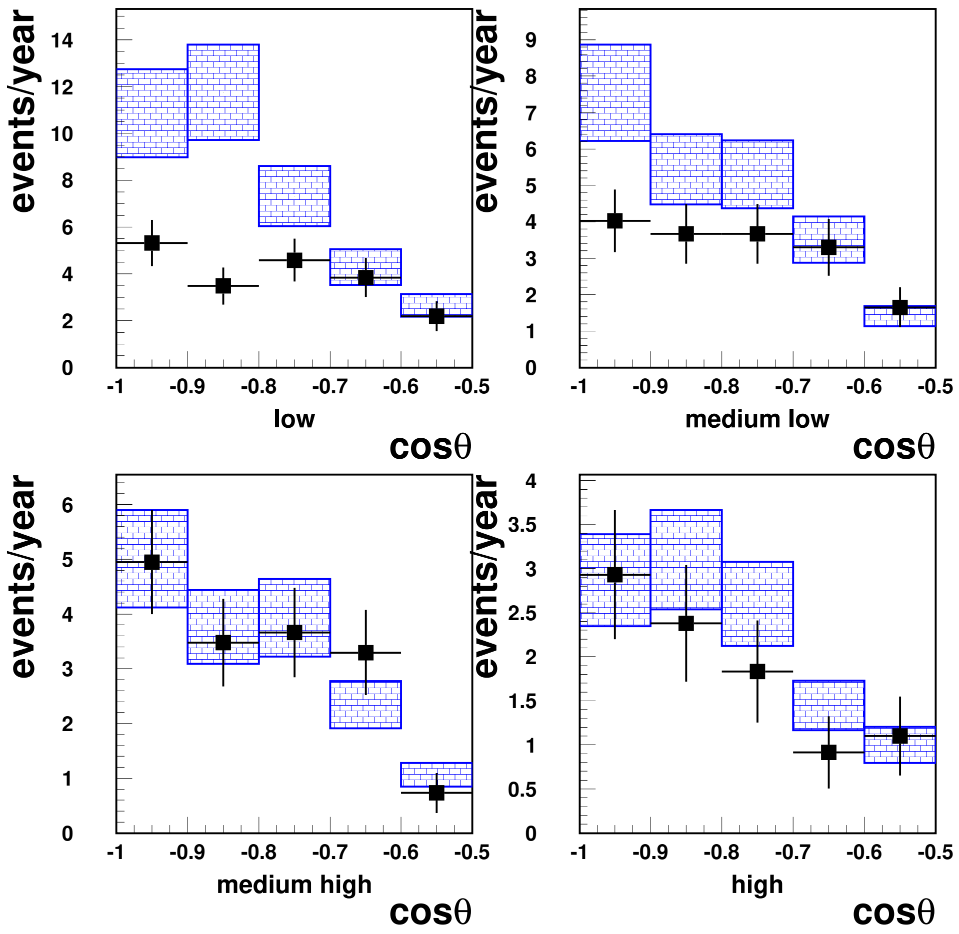

Figure 6.6: Zenith angle distributions of upthroughgoing muons in four energy windows. The black points are the data, the boxes show the MC expectations for the no-oscillation hypothesis (statistical errors plus 17% systematic uncertainty on the flux).

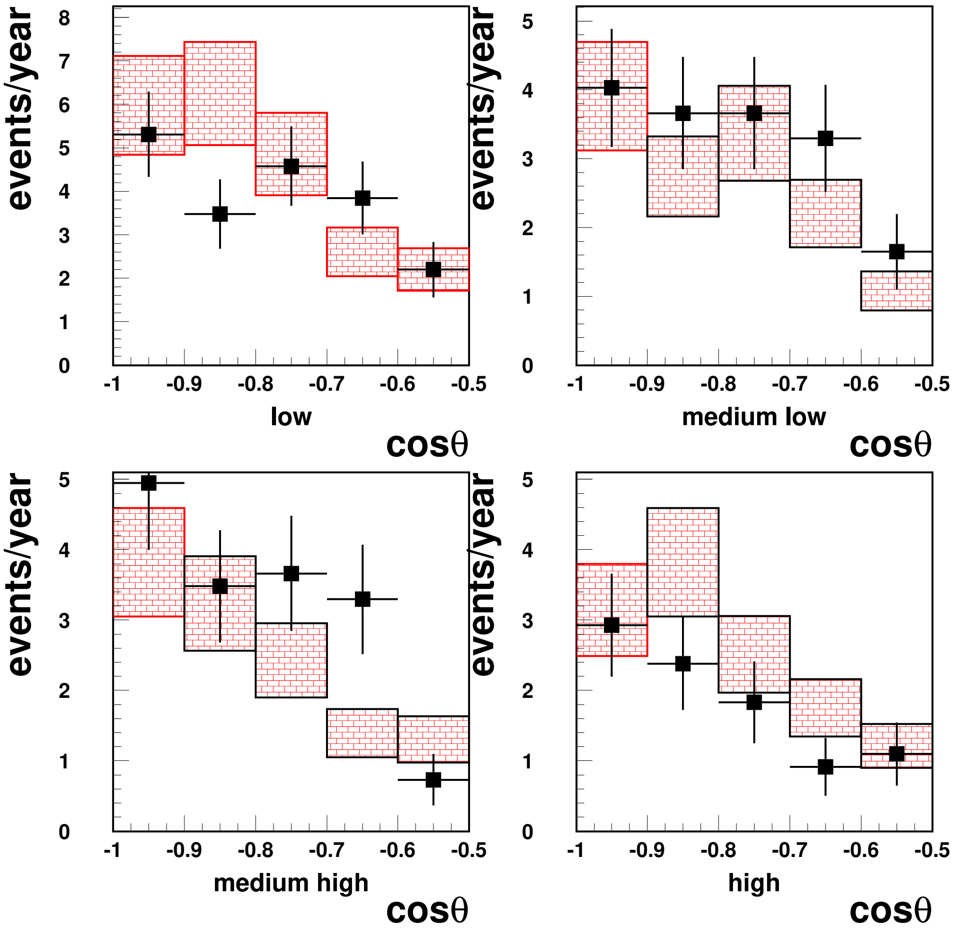

Figure 6.7: Same plot of Fig. 6.6, where the no-oscillation MC has been substituted by the MC assuming neutrino oscillations with $\Delta m^2 = 2.5 \cdot 10^{-3}$ eV^2 and $\sin^2 2\theta = 1$.

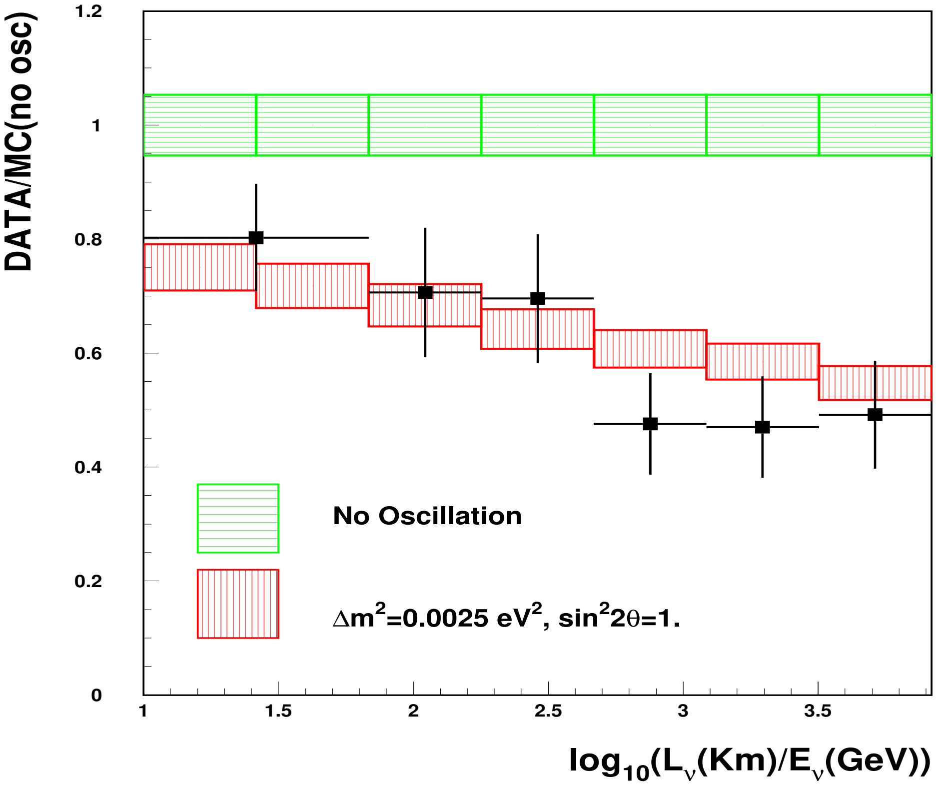

Figure 6.8: Ratio between data and no-oscillation MC as a function of L/E_ν for the MACRO upthroughgoing muons. The black points are the real data, the boxes represent the MC expectations for the no-oscillation hypothesis and for oscillations with $\Delta m^2 = 2.5 \cdot 10^{-3}$ eV^2 and $\sin^2 2\theta = 1$.

Chapter 7

Conclusions

The main goal of this thesis was the study of atmospheric $\nu_\mu \longleftrightarrow \nu_\tau$ oscillation probability in terms of L/E_ν, through a Multiple Coulomb Scattering analysis of neutrino-induced upthroughgoing muons.

During the full period of data taking, MACRO detected 809 upthroughgoing muons, which showed a global deficit and an anomalous zenith angle distribution with respect to the MC predictions neglecting neutrino oscillations. The standard MACRO analysis, taking into account the number of events and the zenith angle distribution, is in agreement with the $\nu_\mu \longleftrightarrow \nu_\tau$ oscillation hypothesis and yields the best fit values $\sin^2 2\theta = 1$ and $\Delta m^2 = 2.5 \cdot 10^{-3}$ eV^2 for the oscillation parameters.

Although the energy of an upgoing neutrino is not directly measurable, because in a CC interaction it is shared by the upgoing muon and by the hadrons, Monte Carlo simulations show that the muon energy at the detector level (residual muon energy) still preserves informations about the parent neutrino energy. As MACRO was not equipped with a magnet, the only way to estimate the muon energy is through their Multiple Coulomb Scattering in the absorbers.

The space resolution of the standard tracking system allows an estimate of E_μ only up to $\simeq 10$ GeV. We used the limited streamer tubes in drift mode, retrieving the time informations from the TDC of the QTP system. A global check of the QTP electronics, made at the CERN PS/SPS beams, showed the feasibility of the MCS analysis and demonstrated an improvement of the space resolution by a factor 3.5 (from $\simeq 1$ cm to $\simeq 3$ mm).

This technique was followed by a Neural Network approach. Some variables sensitive to MCS were given in input to the NN, previously trained to estimate the muon energy with MC events with known energy and different zenith angles. The NN allowed to estimate the muon energy event by event, with a relative uncertainty of about 100%. According to the NN output, the whole sample of upthroughgoing muons was separated in four subsamples, of different average energies; their zenith angle distributions show good agreement with the oscillation predictions. The NN was also used to estimate event by event the $\log_{10}(L/E_\nu)$ values; this allowed to study the trend of the L/E_ν distribution of the data and to compare it with the MC predictions. The good agreement of the data with the $\nu_\mu \longleftrightarrow \nu_\tau$ oscillation hypothesis with the parameters estimated by the independent standard analysis of upthroughgoing muons supports this strong evidence.

The MCS analysis result will be used to obtain the allowed regions for the oscillation parameters in the $\sin^2 2\theta - \Delta m^2$ plane.

Bibliography

[1] B. Pontecorvo, Zh. Eksp. Teor. Fiz. 33 (1957) 549; Zh. Eksp. Teor. Fiz. 34 (1958) 247; Zh. Eksp. Teor. Fiz. 53 (1967) 1717.

[2] G. Giacomelli, M. Giorgini and M. Spurio, *Atmospheric neutrino oscillations*, Proc. of the 6^{th} School on Non Accelerator Astroparticle Physics, Trieste, Italy, 2001.

[3] D. Vignaud, *Solar and supernovae neutrinos*, Proc. of the 6^{th} School on Non Accelerator Astroparticle Physics, Trieste, Italy, 2001.

[4] The LEP Coll. (Aleph, Delphi, L3, OPAL), *A combination of preliminary electroweak measurements and constraints on the Standard Model*, CERN-EP/2000-153, (2000).

[5] Z. Maki, M. Nakagawa and S. Sakata, Progr. Theor. Phys. 28 (1962) 870.

[6] Particle Data Group, D.E. Groom et al., Eur. Phys. J. C15 (2000) 1.

[7] R.N. Mohapatra and G. Senjanović, Phys. Rev. Lett. 44 (1980) 912.

[8] L. Landau, Nucl. Phys. 3 (1957) 127; T.D. Lee and C.N. Yang, Phys. Rev. 105 (1957) 1671; A. Salam, Il Nuovo Cimento 5 (1957) 299.

[9] M. Goldhaber, L. Grodzins and A.W. Sunyar, Phys. Rev. 109 (1958) 1015.

[10] L. Wolfenstein, Phys. Rev. D17 (1978) 2369; Phys. Rev. D20 (1979) 2634.

[11] S.P. Mikheyev and A.Y. Smirnov, Sov. J Nucl. Phys. 42 (1985) 913.

[12] A. De Santo, hep-ex/0106089.

[13] J.N. Bachall et al., astro-ph/0010346; *http://www.sns.ias.edu jnb.*

[14] S.M. Bilenky et al., Prog. Part. Nucl. Phys. 43 (1999) 1.

[15] K. Nakamura et al., K2K Coll., Nucl. Phys. B Proc. Suppl. 91 (2001) 203.

[16] B.T. Cleveland et al., Astrophys. J 496 (1998) 505; K. Lande et al., Nucl. Phys. B Proc. Supp. 91 (2001) 50.

[17] J.N. Abdurashitov et al., Phys. Rev. C60 055801 (1999); V. Gavrin et al., Nucl. Phys. B Proc. Supp. 91 (2001) 36.

[18] W. Hampel et al., Phys. Lett. B447 (1999) 127.

[19] M. Altmann et al., Phys. Lett. B490 (2000) 16; E. Bellotti et al., Nucl. Phys. B Proc. Supp. 91 (2001) 44.

[20] K.S. Hirata et al., Phys. Rev. Lett. 77 (1996) 1683.

[21] Y. Fukuda et al., Phys. Rev. Lett. 81 (1998) 1158; Y. Fukuda et al., Phys. Rev. Lett. 86 (2001) 5651.

[22] The SNO Coll., Phys. Rev. Lett. 87 071301 (2001); A.B. McDonald, Nucl. Phys. B Proc. Suppl. 91 (2001) 21.

[23] S.M. Bilenky, hep-ph/0110306.

[24] J. N. Bahcall, M.C. Gonzalez-Carcia and C. Pena-Garay, hep-ph/0106258.

[25] G.L. Fogli, E. Lisi, D. Montanino and A. Palazzo, hep-ph/0106247.

[26] M. Aglietta et al., Europhys. Lett. 8 (1989) 611;

[27] C. Barger it et al., Phys. Lett. B227 (1989) 489; C. Barger et al., Phys. Lett. B245 (1990) 305; K. Daum et al., Frejus Coll., Z. Phys. C66 (1995) 417.

[28] W.W.M. Allison et al., Soudan 2 Coll., Phys. Lett. B391 (1997) 491; Phys. Lett. B449 (1999) 137; W. Anthony Mann, hep-ex/0007031 (2000); T. Mann et al., Nucl. Phys. B Proc. Suppl. 91 (2001) 134.

[29] R. Becker-Szendy et al., Phys. Rev. D46 (1992) 3270; D. Caspar et al., Phys. Rev. Lett. 66 (1991) 2561; R. Becker-Szendy et al., Nucl. Phys. B Proc. Suppl. 38 (1995) 331.

[30] K.S. Hirata et al., Phys. Lett. B205 (1988) 416; K.S. Hirata et al., Phys. Lett. B280 (1992) 146; Y. Fukuda et al., Phys. Lett. B335 (1994) 237-245.

[31] SuperKamiokande Coll., Y.Fukuda et al., Phys. Rev. Lett. 81 (1998) 1562; Phys. Lett. B433 (1998) 9; Phys. Rev. Lett. 85 (2000) 3999; Nucl. Phys. B Proc. Suppl. 91 (2001) 127; T. Toshito, hep-ex/0105023 (2001).

[32] S. Mikheyev for the Baksan Coll., 5^{th} TAUP Workshop Proc., Gran Sasso, Italy, 1997.

[33] S. Ahlen et al., MACRO Coll., Phys. Lett. B357 (1995) 481; M. Ambrosio et al., MACRO Coll., Phys. Lett. B434 (1998) 451; Phys. Lett. B478 (2000) 5; Phys. Lett. B517 (2001) 59. G. Giacomelli and M. Giorgini, *Atmospheric neutrino oscillations in MACRO*, hep-ex/0110021, Proc. of the NO-VE, Int. Workshop on Neutrino Oscillations in Venice, Venice, Italy, 2001.

[34] R. Engel, T.K. Gaisser, T. Stanev, Phys. Lett. B472 (2000) 113.

[35] V. Agrawal et al., Phys. Rev. D53 (1996) 1314; P. Lipari, T.K. Gaisser and T. Stanev, Phys. Rev. D58 073003 (1998).

[36] G.J. Feldman and R.D. Cousins, Phys. Rev. D57 (1998) 3873.

[37] M. Gluck et al., Z. Phys. C67 (1995) 433.

[38] W. Lohmann et al., *Energy loss of muons in the energy range 1-GeV to 10000-GeV.*, CERN-EP/85-03 (1985).

[39] P. Lipari et al., Phys. Rev. Lett. 74 (1995) 4384.

[40] M. Apollonio et al., Phys. Lett. B466 (1999) 415.

[41] F. Boehm et al., Nucl. Phys. B Proc. Suppl. 77 (1999) 166.

[42] C. Athanassopoulus et al., Phys. Rev. Lett. 77 (1996) 3082; Phys. Rev. Lett. 81 (1998) 1774; A. Aguilar et al., hep-ex/0104049 (2001).

[43] M. Honda et al., Phys. Lett. B248 (1990) 193; M. Honda et al., Phys. Rev. D52 (1995) 4985.

[44] G. Battistoni et al., Astrop. Phys. 12 (2000) 315; hep-ph/9907408.

[45] M.S. Longair, *High Energy Astrophysics*, Cambridge University Press, 1981, Reprinted 1997, Vol. 1, pp.300-324.

[46] W.R. Webber and J.A. Lezniak, Astrohys. Space Sci. 30 (1974) 361.

[47] AMS Coll., Phys. Lett. B472 (2000) 215.

[48] W. Frati et al., Phys. Rev. D48 (1993) 1140.

[49] T.K. Gaisser and T. Stanev, Bartol Preprint.

[50] M. Boezio et al., Caprice Coll., Ap. J. 518 (1999) 457.

[51] T. Sanuki et al., BESS Coll., astro-ph/0002481.

[52] W. Menn et al., *Measurement of the absolute proton and helium flux at the top of the atmosphere using IMAX*, Proc. of the 25^{th} ICRC, Vol. 3 (1997) 409.

[53] J.A. Simpson, Ann. Revs. Nucl. & Particle Science, 33 (1983) 323.

[54] S. Swordy et al., *Ring Imaging Cerenkov Counters: flight performance and future applications*, Proc. of the 23^{rd} ICRC, Calgary, Canada, Vol. 2 (1993) 500.

[55] K. Asakimori et al., *Cosmic ray composition and spectra: protons*, Proc. of the 23^{rd} ICRC, Calgary, Canada, Vol. 2 (1993) 21; *Cosmic ray composition and spectra: helium and $Z > 2$*, Proc. of the 23^{rd} ICRC, Calgary, Canada, Vol. 2 (1993) 25.

[56] P. Lipari, Astrop. Phys. 14 (2000) 171; hep-ph/0003013.

[57] P. Lipari, Astrop. Phys. 14 (2000) 153; hep-ph/0002282.

[58] M. Honda et al., hep-ph/0103328.

[59] T. Eichten et al., Nucl. Phys. B44 (1972) 333.

[60] M. Antinucci et al., Lettere al Nuovo Cimento 6 (1973) 121.

[61] P. Lipari, *The prediction of the atmospheric neutrino fluxes*, Cosmic Radiations: From Astronomy to Particle Physics, NATO Sciences Series, Vol. 42, p. 107.

[62] E. Lisi, A. Marrone and D. Montanino, Phys. Rev. Lett. 85 (2000) 1166.

[63] V. Barger et al., Phys. Lett. B462 (1999) 109.

[64] M. Ambrosio et al., MACRO Coll., hep-ex/0009002 (2000).

[65] G. t'Hooft, Nucl. Phys. B79 (1974) 276.

[66] M. Ambrosio et al., MACRO Coll., Eur. Phys. Jou. C13 (2000) 453.

[67] M. Ambrosio et al., MACRO Coll., Phys. Rev. D60 082002 (1999).

[68] M. Ambrosio et al., MACRO Coll., Phys. Rev. D62 (2000) 052003.

[69] M. Ambrosio et al., MACRO Coll., Phys. Lett. B434 (1998) 451.

[70] M. Ambrosio et al., MACRO Coll., Phys. Lett. B478 (2000) 5.

[71] S. Ahlen et al., MACRO Coll., Nucl. Instr. Meth. A324 (1993) 337; M. Ambrosio et al., *The MACRO detector at Gran Sasso*, accepted for publication on Nucl. Instr. Meth. A.

[72] S. Drell et al., Phys. Rev. Lett. 50 (1983) 644.

[73] M. Ambrosio et al., MACRO Coll., Phys. Rev. D60 032001 (1999).

[74] M. Ambrosio et al., Nucl. Instr. Meth. A321 (1992) 609.

[75] R. Fleischer, P.B. Price and R.M. Walker, Nuclear Tracks in Solids, University of California Press (1975).

[76] S. Cecchini et al., Nuovo Cim. A109 (1996) 1119.

[77] P.A.M. Dirac, Proc. of the Royal Society, London, A133 (1931) 60.

[78] M. Giorgini for the MACRO Coll., Nucl. Phys. B Proc. Suppl. 85 (2000) 227.

[79] I. D'Antone et al., IEEE, Trans. Nucl. Sci., 41 (1994) 83.

[80] G. Battistoni et al., *DREAM: the reconstruction program for the MACRO offline analysis*, MACRO Int. MEMO 1001/88.

[81] R. Brun, M. Goossens and J. Zoll, ZEBRA users guide, CERN Program Library Q100.

[82] R. Brun, D. Lienart, HBOOK user guide and Reference Manual, CERN Program Library Y250.

[83] R. Brun et al., FFREAD user guide and Reference Manual, CERN Program Library I302.

[84] F. Guarino et al., *GMACRO: MACRO detector through the GEANT 3 package*, MACRO Int. MEMO 16/87.

[85] F. Gasparini et al., Nucl. Instr. Meth. A267 (1988) 87.

[86] G. Battistoni et al., Accepted by Nucl. Instr. Meth. A, hep-physics/0105099.

[87] M. Giorgini for the MACRO Coll., *Performance of the MACRO limited streamer tubes for estimates of muon energy*, Proc. of the 7^{th} Int. Conf. on Advanced Technology and Particle Physics, Como, Italy (2001).

[88] R. Veenhof, Nucl. Instr. Meth. A419 (1998) 726.

[89] C. Peterson et al., Comput. Phys. Commun., 81 (1994) 185.

[90] M. Ambrosio et al., Astrop. Phys. 10 (1999) 11.

[91] M. Ambrosio et al., Astrop. Phys. 9 (1998) 105.